Spring 2022

A Mastcam Multispectral Investigation of Rock Variability in Gale Crater, Mars: Implications for Alteration in the Clay-Sulfate Transition of Mount Sharp

Alivia Eng
Western Washington University, aliviaeng@gmail.com

A Mastcam Multispectral Investigation of Rock Variability in Gale Crater, Mars: Implications for Alteration in the Clay-Sulfate Transition of Mount Sharp

By

Alivia M. Eng

Accepted in Partial Completion
of the Requirements for the Degree
Master of Science

ADVISORY COMMITTEE

Dr. Melissa Rice, Chair

Dr. Asmaa Boujibar

Dr. Kristina Walowski

GRADUATE SCHOOL

David L. Patrick, Dean

Master's Thesis

In presenting this thesis in partial fulfillment of the requirements for a master's degree at Western Washington University, I grant to Western Washington University the non-exclusive royalty-free right to archive, reproduce, distribute, and display the thesis in any and all forms, including electronic format, via any digital library mechanisms maintained by WWU.

I represent and warrant this is my original work, and does not infringe or violate any rights of others. I warrant that I have obtained written permissions from the owner of any third party copyrighted material included in these files.

I acknowledge that I retain ownership rights to the copyright of this work, including but not limited to the right to use all or part of this work in future works, such as articles or books.

Library users are granted permission for individual, research and non-commercial reproduction of this work for educational purposes only. Any further digital posting of this document requires specific permission from the author.

Any copying or publication of this thesis for commercial purposes, or for financial gain, is not allowed without my written permission.

Alivia M. Eng

May 12th, 2023

A Mastcam Multispectral Investigation of Rock Variability in Gale Crater, Mars: Implications for Alteration in the Clay-Sulfate Transition of Mount Sharp

A Thesis
Presented to
The Faculty of
Western Washington University

In Partial Fulfillment
Of the Requirements for the Degree
Master of Sciecne

By
Alivia M. Eng
May 2023

Abstract

The Mars Science Laboratory Curiosity rover has explored over 650 m of strata since landing in 2012. After leaving Vera Rubin Ridge (VRR), the rover traversed though the phyllosilicate-rich region, Glen Torridon, and the Mg-sulfate-bearing strata that lies above it, with excursions onto the Greenheugh Pediment and Amapari Marker Band. These unique stratigraphic units were investigated using Curiosity's instrument suite which includes the Mast Camera (Mastcam) pair of multispectral imagers. Mastcam's narrowband filters are sensitive to iron-bearing phases and some hydrated minerals. We used Mastcam spectra, in combination with chemical data from Curiosity's CheMin, APXS and ChemCam instruments, to assess the variability of rock spectra and interpret the mineralogy, depositional origin, and diagenesis in the clay-sulfate transition and surrounding regions. To constrain the Mg-sulfate detection capabilities of Mastcam and aid in the analyses of multispectral data, we conducted a laboratory investigation with different mixtures of phyllosilicates, hydrated Mg-sulfate, and basalt. We identify four new classes of rock spectra since leaving VRR. The localities and cross-instrument comparisons with these Mastcam spectra suggest that: (1) two of the new classes are inherent to dusty and pyroxene-rich surfaces on the Amapari Marker Band; (2) one new class is associated with the relatively young, basaltic, Greenheugh Pediment; and (3) one new class indicates areas subjected to intense aqueous alteration with an amorphous Fe-sulfate component, primarily in the clay-sulfate transition region. Our laboratory investigation shows the ease at which hydrated Mg-sulfates can be masked by other materials, requiring ≥ 90 wt. % of hydrated Mg-sulfate to exhibit a hydration signature in Mastcam spectra. Thus, we conclude that it would be challenging for Mastcam to detect Mg-sulfate in an intimate mixture. However, we can use these results to constrain the abundance of hydrated Mg-sulfates along Curiosity's future traverse. Together these results imply significant compositional changes along the traverse since leaving VRR, and they support the hypothesis of wet-dry cycles in the clay-sulfate transition. The new set of Mastcam spectral classes will provide a baseline for Curiosity's further exploration of Mount Sharp, where hydrated sulfates, minor phyllosilicates, and other hydrous mineral signatures have been identified from orbit.

Key words: Mars, Curiosity rover, spectroscopy, multispectral imaging

Acknowledgements

This research was made possible by support from the Western Washington University Geology Department and the MSL Participating Science Program. The data presented here were collected thanks to the MSL Science Team, the specialists at Malin Space Science Systems, and the calibration crew at Arizona State University. Special thanks to these parties for continuing to care for Curiosity, after over 10 years on Mars, and ultimately getting the rover to an incredible site to study for my Master's degree.

The work presented here was supported by many contributing co-authors: Melissa Rice, Elizabeth Rampe, Jeff Johnson, Lucy Thompson, Bill Farrand, and Samantha Jacob with supportive data provided by Rachel Sheppard, Janice Bishop, and Elizabeth Sklute. Particular thanks to Elizabeth Rampe, Lucy Thompson, and Jeff Johnson for providing data and guidance on CheMin, APXS, and ChemCam, respectively; Sections 5.4-5.6 would not have come to life without you. I thank Ed Cloutis for supporting my curation of samples and data acquisition. To Ben Paulson, Kristiana Lapo and Max Gabbert, thank you for all your support in my laboratory investigation- I truly could not have done it without the three of you. I would also like to acknowledge Acacia Arielle Evans and Lee Adair for their help in updating the multispectral database.

To friends that I have made at WWU and in the Western Mars Lab, thank you for always believing in and encouraging me when I doubted myself. Thank you to my committee, Kristina Walowski and Asmaa Boujibar, for providing non-Martian feedback that helped me connect my study to the big picture. I also want to acknowledge Allison Pfeiffer, Pete Stelling, Ben Paulson, and Paul Thomas, whose incredible characters and teaching styles drew me in to scientific research during my first year at WWU as an undergraduate. All my growth, as a human and scientist, during my time at WWU would not have been nearly as significant without the support of my loving family, partner, and furry companions. I'd like to dedicate this thesis to my grandparents who I lost the last 2 years; they quite literally believed I could do anything, and I know that they'll be watching out for me as I continue my academic journey away from home.

Lastly, I thank my advisor, Melissa Rice, who I'm not sure I'll ever be able to thank enough. From taking me in as a shy undergraduate to helping me grow into a more confident researcher, she has pushed me to places I thought I couldn't reach. The number of opportunities she provided me has built a sturdy foundation for the rest of my academic career. I will never forget the kindness and patience with which she treated me when I went through personal hardships, and I will always aspire to emulate her compassion and professionalism.

Table of Contents

List of Tables and Figures

I. Introduction

Mars hosts many geologic features that resemble those on Earth, making for an invaluable opportunity to contextualize our own planet's evolution. Both differentiated terrestrial planets formed from the same materials and have hosted flowing water. So why does Mars look so much different from Earth today? Key questions that scientists have been asking since the beginning of Mars exploration are "Was Mars able to host life during its 'warm and wet' era?" and "What caused the drying out of Mars?" These are questions that can only be answered by sending a rover equipped with a suite of scientific instruments to analyze the rock record in detail. Studying the geology of Mars informs processes that characterize environmental shifts and their effects on habitability, which has become increasingly important amid Earth's ongoing climate crisis.

1.1. Overview of Curiosity's Traverse and Instruments

In 2011, approximately 1.5 years before the launch of the Mars Science Laboratory (MSL) Curiosity rover, Gale crater was selected as its landing site from over 50 candidates (Golombek et al., 2012). Unique to Gale crater is a ~5 km sedimentary mound in the center known as Aoelis Mons (informally called Mount Sharp) (Figure 0). Given that the primary science objective of MSL is to assess past and present habitability, Gale crater was selected for two important reasons. First, Gale has a high potential for biologic preservation, since its phyllosilicate-rich units can maintain organics (e.g. organic Carbon (Broz, 2020)), if present. Additionally, the sulfate-rich units in lower Mount Sharp may harbor biosignatures (e.g. amino acids (Kotler, 2009)), S-isotopes and implications for biogeochemical S-cycling (Moreras-Mart et al., 2022). Second, the well-defined and exposed phyllosilicate- and sulfate- bearing beds in lower Mount Sharp are hypothesized to record a change in environmental conditions (Milliken et al., 2010) (Figure 1). However, it would take Curiosity 6.5 years (2300 sols) to reach the region responsible for its landing site selection.

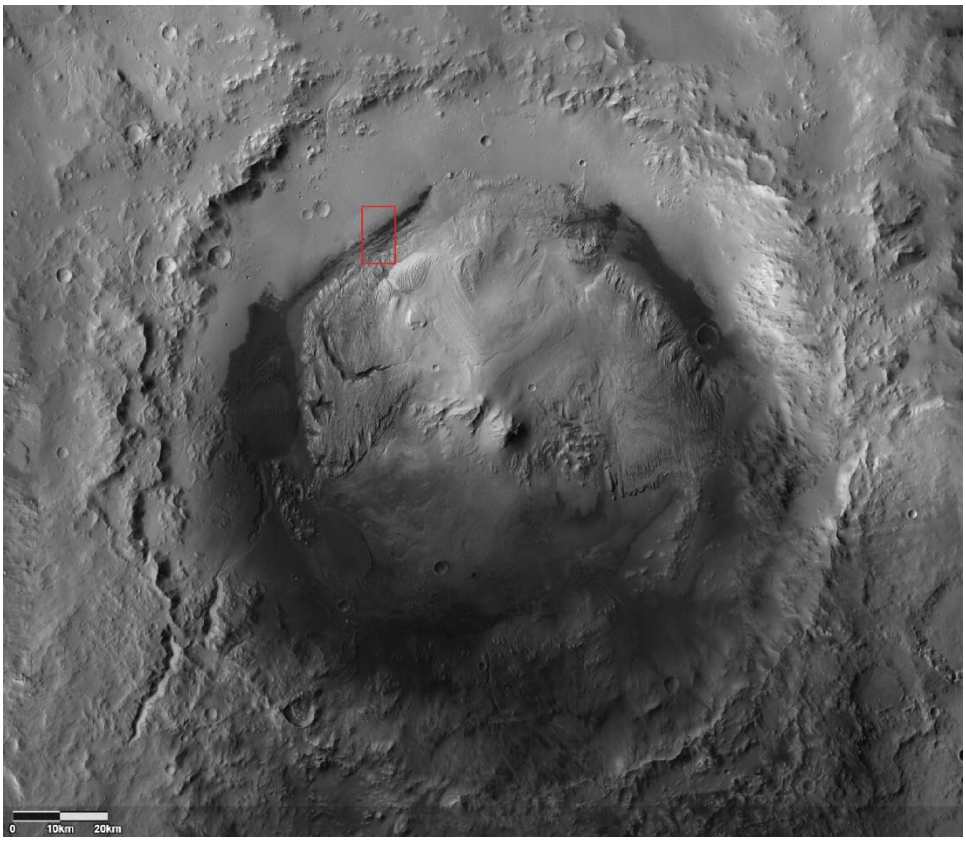

Figure 0: Grayscale map of Gale crater from the Context and the HiRISE cameras on NASA's Mars Reconnaissance Orbiter. Curiosity's traverse has covered the region outlined in red.

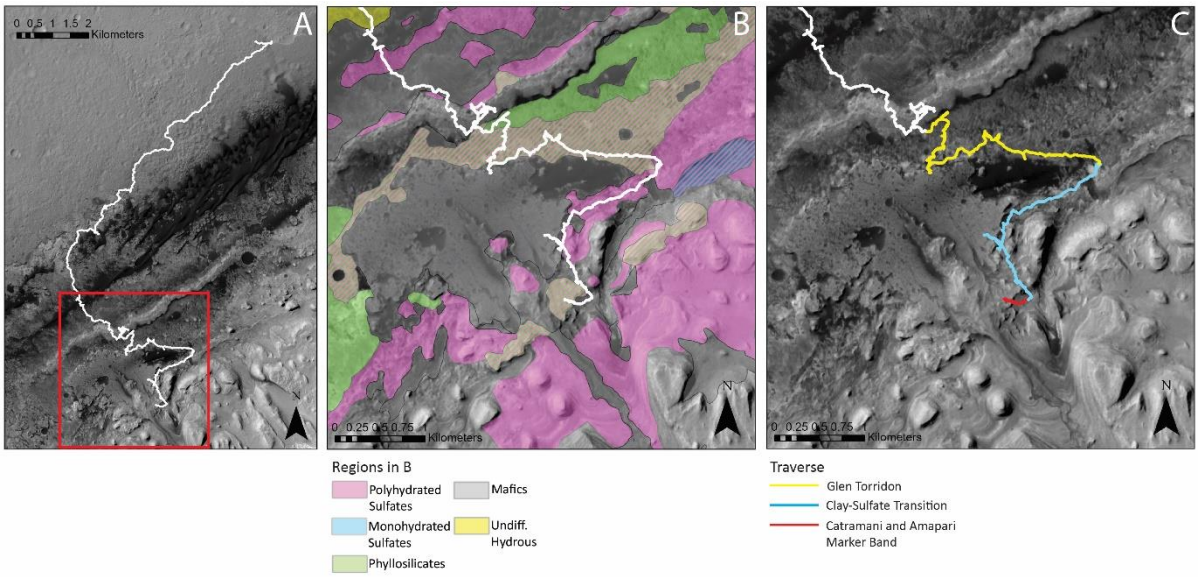

Figure 1: (A) Map of Curiosity's traverse over Mars Reconnaissance Orbiter Context Camera (CTX) mosaic of Gale crater through sol 3672 with more recent traverse in the red box and panels B and C. (B) Map of Curiosity's traverse from sol ~1570 to 3672 with mineralogic units from Sheppard et al. (2022). (C) Traverse in color represents regions of interest in this study and corresponds to colors in stratigraphic column in Figure 2.

Curiosity landed in a relatively flat, lower-elevation region north of Mount Sharp now known as the Bradbury group. The Bradbury group comprises the oldest and lowest-elevation rocks explored by Curiosity (Grotzinger et al., 2015) (Figure 2). Above the Bradbury group is the Murray formation of the Mount Sharp group. In-situ data from Curiosity of lower Mount Sharp is consistent with lacustrine deposits (Grotzinger et al., 2015), while the Upper Mount Sharp group is characterized by a hematite-rich ridge, known as Vera Rubin ridge (VRR). VRR was subjected to early oxidation followed by diagenetic fluids that produced a variety of grain sizes of hematite, and thus colors of the outcrop (Horgan et al., 2020). Curiosity then descended VRR into a trough-like region known as Glen Torridon (GT). After the GT campaign, Curiosity traversed through this study's region of interest, the clay-sulfate transition (CST), followed by multiple encounters with the Amapari marker band within Marker Band valley (MBV) (Figure 1). Also included in this study is data from the rover's two excursions onto Greenheugh pediment (GP). GP is a part of the Siccar Point group which lies unconformably over the Mount Sharp Group as a basaltic aeolian sandstone (Banham et al., 2022; Watkins et al., 2022).

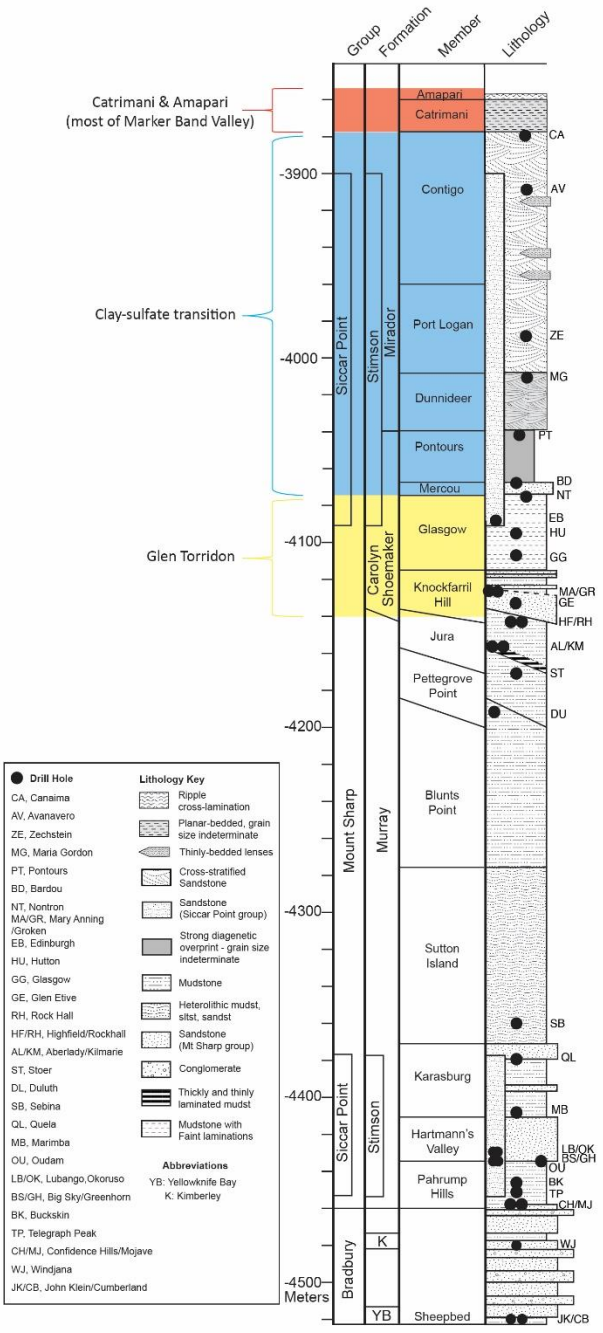

Figure 2: Stratigraphic column of Curiosity's traverse from landing (Yellowknife Bay) to the Amapari marker band. Colors correspond to regions of interest in this study and traverse in Figure 1C. Column provided by the MSL Sedimentology & Stratigraphy working group.

Since landing, Curiosity has investigated ~680 m of strata using the diverse suite of instruments. Included in the suite are the Mast Camera (Mastcam; Bell et al., 2012), Chemistry and Camera (ChemCam; Maurice et al., 2012; Wiens et al., 2012), Chemistry and Mineralogy (CheMin) powder X-ray diffraction and fluorescence instrument (Blake et al., 2012), and Alpha Particle X-ray Spectrometer (APXS; Campbell et al., 2012). Images acquired by the science cameras allow the MSL team to make stratigraphic and textural interpretations; and take quantitative measurements on grain size while spectroscopic data can inform the team of chemical and mineralogic compositions. By synthesizing orbital and in-situ data from Curiosity, the Sedimentology and Stratigraphy Working Group on the MSL team can define unique stratigraphic units encountered by the rover. After 10 years of exploration and nearly 30 km traveled, Curiosity's activities have become relatively conservative in order to preserve the lifetime of rover hardware. Of the rover's instrument suite, Mastcam and ChemCam, both located on the rover mast, are the least time and power intensive and can acquire the most observations at each stop. In contrast, CheMin requires a month's worth of activities, including drilling, and APXS requires arm movement and is often accompanied by the Dust Removal Tool (DRT) to brush dust off the surface. Thus, it is vital to characterize how different surface compositions can be identified in these Mastcam and ChemCam datasets in Curiosity's extended mission. In addition to characterizing targets in the rover's immediate workspace, Mastcam can collect multispectral data over broad spatial areas and expand upon stratigraphic units defined from orbit.

1.2. Motivation

Since leaving Vera Rubin ridge (VRR) (around sol 2302), Curiosity's traverse has since covered the most phyllosilicate-rich region yet observed, Glen Torridon (GT) (Bennet et al., 2023), overlain by sulfate-bearing strata (Figures 1 and 2). This transition, which was initially identified in orbital data, may indicate a change from a wetter environment that accommodated clay mineral formation to a drier environment that led to the precipitation of sulfates, specifically hydrated Mg-sulfates (Milliken et al., 2010). Mount Sharp is not the only location on Mars for which this transition has been observed, which has been hypothesized to signify a global environmental change around the Noachian-Hesperian transition (Bibring et al., 2006).

In GT, the fine-grained mudstones of the Murray formation and the cross-bedded sandstones and laminated mudstones of the Carolyn Shoemaker formation reflect a transition from a low-energy lacustrine depositional setting to fluvial deposits in a lake margin environment (see Section 2.1; Bennett et al., 2022) (Figure 2). However, the environmental conditions in which the clay-sulfate transition region formed remain elusive. The multiple working hypotheses include lacustrine and aeolian depositional settings (Rapin et al., 2019,2021; Roberts et al., 2023) and multiple diagenetic episodes (Seeger et al., 2023; Rapin et al., 2023). Along with visual analysis of the sedimentology and stratigraphy in rover images, spectroscopy techniques (e.g., APXS, ChemCam, VNIR) are used to gather chemical data to deduce the complex geologic history of Gale crater. However, diagnostic hydration features of Mg-sulfates in (VNIR) reflectance spectra are easily masked by the presence of phyllosilicates (Sheppard et al., 2022), further complicating analyses of their history on Mars. Recognizing these challenges, we present a detailed analysis of reflectance spectra from these materials, since understanding the spectral behavior of Mg-sulfates is vital to characterizing the environmental shift in Gale crater's Noachian-aged lake system.

In this study, we use (1) VNIR (447–1,013 nm) multispectral observations from the stereoscopic imaging system, Mast Camera (Mastcam), and (2) cross-instrument comparisons with visible (400–840 nm) point spectra from the ChemCam spectrometer, compositional data from the APXS, and X-ray diffraction data from the CheMin instrument to assess the variability of rock spectra in GT, the clay-sulfate transition region, Greenheugh pediment (GP) of the Stimson formation, part of Marker Band Valley (MBV), and the rover's first encounter with the Amapari marker band (Figure 1). To support mineralogic interpretations of Mastcam spectra of potentially sulfate-bearing targets, we conducted a laboratory investigation of mineral mixtures. Our mixtures consist of Mg-sulfate, phyllosilicates that have been detected by the rover, and crushed Mars-analog basalt to quantify how much Mg-sulfate would be required for Mastcam to detect it. We test two main hypotheses: (1) New spectral classes will appear in accordance with new stratigraphic members encountered by Curiosity (specifically, we expect the occurrence of absorptions near 1000 nm in Mastcam spectra due to hydration as Curiosity traverses through the clay-sulfate transition and the Marker Band valley); (2) Sheppard et al. (2022) found that a wt. % > 10 of montmorillonite can mask the 1.4 and 1.9 μm bands of Mg-sulfate in orbital data. Based on their results, the subtlety of the 1.0 μm band, and the light tone inherent to Mg-sulfates,

we hypothesize that it will take small fractions of phyllosilicates and basalt to completely mask the hydration feature around 1.0 μm in spectra convolved to Mastcam wavelengths. The results of this study constrain environmental conditions in which the clay-sulfate transition formed and alteration experienced post-deposition.

II. Background

2.1. Geologic Context

There are multiple hypotheses for the geologic history of Gale (e.g., Niles and Michalski, 2012; Kraft and Christensen, 2013; Kling et al., 2020) but the data from Curiosity are most consistent with lacustrine and aeolian processes filling and carving the crater interior following the impact (Rapin et al, 2021; Buz et al, 2017). The stratigraphic groups identified thus far are Bradbury, Siccar Point, and Mount Sharp (Bennet et al., 2023) (Figure 2). The origin of the fluvial/lacustrine sediment in the Bradbury Group and Murray formation from streams transporting it down the northern rim of the crater is consistent with orbital and rover observations (Vasavada, 2022). Additionally, Thomson et al. (2019) found that sediments above the elevation of the northern unbreeched rim cannot have been deposited by flowing water. Thus, a significant amount of the sediment in Gale was likely deposited by aeolian suspension. Wind-driven erosion then carved the filled crater into the landscape Curiosity is exploring today. Curiosity first explored the Bradbury Group, which consists of fluvio-deltaic deposits along the crater floor ranging from mudstones to conglomerates (Grotzinger et al., 2015). The lower strata of the Mount Sharp Group explored to date consist of laminated mudstones and sandstones in the Murray and Carolyn Shoemaker formations. Glen Torridon, which records a transition from a low-energy lacustrine environment to a higher-energy fluvial one, encompasses the Carolyn Shoemaker formation. Overlying the Carolyn Shoemaker formation is the Mirador formation. The Mirador formation is distinguished by cross-stratified pebbly sandstone, cross-stratified sandstone with thinly bedded lenses, and a planar-bedded member (Catrimani) with indeterminate grain size due to strong diagenetic overprints (Figure 2). The CST comprises the upper Carolyn Shoemaker formation up to roughly the Catrimani member in the Mirador formation. Strata in the CST are hypothesized to represent a transition from a fluvial and lake margin environment to aeolian with wet-dry cycles (Rapin et al., 2023; Das et al., 2023). In the

rover's recent exploration of the Mount Sharp Group, it entered 'Marker Band Valley,' which is surrounded by buttes and comprises the upper ~10 meters of the Contigo member, the Catrimani member, and the marker band itself. The dark-toned Amapari Marker Band displays rippled and rhythmic textures (Gupta et al., 2023; Weitz et al., 2023; Lewis et al., 2023) and a high-Ca pyroxene signature from orbit (Weitz et al., 2022). In-situ analyses by the rover show changes in morphology and chemistry between the sulfate-bearing layers below and above the marker bed and the marker band itself (Gasda et al., 2023; Berger et al., 2023; Thompson et al., 2023). Unconformably atop Mount Sharp lies the Siccar Point Group as a much younger basaltic aeolian sandstone (Banham et al., 2022; Watkins et al., 2022). A majority of Mastcam multispectral observations in this study are from the Mount Sharp Group with 12 exceptions from the Siccar Point Group during excursions onto the Greenheugh Pediment.

CheMin analyses from GT reveal phyllosilicates (up to 30 wt %) such as the dioctahedral smectite nontronite, Ca-sulfates (up to 25 wt%), hematite (4-8 wt.%), and X-ray amorphous materials (~30-55 wt.%) (Thorpe et al., 2022). The clay-sulfate transition region reveal dioctahedral smectite, with greater abundance at the base of the transition (up to 18 wt%), hematite (up to 8.4%), goethite (up to 4.1%), Ca-sulfates (up to 20.6 wt%), starkeyite in one drill target (2.3 wt%, the first detection of crystalline Mg-sulfate in the Mirador formation), and X-ray amorphous materials (wt. %) (Rampe et al., 2023). The X-ray amorphous material is primarily made up of the major oxides SiO_2, FeO_T, MgO, CaO and SO_3, which suggests much of the amorphous component formed via secondary processes (i.e., from water-rock interactions) (Simpson, 2023). CheMin and SAM analyses of the Canaima drill powder from the top of the CST indicate the presence of amorphous Mg sulfate (e.g., Rampe et al., 2023). These strata and the regional geomorphology suggest that Gale had once been filled with a lake and accompanying sediments via fluvial and aeolian deposition which was then eroded into the modern landscape via fluvial and aeolian processes (Thomson et al., 2019).

The interpretations of clay-sulfate transitions in ancient lacustrine systems on Mars rely primarily on data and analyses of terrestrial analog environments (e.g., Lynch et al., 2015). Clay-bearing strata are characteristic of the following types of deposition on Earth: lacustrine deposits via in situ formation under alkaline or saline conditions if Mg- or Fe- smectites, such as saponite, are major components (Bristow et al., 2009); or continental deposits in soils and weathering

profiles caused by alteration of volcanic material if Al- or Fe- phyllosilicates are detected, such as montmorillonite or nontronite (Bristow and Milliken, 2011; Lynch et al., 2015). The detection of Mg-smectites by the Compact Reconnaissance Imaging Spectrometer for Mars (CRISM) instrument on the Mars Reconnaissance Orbiter (MRO) spacecraft (Murchie et al., 2006), however, does not necessarily confirm a lacustrine deposit. Mg/Fe-smectites, such as saponite and nontronite, may indicate weathering profiles of mafic rocks or hydrothermal alteration due to impacts during early Mars (Bristow & Milliken, 2011). Additionally, these detections are complicated by the fact that these materials have been subjected to erosion and transport over potentially billions of years (Day et al., 2016). Based on closed basin environments studied on Earth (e.g., Currey, 1990; Douglas, 2004), a shift to a drier climate will reduce the water input to the lake thus increasing the concentration of ions and allowing sulfates to form. The abundance of diagenetic features (e.g., nodules, veins, concretions) in Gale crater, however, suggests the possibility of sulfates as a post-depositional diagenetic phase via water-rock interactions (Bennett et al., 2023; Gasda et al., 2022; Rapin et al., 2023; Seeger et al., 2023).

2.2. Mastcam

Mastcam collects VNIR (447–1,013 nm) multispectral observations, providing context for other instruments and broad mineralogic interpretations. Importantly, Mastcam can collect multispectral data over broad spatial areas and expand upon stratigraphic units defined from orbit. The filter positions used by Mastcam makes it sensitive to iron oxides, due to electronic transitions and charge transfers from crystal field theory (Burns, 1993) and some hydrated minerals, due to stretching and bending vibrations (Bishop, 2019). Both iron oxides and hydrated minerals are important indicators of alteration (Rice et al., 2013) and thus aids in the reconstruction of Mars' geologic history (e.g. Horgan et al., 2020). In previous work, a database of Mastcam spectra was compiled for Curiosity's traverse from landing through the exploration of Vera Rubin ridge (sols 0-2302), from which 9 spectral rock classes were identified (Rice et al., 2022a) (Figure 3). Each class has diagnostic spectral features that reflect a mineralogic interpretation and are confined to stratigraphic formations or specific to a geologic feature (e.g., meteorites). In this study we have modified the names of these classes to be more descriptive of either interpreted mineralogy or spectral shape (Figure 3).

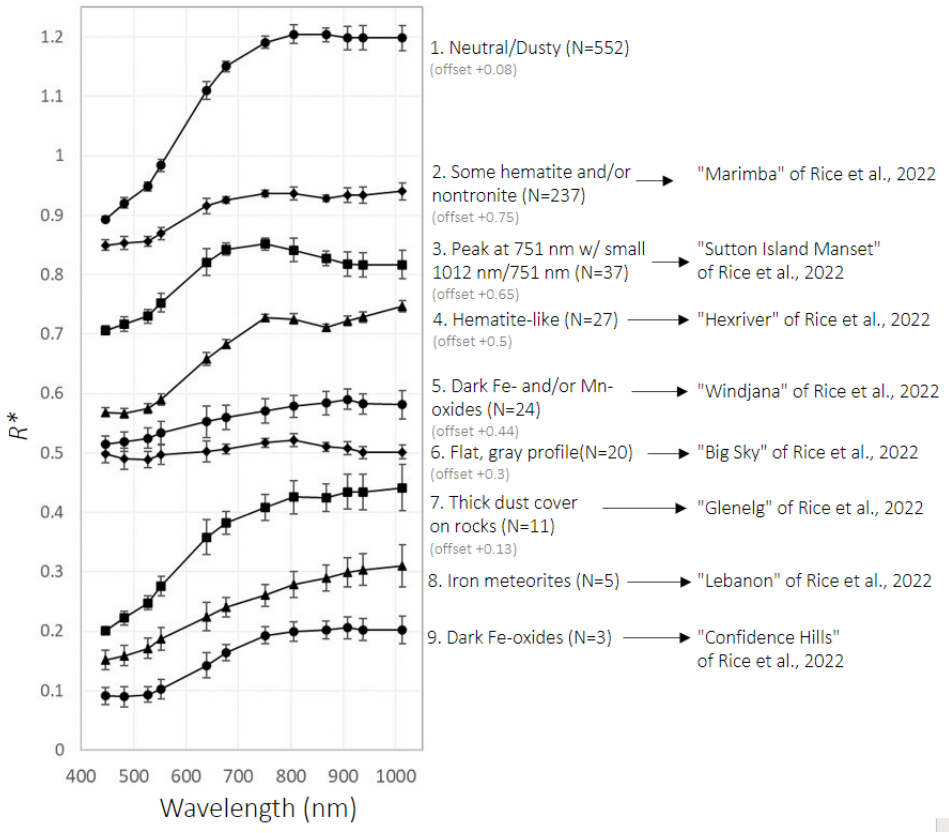

Figure 3: Mastcam rock spectral classes defined by Rice et al. (2022a) using observations from landing through Vera Rubin ridge (VRR). Note that the class names have been revised to be more descriptive of either mineralogic interpretation or spectral shape. N represents the number of spectra categorized as this class through VRR. Error bars are the relative standard deviation of each individual spectrum.

Rudolph et al. (2022) synthesized Mastcam multispectral observations across GT and found two abundant and widespread spectral types. The first were spectra with strong red slopes and absorption bands centered around 900-950 nm, indicative of Fe-bearing clay minerals in the context of GT materials. The second were spectra with strong red slopes and absorption bands centered at 867 nm, indicative of fine-grained, crystalline red hematite. As Curiosity continued up Mount Sharp, phyllosilicates disappeared (Rampe et al., 2023) and sulfates became more abundant. Pure epsomite and other polyhydrated Mg-sulfates convolved to Mastcam wavelengths exhibit a 'downturn' in the last two wavelength filters as a result of the filter positions and ~950-1000 nm hydration feature (Figure 4), hereinafter referred to as the R6 downturn. The R6 downturn is characterized by a 1013 nm/937 nm ratio (R6/R5) < 1.0 but is

only diagnostic of hydration if the NIR spectum is otherwise flat. The R6 downturn has yet to be observed in clay-sulfate transition drill targets. Rather, Mastcam spectra of the tailings (from sols 3055-3612) are characterized by hematite and phyllosilicate abundances (Jacob, 2023).

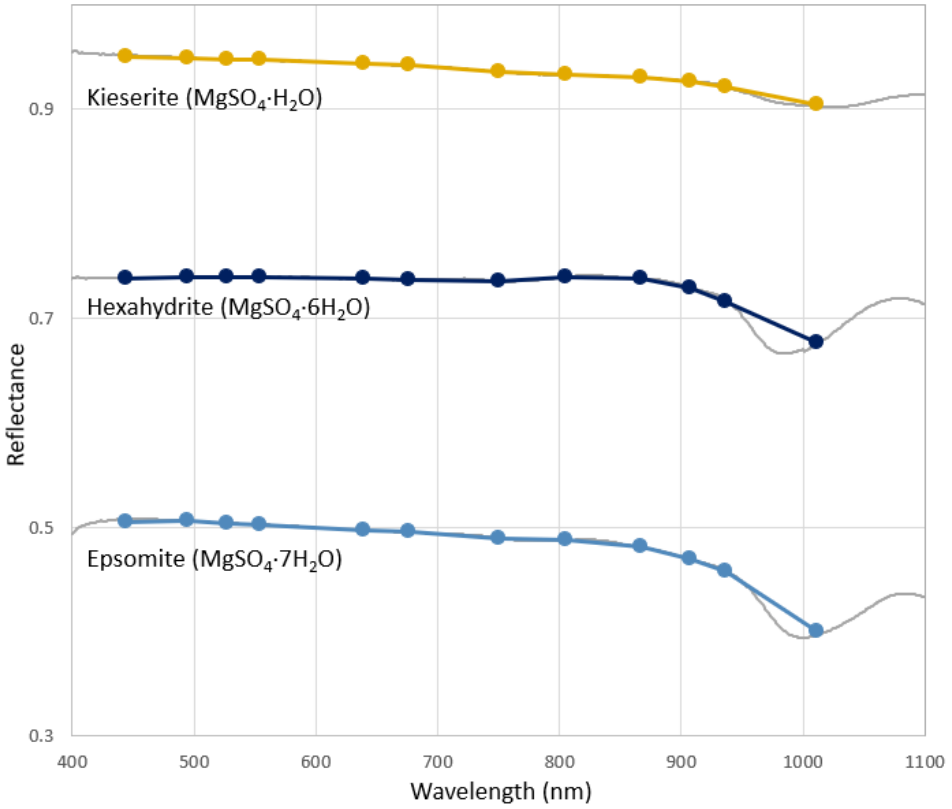

Figure 4: Spectra of synthetic polyhydrated and monohydrated Mg-sulfates convolved to Mastcam wavelengths from Dixon (2018) in color; high resolution spectra in gray. The grain size of these samples is 500-1000 um. The small hydration feature around 1000 nm manifests as an R6 downturn in the last two wavelength filters in convolved spectra (I.e., 1013 nm/937 nm < 1.0) Band depths decrease with less structurally bound water molecules and smaller grain sizes (Dixon, 2018).

2.3. Laboratory investigations of Mastcam's epsomite detection threshhold

Multiple studies have proven the ease at which Mg-sulfates dehydrate and rehydrate when exposed to Mars-like pressures and to different relative humidities (RHs) and temperatures (Vaniman et al., 2004; Cloutis et al., 2007). Thus, the identification of Mg-sulfates holds value as an environmental proxy. Vaniman et al. (2004) found that at low pressure and RH, epsomite

($MgSO_4 \cdot 7H_2O$) partially dehydrates and converts to hexahydrite ($MgSO_4 \cdot 6H_2O$). The hexahydrite then becomes amorphous, the rate of desiccation decreases dramatically, and the sample resists complete dehydration. In contrast, the monohydrated phase, kieserite ($MgSO_4 \cdot H_2O$), remains crystalline. When exposed to elevated RH conditions, kieserite easily hydrates and converts to hexahydrite then epsomite. The amorphous material made from hexahydrite recrystallizes to form hexahydrite, pentahydrite ($MgSO_4 \cdot 5H_2O$), and starkeyite ($MgSO_4 \cdot 4H_2O$). Given the results of Vaniman et al. (2004), it is unlikely that Mg-sulfates with high degrees of hydration are stable on Mars; rather, we expect to find Mg-sulfates with intermediate degrees of hydration that are the products of dehydration (Wang et al., 2009; Wang et al., 2016).

Dixon (2018) performed experiments to constrain the amounts of hydrated sulfates that could be detectable using Mastcam bandpasses. They found that mixtures of different Mg-sulfates exhibit more negative slopes at longer wavelengths depending on epsomite abundance, whereas dust-contaminated samples reduced spectral slopes. Examples of species detectable by Mastcam included pure epsomite (at all grain sizes from <63 μm to 4000 um), and bi-modal mixtures of different Mg-sulfates (epsomite, hexahydrite, and kieserite) with grain sizes of 500-1000 um. However, just 5 wt. % of palagonitic dust simulant (JSC-Mars1 at a grain size of <500 um) made epsomite-kieserite mixtures (with ≤60 wt. % epsomite) undetectable by Mastcam. Cloutis et al. (2007) found that as time exposed to Mars-like conditions increases, the 1.45 and 1.95 μm absorptions in reflectance spectra of polyhydrated Mg-sulfates shallow and the shoulders flatten.

Artificial mixtures of phyllosilicates and sulfates have been used in spectroscopic analysis but were limited to wavelengths outside of Mastcam's spectral range (Sheppard et al., 2022; Stack & Milliken, 2015). In addition, there are scarce studies in which natural materials were included in experimental mineral mixtures (e.g., Roush et al., 2015), which undoubtedly provide valuable information on the spectral behavior of rock and soil targets on Mars. Modeling spectra of mixtures in the NIR has been proven difficult due to the effects of grain size, viewing geometry, and the non-linear mixing behavior (Hapke et al., 1993; Shkuratov et al., 1999; Harris & Grindrod, 2018), thus warranting lab experiments of multiple mixtures. Most relevant to our lab study are the findings of Sheppard et al. (2022), who found that montmorillonite can

spectrally mask the presence of Mg-sulfates if the former is above ~10 wt%. Their analysis, however, was focused on the changes to hydration features outside of Mastcam's wavelength range with applications to CRISM data. Jacob (2022) found in their study of mineral mixtures that the diagnostic R6 downturn of epsomite in Mastcam spectra is easily overwhelmed by plagioclase and pyroxene, even at 50 wt% epsomite. In this study we quantify the threshold at which the hydration feature around 950-1000 nm is present in convolved lab spectra of bi-modal mixtures of phyllosilicates and epsomite. We also add small fractions of powdered basalt to assess the overall dampening of spectral features.

III. Methods

3.1. Image analysis and spectra classification

Mastcam is a multispectral, stereoscopic imaging instrument with a left (M34) and right (M100) camera. These cameras can acquire visible to near infrared (VNIR) reflectance spectra in 12 unique wavelengths from 445-1012 nm by collecting multiple images through different filters on a spinning wheel. Once through the filter wheel, light travels through a Bayer pattern of broadband RGB filters bonded to a charge coupled device which is used in many digital imaging systems (Bell et al., 2017; Malin et al., 2017). VNIR reflectance spectra are not only sensitive to composition but also to grain size and viewing/illumination geometry. To better understand these effects, Mastcam observations are sometimes acquired multiple times a day under variable solar incidence angles. These types of photometry experiments, and grain size experiments, are also conducted in laboratories on Earth and can enhance our interpretations of Mastcam multispectral data. In this study, however, Mastcam multispectral observations were restricted to within 1.5 hours of local noon (to limit the calibration uncertainties that arise at high incidence angles and avoid photometric effects). A total of 908 observations acquired with both Mastcam cameras were used, with 284 collected after sol 2300 in GT, GP, the clay-sulfate transition, MBV and the Amapari marker band (Supplemental Table 1).

For spectral analyses, we followed the methodology described by Rice et al. (2022a) and utilize the previously compiled database of observations prior to sol 2302 (Rice, 2022). Raw sensor values were radiometrically calibrated, using a reduction pipeline that included near-

simultaneous observations of a calibration target (Bell et al., 2017). Radiometrically-calibrated I/F values were converted to reflectance factor (R*) by dividing by the cosine of the solar incidence angle. To highlight the color and spectral variability, we applied a decorrelation stretch to all calibrated Mastcam images which we used to identify regions of interest (ROIs) representative of the morphologic and color diversity within each scene. Spectra were extracted by averaging the R* values of pixels within each ROI and compiled in a database with extensive metadata (including feature type, viewing geometry, sol, local true solar time (LTST), tau, elevation, L_S, etc.). We followed the "best practices" for identifying and selecting ROIs as described by Rice et al. (2022a).

Principal component analysis (PCA) was utilized to understand what spectral features were contributing most to the variability of rock spectra in the dataset (sols 2303-3672). We first normalized spectra to 1.0 at their peak reflectance to avoid components related to albedo, especially since non-mineralogic factors can affect overall reflectance (e.g. shadows) (Rice et al., 2022a). The average relative standard deviation was restricted to 0-0.2. Eight observations were omitted due to either calibration errors or targets at a distance that could not be correlated with rover elevation. To perform the analysis, we used the Scikit-learn Python package (Pedregosa et al., 2011) and then plotted the resulting PCs against each other to identify spectra that represent the minimum and maximum values of each component.

In order to interpret mineralogic trends across the full dataset, we utilized spectro-stratigraphic and parameter plots. The spectro-stratigraphic columns allow for analysis of spectral variations across the traverse as a function of elevation. We selected spectral parameters based on the major spectral contributors to rock spectra, as defined by the PCA. From the clustering of rock spectra within these parameter spaces we identified spectral classes (some the same as – and others distinct from –) the classes of Rice et al. (2022a)). We used visual inspection of the parameter plots and the spectra themselves to distinguish unique classes, comparing the Mastcam spectra to spectra of pure minerals from laboratory databases (Figure 5). The spectral parameters that most greatly aided in the analysis and interpretation of Mastcam spectra are summarized in Table 1.

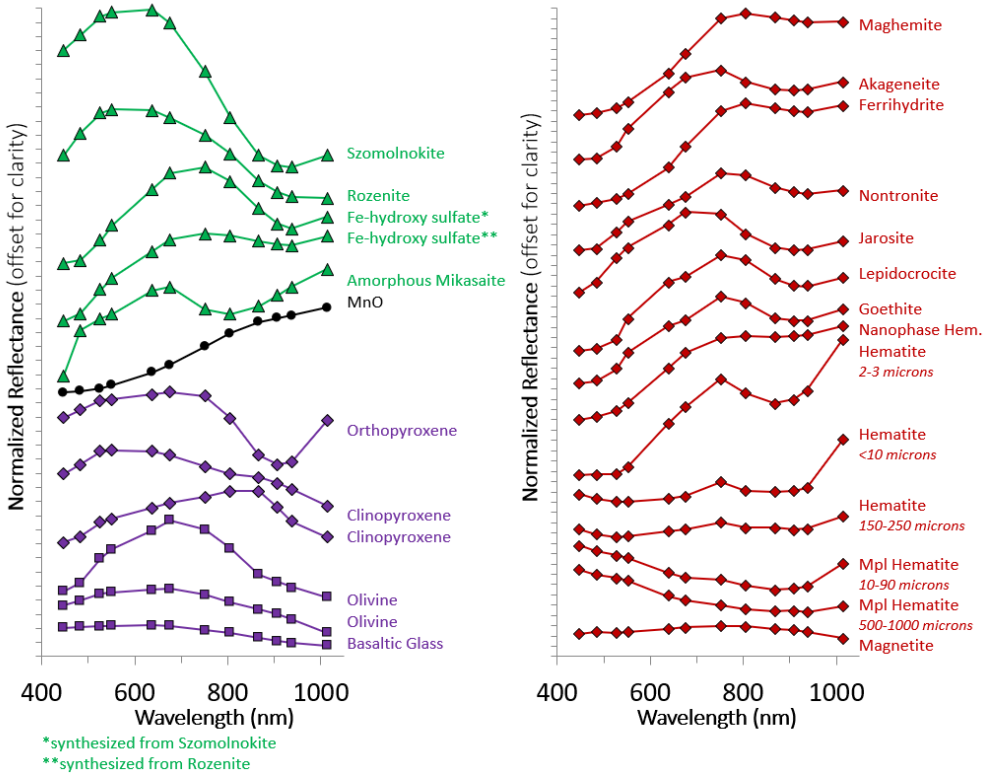

Figure 5: Laboratory spectra of Fe-bearing minerals and oxides, modified from Figure 5 of Rice et al. (2022a): ferrous sulfates (light green triangles); MnO (black circles); pyroxenes (purple diamonds; olivines and basaltic glass (purple squares); ferric alteration phases (red diamonds). Ferrous sulfates are from Bishop et al. (2021). The amorphous mikasaite was synthesized by Elizabeth Sklute using the methods described in Sklute et al. (2015). Microplaty (Mpl) hematite spectra are from Lane et al. (2002). Spectra have been convolved to Mastcam spectral bandpasses, normalized to 1.0 at 751 nm, and offset for clarity.

Table 1: Summary of Spectral Parameters Used to Characterize Mastcam Spectra. Modified from Rice et al. (2022a).

Camera	Parameter	Formula	Possible mineralogic indicators
Left	L6 (1012 nm)/L3 (751 nm) ratio	R^*_{1012}/R^*_{751}	Used as a proxy for NIR profile; values <1.0 are consistent olivine, clinopyroxene, and basaltic glasses; values >1.05 can be indicative of iron meteorites
Left	L5 (867 nm)/L4 (676 nm) ratio	R^*_{867}/R^*_{676}	Values <1.0 may indicate ferric sulfates or olivine.
Left	L1 (527 nm) band depth	$1—R^*_{527}/(0.645R^*_{445} + 0.355R^*_{676})$	Larger value can indicate higher degree of Fe oxidation (e.g., Farrand et al., 2008)
Left	L3 (751 nm)/L2 (445 nm) ratio	R^*_{751}/R^*_{445}	Termed "red/blue ratio" and can indicate "redness" of spectra; larger values are consistent with higher degrees of oxidation
Left	L3 (751 nm)/L1 (527 nm) ratio	R^*_{751}/R^*_{527}	A modified version of the "red/blue ratio"; values >1.1 are consistent with iron meteorites (e.g. Wellington et al., 2018)
Left	L5 (867 nm) band depth	$1-R^*_{867}/(0.556R^*_{751} + 0.444R^*_{1012})$	Largest values are consistent with presence of fine-grained, red crystalline hematite, and smaller positive values consistent with other Fe-oxides. Negative values indicate a convex NIR profile more consistent with olivine, pyroxenes and nontronite (e.g. Horgan et al., 2020)
Right	1013 nm/937 nm	R^*_{937}/R^*_{1013}	Used to quantify the spectral "downturn" or "uptick" in the longest Mastcam wavelength. Values >1.0 with otherwise flat NIR profiles are consistent with a hydration band at ~980 nm (Rice et al., 2010). Large values paired with large 805/937 nm ratios are consistent with broader 900–1000 nm absorptions (e.g., olivines, pyroxenes). Values <1.0 are more consistent with 800–900 nm absorptions (e.g., hematite).

3.2. Cross-instrument analyses

Using these new Mastcam spectral classes of rocks, we classified Mastcam spectra of all CheMin target drill tailings to decipher what crystalline minerals are contributing to the shape of Mastcam spectra. The CheMin instrument is an X-ray diffractometer (XRD) and X-ray fluorescence (XRF) spectrometer that operates in transmission geometry (Blake et al., 2012). CheMin analyzes a few 10s of milligrams of drill powder or scooped loose sediment, typically over three nights for a total of ~22 hours of analysis. CheMin uses a Co X-ray source to substantially reduce fluorescence from Fe-bearing phases. XRD patterns are collected from 4 to 52°2θ (Co-Ka) with an angular resolution of ~0.3°2θ. Patterns are analyzed via Rietveld refinement (e.g., Rietveld, 1969) and the full-pattern fitting software FULLPAT (e.g., Chipera and Bish, 2002) to quantify mineral abundances to a detection limit of ~1 wt.%, determine unit-cell parameters of minerals present in abundances >5 wt.% of the bulk, and quantify X-ray amorphous abundance.

We also classified all surfaces subjected to the dust-removal tool (DRT), which mitigates the effects of dust and is utilized whenever possible prior to obtaining APXS rock analyses. In doing so we can compare the Mastcam multispectral classifications of the dust-removed surfaces to elemental abundances. APXS measures the chemistry of rocks, unconsolidated material and the atmosphere on Mars using a combination of particle induced X-ray emission and X-ray fluorescence spectroscopy (see Campbell et al., 2012, 2014, Gellert et al., 2006, 2015 and Reider et al., 2003 for instrument details). APXS acquires elemental abundances for Na, Mg, Al, Si, P, S, Cl, K, Ca, Ti, Cr, Mn, Fe, Ni, Zn and Br, and all elements are normalized to 100% and reported as weight% oxides except for Cl, Ni, Zn and Br (Gellert et al., 2006, Campbell et al., 2012). Cl is reported as weight% element, and Ni, Zn and Br as parts per million (ppm). The highest quality APXS data is acquired during cooler temperatures (-25 to -45°C) and over integration times of 4 hours or more. Acceptable quality data can be acquired during as little as 20 minutes of integration time. The APXS instrument is deployed to contact, or within a 2 cm standoff from the surface to be measured, resulting in a field of view of 1.5 – 3 cm. Thus, compositional data is acquired from the area within the respective FOV, and from sample depths of 2-5 μm for the lighter elements 50 μm for the heavier elements (Reider et al., 2003).

In order to further validate the presence of new classes, we compared measurements between Mastcam and ChemCam reflectance spectra on similar surfaces. Relative reflectance data from Mastcam and ChemCam exhibit similar trends in the 400-840 nm region with stratigraphy (e.g. Fraeman et al., 2020; Seeger, 2020; Horgan 2020). As shown by Johnson et al. (2015) ChemCam measurements acquired without the laser on sunlit surfaces have been used as a means of acquiring passive radiance spectra (called "passive spectra") with absolute calibration uncertainty of ~6-8%. Relative reflectance spectra in the 400-840 nm region were estimated by dividing a scene radiance spectrum by a white calibration target radiance spectrum, followed by multiplication by the known laboratory reflectance of the calibration target material (e.g., Johnson et al., 2015).

3.3. Laboratory investigation of Mastcam's epsomite detection threshhold

To study the spectra of phyllosilicate-sulfate mixtures, as a comparison to alteration mineral assemblages that Mastcam may encounter, we used a similar suite of minerals to that of Stack & Milliken (2022), which was based on identifications made previously in CRISM and Observatoire pour la Minéralogie, l'Eau, les Glaces et l'Activité (OMEGA) spectra of Mars. This included the polyhydrated Mg-sulfate, epsomite; smectites, montmorillonite, saponite, and nontronite; and a basalt collected from the Grande Ronde flow of the Columbia River Basalt Group in Eastern Washington State (Figure 6, Table 2). We use epsomite because the Mg-sulfate identified by CheMin, starkeyite, is spectrally similar in the VNIR range but is not stable under typical laboratory conditions. The montmorillonite sample was sourced from the Clay Minerals Society (SWy-1). The saponite sample (SAP101) has been characterized by the University of Winnipeg Planetary Spectrophotometer Facility (UWPSF) with an estimated purity of 98% and minor feldspars. The nontronite sample (NON105 from UWPSF) was collected from the same road cut as the Source Clay Minerals Repository sample SWa-1 in Grant County, WA, USA and has been characterized in detail by Turenne et al. (2023). The Columbia River Basalts have been characterized in detail and proven to be suitable spectroscopic Mars-analogs (e.g., Michalski et al., 2006; Hoza, 2019; Lapo, 2021; Curtis, 2022). None of the trace mineral components in our samples have significant effects on the spectra. Epsomite, nontronite, and saponite were crushed using a mortar and pestle. The basalt was crushed using a mixer mill. All components were dry-sieved to a grain size range of 75 µm - 106 µm based on rock grain size measured in situ (e.g.

Rivera-Hernandez et al., 2020; Minitti et al., 2021). A high precision scale was used to measure the weight of each component in the mixtures.

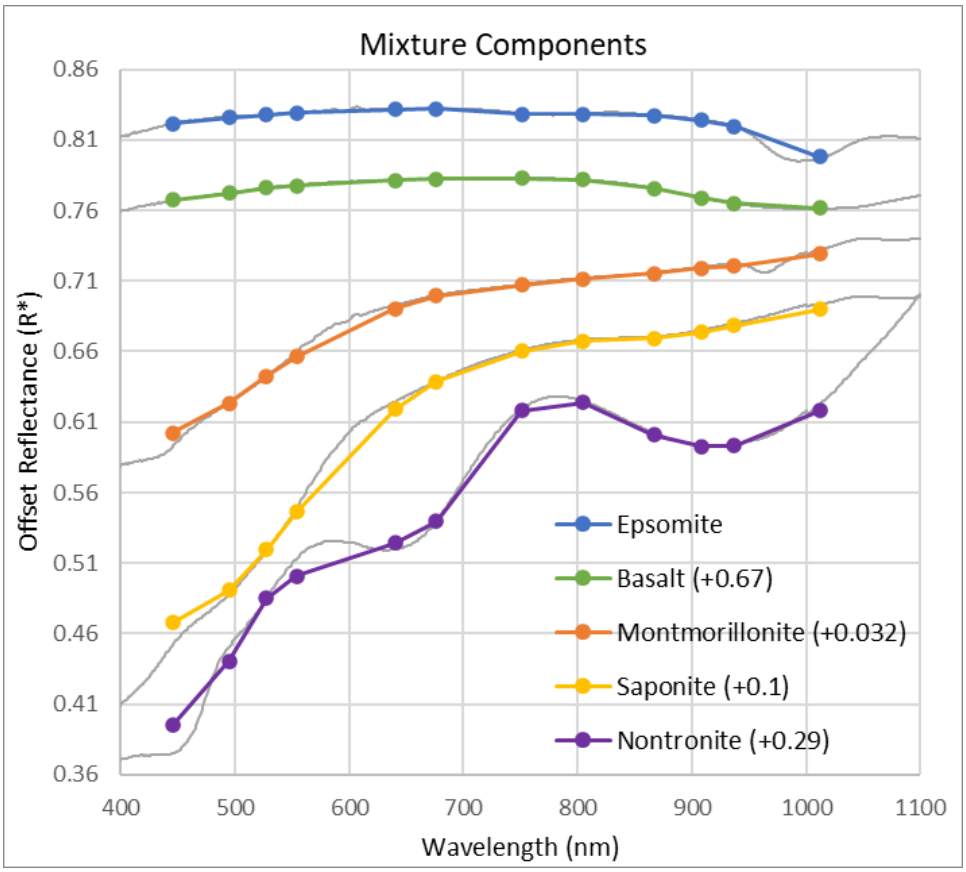

Figure 6: Spectra of mixture components with grain size of 75-106 µm. High-resolution spectra from the ASD spectrometer shown in gray. ASD spectra convolved to Mastcam wavelengths are shown in color.

Table 2: Materials used in laboratory mixtures

Material	Formula	Identified in:
Mg- Sulfates		
Epsomite	$MgSO_4 \cdot 7H_2O$	Rapin et al., 2019
Kieserite	$MgSO_4 \cdot H_2O$	Milliken et al., 2010 Smith et al., 2021 Sheppard et al., 2021
Hexahydrite	$MgSO_4 \cdot 6H_2O$	Rapin et al., 2019

Phyllosilicates		
Nontronite	$Na_{0.3}Fe_2((Si,Al)_4O_{10})(OH)_2 \cdot nH_2O$	Milliken et al., 2010 Carter et al., 2015
Montmorillonite	$(Na,Ca)_{0.33}(Al,Mg)_2(Si_4O_{10})(OH)_2 \cdot nH_2O$	Carter et al., 2015 Bridges et al., 2015
Saponite	$Ca_{0.25}(Mg,Fe)_3((Si,Al)_4O_{10})(OH)_2 \cdot n(H_2O)$	Carter et al., 2015 Bristow et al., 2018
Analogs		
Columbia River Basalts	Plagioclase, pyroxene, ilmenite, apatite, augite, olivine	Michalski et al,. 2006 Hoza, 2019 Curtis, 2022

Spectra were acquired using an Analytical Spectral Devices (ASD) FieldSpec 4 HiRes spectrometer connected to an ASD contact probe which has a fixed geometry of i = 12° and e = 35°. Following the methodology of Rice et al. (2010), we convolved each high-resolution laboratory spectrum to the filter bandpasses of Mastcam. These mixtures provided context when defining mineralogic interpretations of spectral classes and characterize the threshold at which Mastcam can detect hydrated Mg-sulfates. Additional high-resolution and convolved reflectance spectra from the UWPSF were also consulted in these analyses.

We started with 10 and 20 wt.% phyllosilicates in the mixtures with epsomite. After assessing the spectra of initial mixtures, we changed the wt. % of the phyllosilicate component to constrain the detection threshold. Small abundances of basalt were then introduced to simulate components of the mudstones in lower Mount Sharp and to assess the resultant dampening of spectral features. The resulting components and their proportions in each mixture are summarized in Supplemental Table 2.

IV. Results

We use principal component analysis to understand which aspects of the spectra, from GT to the rover's first encounter with the Amapari marker band, are contributing the most to the variability of the dataset. Once defined, these key spectral parameters correlated to principal

components are interpreted as a function of elevation to discern trends with stratigraphy. The resultant spectral variability is used to define new rock spectral classes in the context of spectra from our laboratory mixtures and pure minerals to make mineralogic interpretations (Section 5).

4.1. PCA of Mastcam Rock Spectra

In PCA of rocks in GT and the CST, 76.09% of the variance lies in PC1, 16.55% in PC2, 3.66% in PC3, and 2.19% in PC4, and 1.50% in remaining components (Table 3). PC1 versus PC2 is plotted in Figure 7, with each point representing a rock spectrum color-coded by stratigraphic member and the Amapari Marker Band. By inspecting spectra that are characterized by minimum and maximum PC values, we can identify which spectral features are contributing to the variability of the dataset. Examples of spectra with minimum and maximum component values are displayed in Figure 8. PC1 corresponds to the overall "redness" of rock spectra which can be quantified by the L3/L2 (751 nm/445 nm) ratio. The "redness" of rock surfaces – which can correlate with ferric components and/or dust cover – is the major control on spectral shape for rocks at all Mars landing sites, as shown in PCA results from the Mars Exploration Rover (MER) Pancams (e.g., Farrand et al., 2008), Curiosity's Mastcam in the early traverse (Rice et al., 2022b) and Perseverance's Mastcam-Z (Rice et al., 2023). PC2 is characterized by two spectral features: the peak NIR position and the 867 nm/751 nm ratio (Figure 8). The 867nm/751 nm ratio has previously been shown to correlate with phyllosilicate abundance in some instances (Jacob, 2022). The features that correlate with PC2 had not been a large contributor to the variability of Mastcam spectra from Curiosity's earlier traverse (Rice et al., 2022); we use this component, in part, to define a new spectral class (see Discussion section). PC3 corresponds to the 527 nm and 867 nm band depths and the 1012 nm/ 908 nm or 1013 nm/ 937 nm ratio. The latter did not significantly contribute to the variability of rock spectra in Curiosity's earlier traverse (Rice et al., 2022). PC4 is characterized by the 1012 nm/805 nm ratio.

Geologic formations in the CST and Marker Band Valley, specifically the Mirador formation, show greater amounts of spectra characterized by minimum PC2 in compared to those in GT (Figure 7). PC3 also contributes significantly to the spectral variability of the Mirador formation (Figure 7). Additionally, spectra from the Stimson formation and Amapari Marker Band are markedly characterized by smaller PC3 values (Figures 7,8).

Table 3: Principal components of rock spectra with minimum and maximum PC examples in Figures 7 and 8

PC	% Variance	Defining spectral characteristics	Max PC examples	Min PC examples
1	76.09	Overall redness (751 nm/445 nm ratio)	Joppa Shore (sol 2472); Edinburgh (sol 2726); Kilmaluag (sol 3209); Calder DRT (sol 3423)	Pitinga DRT (sol 3489); Omai (sol 3504); El Caura (sol 3558); Ilha Novo Destino (sol 3536)
2	16.55	Peak NIR position at 751 nm vs 908 nm or longward and the 867 nm/751 nm ratio	Edinburgh (sol 2726); Obar Dheathain (sol 2967); Saracura (sol 3643); Tucano (sol 3640)	Maria Gordon dump pile (sol 3247); Parepone (sol 3492); Micobie (sol 3579); Canaima tailings (sol 3613)
3	3.66	527nm and 867 nm band depths and the 1012 nm/908 or 937 nm ratio	Karia Island (sol 3565); Maraca (sol 3635); Shabono (sol 3672); Roxhinho (sol 3669)	Videix (sol 3143); Helmsdale Boulder (sol 3248); Linden (sol 3555); El Caura (sol 3558)
4	2.19	Overall NIR slope (1012 nm/805 nm ratio)	Obar Dheathain (sol 2967); Blis Et Born (sol 3202); El Caura (sol 3558); Arorouta (sol 3553)	Alba Dun Ara (sol 2313); Clyde Gannet (sol 2319); Groken DRT (sol 2907); Lagoa do Paraiso (3544)

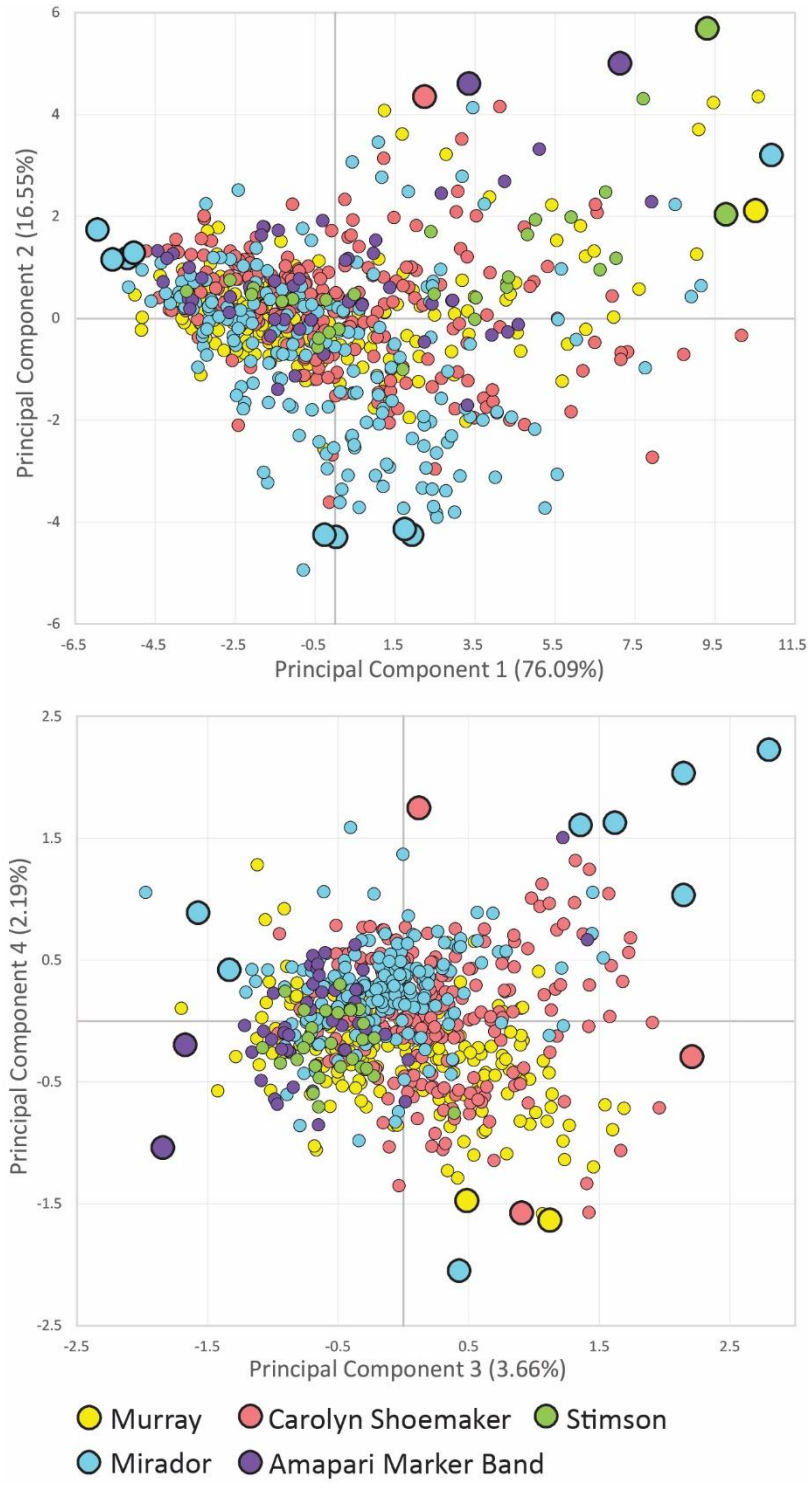

Figure 7: PCA results for all rocks in GT and CST (top panels), with GT rocks (middle panels) and CST rocks (bottom panels) shown separately to highlight the spectral differences with stratigraphy. Points are color-coded by formation. Larger circles indicate the minimum and maximum PC example spectra shown in Figure 8.

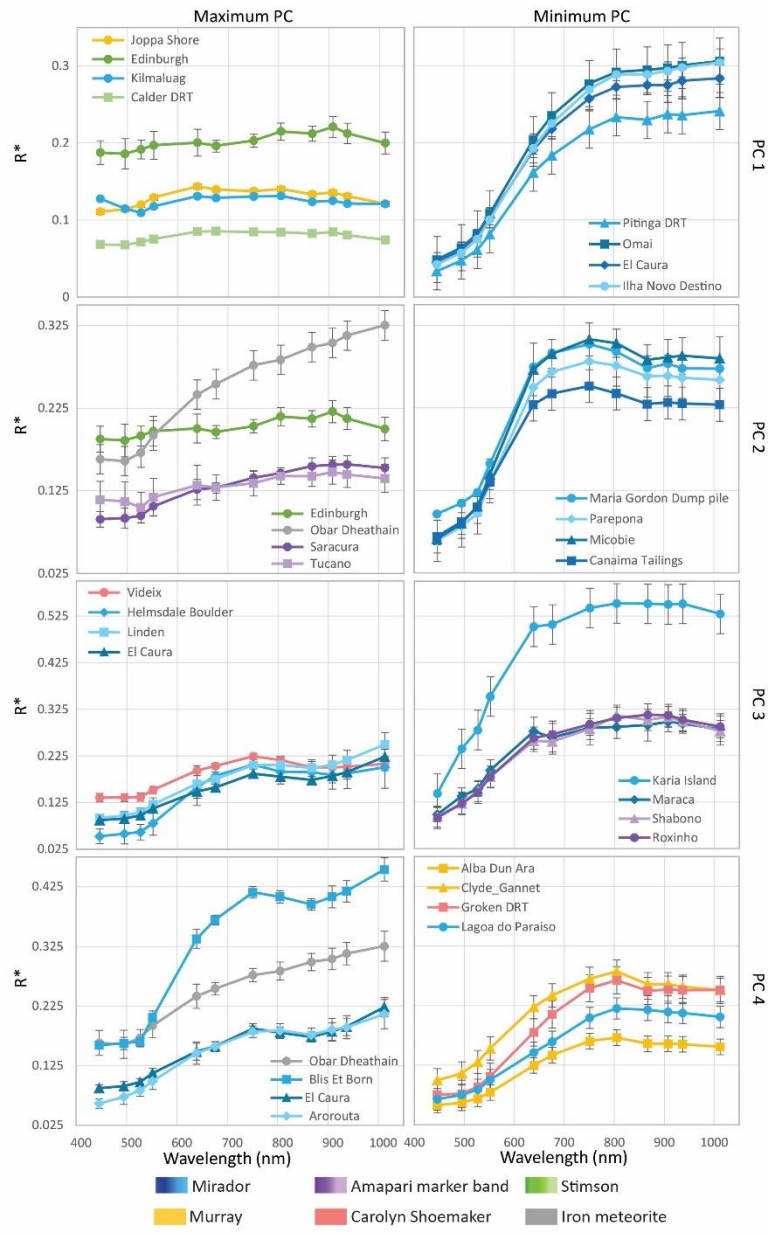

Figure 8: Example spectra for minimum and maximum PC values which correspond to the large points in Figure 7. Each row represents a different principal component, which is labelled to the right of the plots. Spectra are color-coded by stratigraphic formations, the Amapari marker band, and iron meteorites.

4.2. Trends with elevation, stratigraphy and dust cover

In order to assess spectral trends with stratigraphy, we analyzed key spectral features as a function of rover elevation. A larger percentage (67.27%) of rocks in the Mirador formation have 1013 nm/937 nm ratios < 1.0 in comparison to the rest of the traverse (Figure 9). Like spectra of rocks in the Murray formation, DRT targets don't have substantially different 1013 nm/937 nm ratios compared to dusty rocks. The dust-cleared targets and dusty counterparts between –3980 m and –3960 m with 1013 nm/937 nm ratios <~-0.96 are from GP. Like in the Jura member of the upper Murray, the 527 nm band depths in spectra of rocks in GT do not exhibit clear relationships with dust-cleared rocks (Figure 9). In the CST, the 527 nm band depths in spectra of rocks from upper Pontours to Contigo slightly increases in dust-cleared rocks, similar to that of Pettegrove Point in the upper Murray. Few rock spectra from GT and CST have 867 nm band depths > 0.05 overall; and few dusty rocks have 867 nm band depths > 0 compared to VRR in the upper Murray formation. In rock spectra from the CST, the effect of dust on the 867 nm band is drastically reduced by the DRT and in drill tailings in comparison to the rest of the traverse (Figure 9). The 867 nm band depths in spectra of dust cleared targets in Catrimani and Amapari exhibit smaller values than the rest of the Mirador formation.

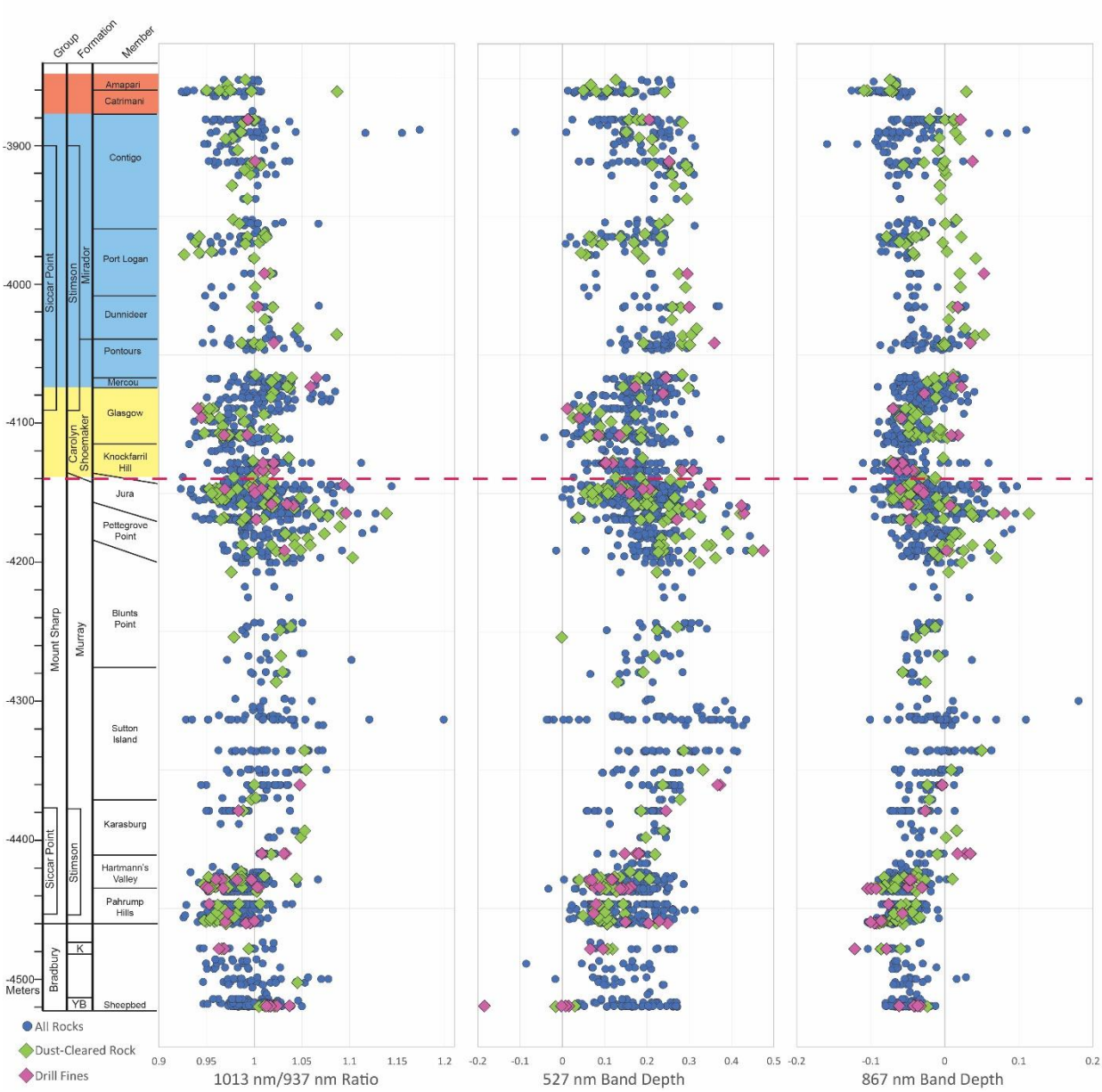

Figure 9: Spectral variability across Curiosity's traverse, for dust-cleared rocks (DRT targets, green diamonds), drill fines (pink diamonds) and all other rock targets (blue dots). Left: 1013 nm/937 nm ratio. Middle: 526 nm band depth. Right: 867 nm band depth. Points below red dashed line are observations synthesized by Rice et al. (2022); those above the red dashed line are from this study.

4.3. Laboratory Spectra

4.3.1. Epsomite and Montmorillonite

In a two-phase mixture of epsomite and montmorillonite, we find that the minimum wt. % epsomite needed to produce the R6 downturn (1013/937 nm ratio < 1.0) characteristic of the hydration in epsomite is 90 wt. %, which is consistent with the findings of Sheppard et al. (2022) (Figure 10). With the addition of 5 wt. % basalt, the 1012/937 nm ratio approaches 1.0. The 1012 nm/937 nm ratio in the epsomite-montmorillonite mixtures exceeds 1.0 at 20 wt. % montmorillonite. In mixtures with epsomite-montmorillonite ratios 90/10 and 80/20, the 1012/937 nm ratio > 1.0 is eradicated by 10 wt. % basalt powder. Key spectral features of pure basalt (e.g., broad pyroxene absorption due to Fe^{2+} longward of 1012 nm) are present in all mixtures with 10 wt. % basalt powder but are most prominent in the 80/20 epsomite-montmorillonite mixture with 10 wt. % basalt.

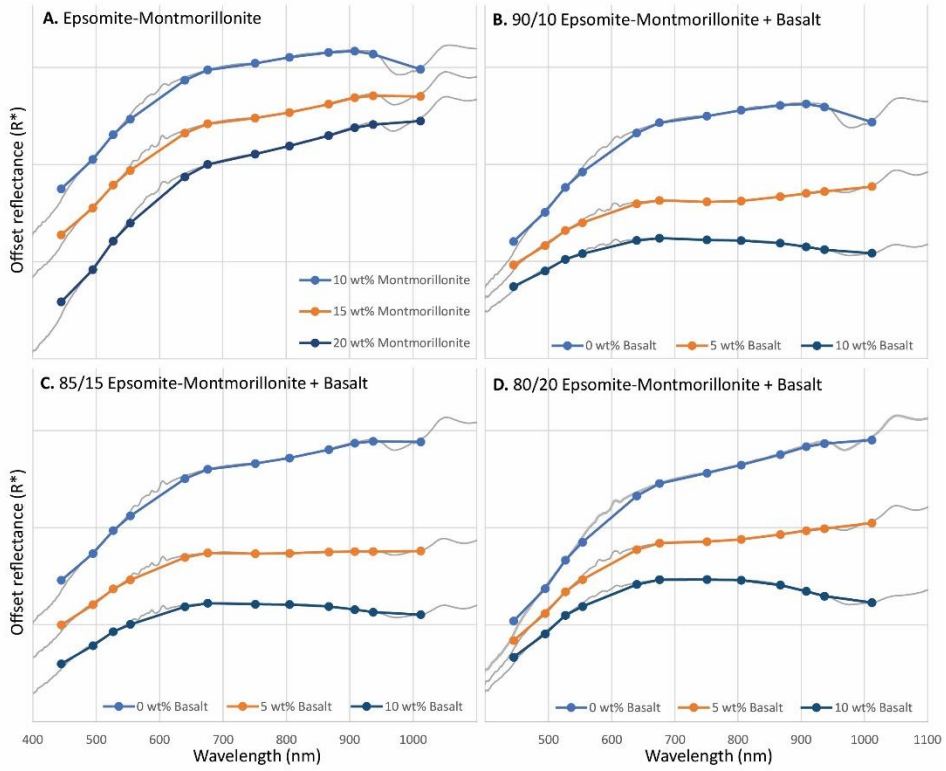

Figure 10: Epsomite-montmorillonite mixtures in (A) with 5 and 10 wt. % basalt additions in (B-D). Grey lines are high-resolution spectra from the ASD spectrometer. Blue, orange, and dark blue points represent the ASD spectra convolved to Mastcam bandpasses. Reflectance is offset for clarity and all Y-axes scales are equal. The 'wobbles' between 552 nm and 639 nm are a result of a known instrument artifact due to the order-sorting filters in the ASD spectrometer.

The R6 downturn due to epsomite is only present in the mixture with 90 wt. % epsomite and 10 wt. % montmorillonite.

4.3.2. Epsomite and Nontronite

In a two-phase mixture of epsomite and nontronite, the 1012 nm/937 nm ratio in the spectra convolved to Mastcam wavelengths is >1.0 in all mixtures (Figure 11). The most notable change with increasing nontronite wt. % is the increase of the 900 nm band depth and the 751 nm/ 527 nm ratio, increasingly negative 527 nm band depths, and the overall change in reflectance (i.e. spectra are flatter with more epsomite). The lower the wt. % nontronite in the two-phase mixtures, the stronger the effect that the basalt powder addition has on the spectra. In the 90/10 and 80/20 epsomite-nontronite mixtures with basalt powder additions, increasing basalt wt. % shifts the 900nm band center to 937 nm.

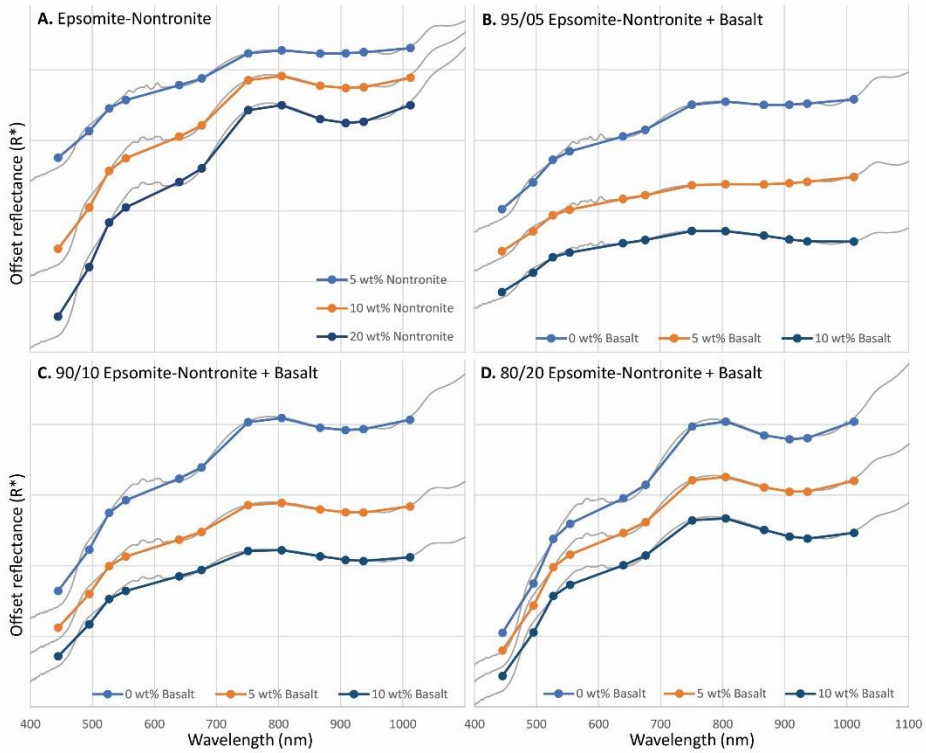

Figure 11: Epsomite-nontronite mixtures in (A) with 5 and 10 wt. % basalt additions in (B-D). Grey lines are high-resolution spectra from the ASD spectrometer. Blue, orange, and dark blue points represent the ASD spectra convolved to Mastcam bandpasses. Reflectance is offset for clarity and all Y-axes scales are equal. The 'wobbles' between 552 nm and 639 nm are a result of a known instrument artifact due to the order-sorting filters in the ASD spectrometer. The R6 downturn due to epsomite is not present in any of the mixtures with nontronite.

4.3.3. Epsomite and Saponite

In a two-phase mixture of epsomite (formula) and saponite (formula), there is a small 1012nm / 937 nm ratio in the spectra convolved to Mastcam wavelengths in the mixture with 5 wt. % saponite (Figure 12). As wt. % saponite increases, the overall slope reddens and the 1012 nm/937 nm ratio increases. In the 95/05 and 90/10 epsomite-saponite mixtures, increasing the basalt wt. % flattens the NIR slope. Increasing the basalt wt. % in the 80/20 epsomite-saponite mixtures produces convex NIR profiles with the most basalt-like spectrum being the 80/20 mixture with 10 wt. % basalt.

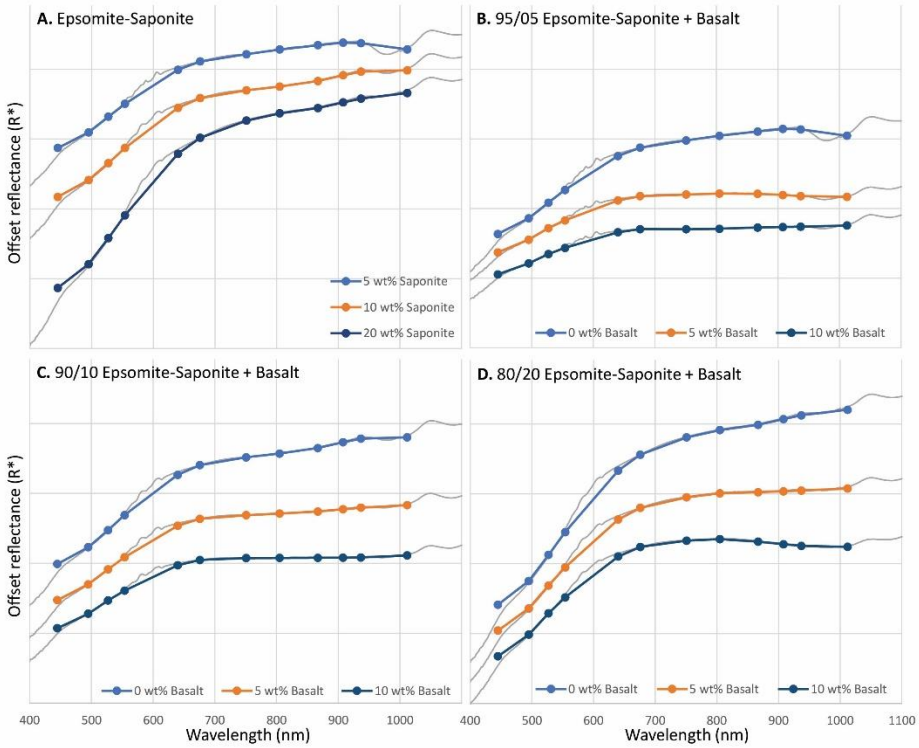

Figure 12: Epsomite-saponite mixtures in (A) with 5 and 10 wt. % basalt additions in (B-D). Grey lines are high-resolution spectra from the ASD spectrometer. Blue, orange, and dark blue points represent the ASD spectra convolved to Mastcam bandpasses. Reflectance is offset for clarity and all Y-axes scales are equal. The 'wobbles' between 552 nm and 639 nm are a result of a known instrument artifact due to the order-sorting filters in the ASD spectrometer. The R6 downturn due to epsomite is only present in the mixture with 95 wt. % epsomite and 5 wt. % saponite.

V. Discussion

5.1. New Rock Spectral Classes

Using a combination of PCA (section 4.1) and analyses of spectral trends with stratigraphy (section 4.2), we propose four new rock spectral classes that characterize GT, GP, CST, and MBV (Figure 13, Table 4); we refer to these as Classes J-M, with Classes A-L referring to those previously defined by Rice et al. (2022).

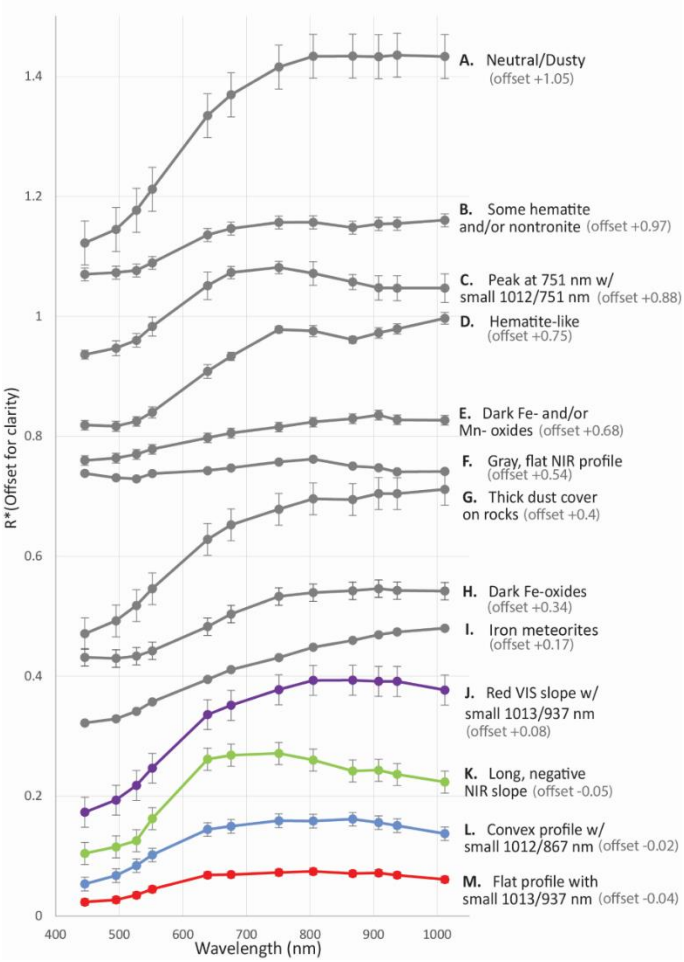

Figure 13: Example spectra of pre-established classes (A-I in gray) from Curiosity's traverse from landing through Vera Rubin Ridge (Rice et al., 2022); and newly defined classes (J-M in purple, green, blue, red) from Curiosity's traverse from Glen Torridon to the Amapari Marker Band.

Table 4: Summary of rock spectral classes

Class	Defining spectral characteristics	Type examples	Distribution	Interpretation
A. Neutral/Dusty	Moderate 751 nm/445 nm ratios; Small values of 1012 nm/751 nm ratio; Flat NIR profiles	sol 183, mcam00993	Consistent throughout the traverse	Variable amounts of dust upon rocks with neutral spectra
B. Some hematite and/or nontronite	Large 751 nm/445 nm ratios; Small values of 1012 nm/751 nm ratio; Positive 867 nm band depths	sol 1425, mcam07034	Prevalent in the Murray, Carolyn Shoemaker, and Mirador formations	Rocks bearing some red hematite and/or nontronite
C. Peak at 751 nm with small 1012 nm/751 nm ratio	Peak reflectance at 751 nm; Small 1012/751 nm ratios; Positive 867 nm band depths	sol 1524, mcam0770	Primarily within the Sutton Island member and the CST	Dark, diagenetic features, possibly nontronite-bearing
D. Hematite-like	Large 867 and 527 nm band depths	sol 1885, mcam09853	Mostly within the Sutton Island and Jura members, with significant local variability	Strongly diagenetically-altered rocks containing red hematite, nontronite and/or ferric phases
E. Dark Fe- and/or Mn- oxides	Straight, flat to positively sloping profiles to 908 nm; 908 nm/1013 nm < 1.0	sol 626, mcam02676	Primarily within the Kimberley formation, Pahrump Hills member, and the Amapari marker band	Rocks with variable contributions of dark Fe- and/or Mn-oxides
F. Gray, flat profile	1012 nm/751 nm ratios close to 1.0; blue/red ratios positive or close to 1.0; often has a small 527 nm >1.0 and peak at 805 nm.	sol 1120, mcam04990	Drill fines, mostly within the Stimson formation	Rock interiors with minimal spectrally neutral phases (e.g., crystalline SiO_2, magnetite)
G. Thick dust cover on rocks	Large 751 nm/445 nm ratios; Positive 1012 nm/751 nm ratios; no 867 nm band depth	sol 069, mcam00486	Seen within Bradbury Group and CST	Thick dust cover on rock surfaces
H. Iron meteorites	1012 nm/751 nm ratios >1.1; 741 nm/527 nm ratios 1.0–2.0	sol 640, mcam02718	Isolated float rocks, found sporadically at all elevations	Iron meteorites
I. Dark Fe-oxides	Large 527 nm band depth; flat NIR profile	sol 758, mcam03257	Only seen within Pahrump Hills member	Dark Fe-oxide, possibly coarse-grained hematite
J. Red VIS slope with small 1013 nm/937 nm ratio	Neutral/Dusty-like spectra but with 1013 nm/937 nm ratios <1.0	sol 3643, mcam03029	Only seen within the Amapari marker band and its float rocks	Hydration in dust at certain viewing geometries

K. Long, negative NIR slope	Positive 527 nm band depths; continuously negative slopes from 676 nm or 751 nm to 1013 nm; sometimes exhibits positive 867 nm band	sol 3606, mcam02817	Seen in Sutton Island, Glasgow, CST, and Catrimani	Targets with strong diagenetic overprints; primarily ferrous component; hematite and/or goethite; secondary iron-rich mineral (nontronite and/or amorphous Fe-sulfate)
L. Convex profile with small 1012 nm/867 nm ratios	Convex profile; 1012 nm/867 nm ratios <1.0; 527 nm band depths close to 0; negative 867 nm band depths.	sol 3642, mcam03022	Only seen within the Amapari marker band and its float rocks	Clinopyroxene
M. Flat profile with small 1013 nm/937 nm ratios	Flat profile; 1013 nm/937 nm ratios <1.0; no obvious peaks; red/blue ratios close to 1.0	sol 3423, mcam01696	Primarily of dark surfaces on the Greenheugh Pediment	Relatively unaltered basaltic mineralogy with magnetite and possibly microplaty hematite

Class J ("Red VIS slope with small 1013nm/937 nm ratio" class; Figure 13) is characterized by positive slopes in visible wavelengths, like Class A, but with a distinct R6 downturn in the last two wavelength filters, potentially indicative of hydration (Rice et al., 2010). Class K displays negative slopes from 639-751 nm to 1012 nm and positive 527 nm band depths. Class L ("Convex profile with small 1012 nm/867 nm ratio" class) displays a shallower red VIS slope in comparison to classes A and J, with a very small positive slope from 639 nm to 867 nm and a small 1012 nm/867 nm ratio. Class M ("Flat profile with small 1013nm/937 nm ratio" class) displays some of the flattest spectral profiles of rocks across the entire traverse with a small 1013 nm/937 nm ratio and in many cases, a very small 867 nm band depth.

The parameters that best distinguish the new classes from each other (and previously established classes) are the 1013 nm/937 nm and 867 nm/676 nm ratios (Figure 14). A greater amount of rock spectra from CST have 1013 nm/937 nm ratios < 1.0, which is consistent with PC3. The 867 nm/676 nm ratio characterizes the spectral shape between these two wavelengths and is also a variation on PC2. Parameters concerned with smaller wavelength features do show variations but do not appear to be as useful for distinguishing like-spectra from the rest of the dataset.

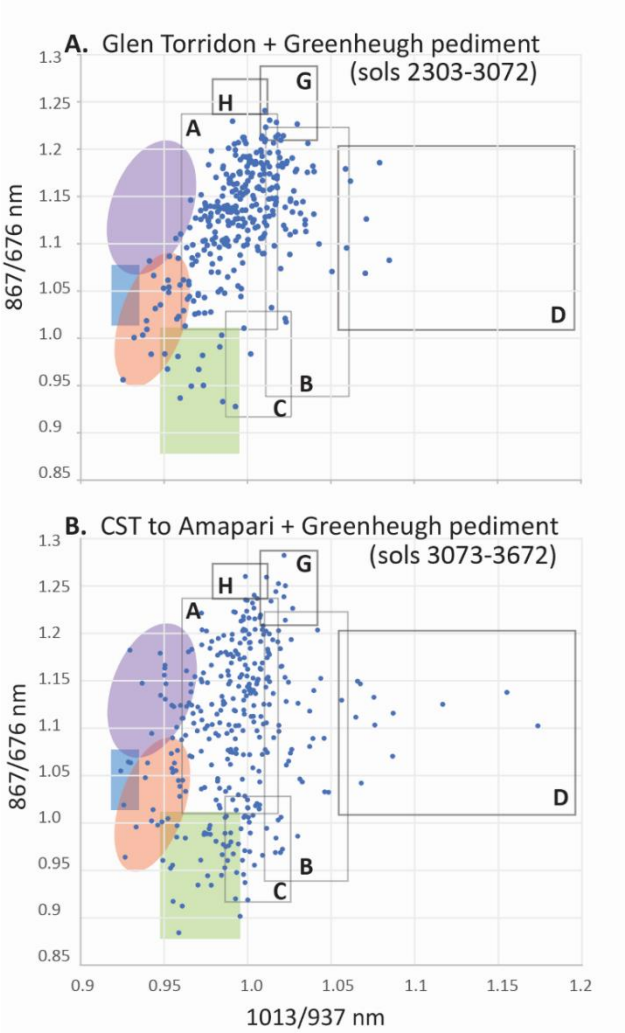

Figure 14: 1013/937 nm ratio plotted against the 867/676 nm ratio with class regions for observations in (A) Glen Torridon and Greenheugh pediment; and (B) the clay-sulfate transition through the first encounter with Amapari and Greenheugh pediment. Regions outlined in light gray are pre-established classes using Mastcam spectra from landing to VRR (Rice et al., 2022). Colored regions are newly defined classes using data collected post VRR: purple is Class J, green is Class K, blue is Class L, and red is Class M. Regions correspond to classes in Figure 13. 1013/937 nm ratios less than 1 with otherwise flat NIR profiles are consistent with a hydration band at ~980 nm (Rice et al., 2010). The 867/676 nm ratio characterizes spectral shape and helps distinguish flatter spectra from peaks or shoulders. Note that the pre-established classes "Dark Fe- and/or Mn- oxides", "Gray, flat NIR profile", and "Iron meteorites" are not highlighted by these spectral parameters

5.2 Distributions of classes with stratigraphy

We find notable distributions of pre-established and new classes throughout GT, CST, and the Amapari Marker band. GT is primarily characterized by Class B with some occurrences of Class C, D, F, G, and K (Figures 15,16). The Glasgow member in GT is marked by the occurrence of Classes D and K; both of which signify alteration and are consistent with the findings of diagenesis in the Glasgow member (Rudolph et al., 2022; Bennet et al., 2022). Above Glasgow and GT, Class J appears in accordance with significantly dusty rocks on and around Mount Mercou (Figure 16). The occurrence of Class B persists through the CST, but along with it the abundance of Classes C and K increases (Figure 16). Classes K and C occur in CST more than GT (Figure 15C,E and 16) and can be correlated to higher abundances of nodules, dark-toned fins, and diagenetic overprints (Figure 17) (Rice et al., 2022). Class M directly corresponds to the rover's excursions onto Greenheugh Pediment, which is a part of the Stimson formation, and float rocks leading up to the pediment (Figure 15). One exception is the Hutton drill just below the Carolyn Shoemaker formation/Stimson unconformity in a relatively lighter-toned area (Thorpe et al., 2022). Class M spectra are typically of smooth, dust-removed, dark gray surfaces (Figure 17).

Moving up section into MBV, we see the occurrence of Classes C and K persist in accordance with diagenetic features. In the marker band itself, two new spectral classes appear. Spectra classified as J are from the lower rippled and upper rhythmic units of the Amapari marker band and its respective rippled floats just below (Figure 15F and Figure 16). Class J spectra are from primarily dusty, eroded surfaces on the Amapari marker band (Figure 17). Similar to Class J, Class L only occurs within the Amapari marker band or its respective float rocks (Figure 15F and Figure 16). Class L spectra are from targets with slightly lighter-toned and relatively matte surfaces from the rippled unit of the Amapari marker band (Figure 17). Class E occurs in accordance with the dark, shiny surfaces on the rippled unit of the Amapari marker band, which is consistent with its pre-established mineralogic interpretation and ChemCam and APXS results of higher MnO and FeO abundances (Gasda et al., 2023; Weitz et al., 2023) (Figure 16).

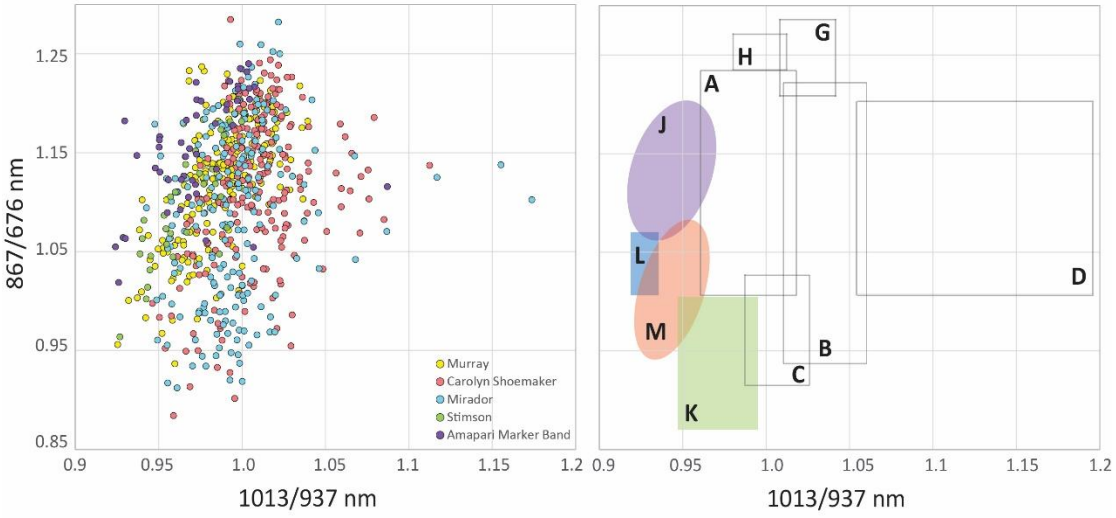

Figure 15: (Left) Parameter plot in Figure 14 with point color-coded by formation or feature. (Right) Class regions. Mirador displays the most variability and has the greatest amount of rock spectra plotting in Classes K and C; rock spectra from Stimson are consistent with Class M; rock spectra from Amapari marker band are consistent with Classes J and L.

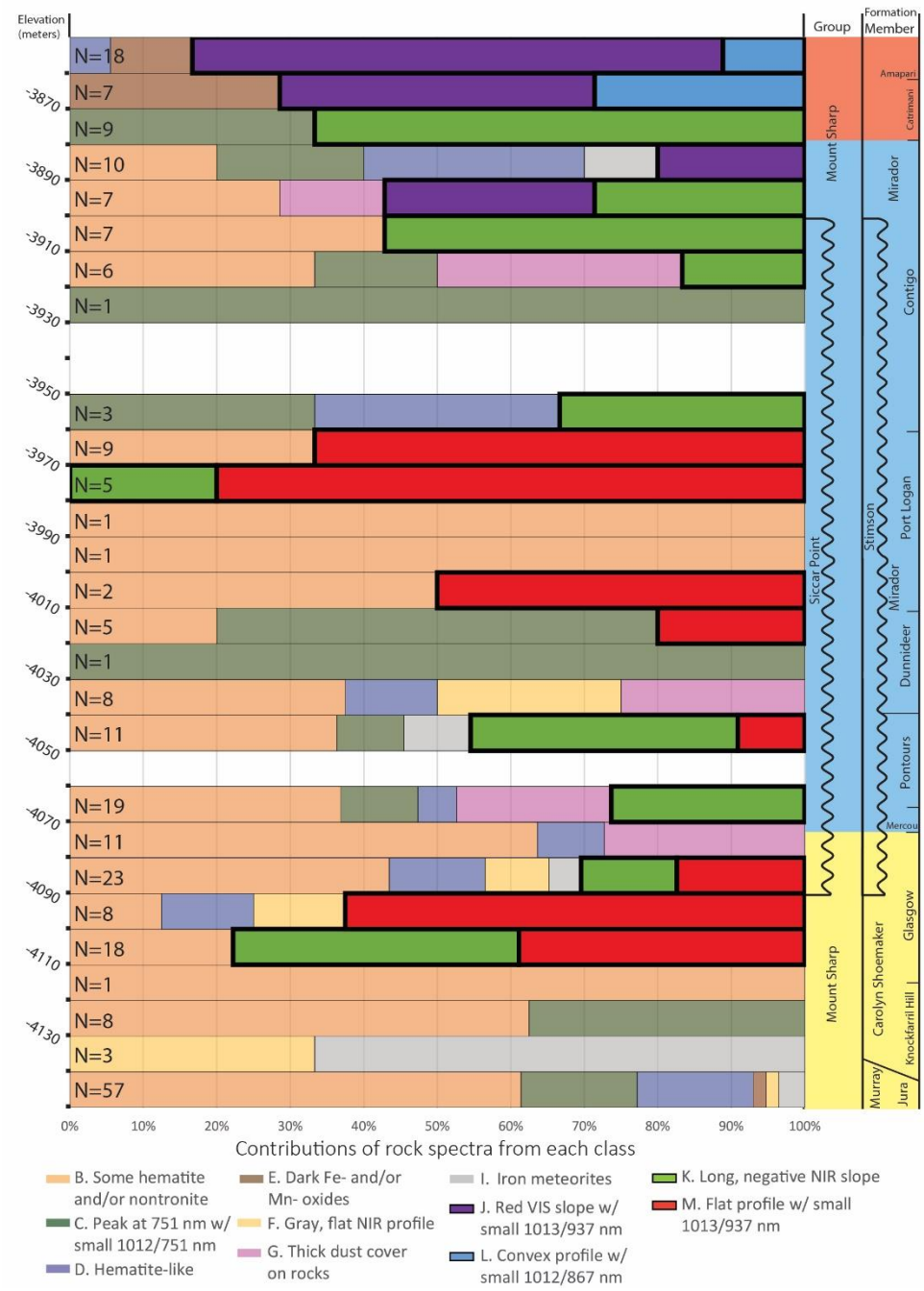

Figure 16: Distribution of rock spectral classes with elevation across Curiosity's traverse from Glen Torridon to first encounter with the Amapari marker band (omitting the Neutral/Dusty class) with newly identified classes in bold. Data are binned to 10 m elevation intervals. Percentage values indicate proportions of rock spectra belonging to each class within the elevation bin. Classes J and L are localized to Amapari marker band. Class M is consistent with excursions onto Greenheugh pediment and float rocks in its approach. Class K corresponds to regions with diagenetic overprints and features (Figure 19).

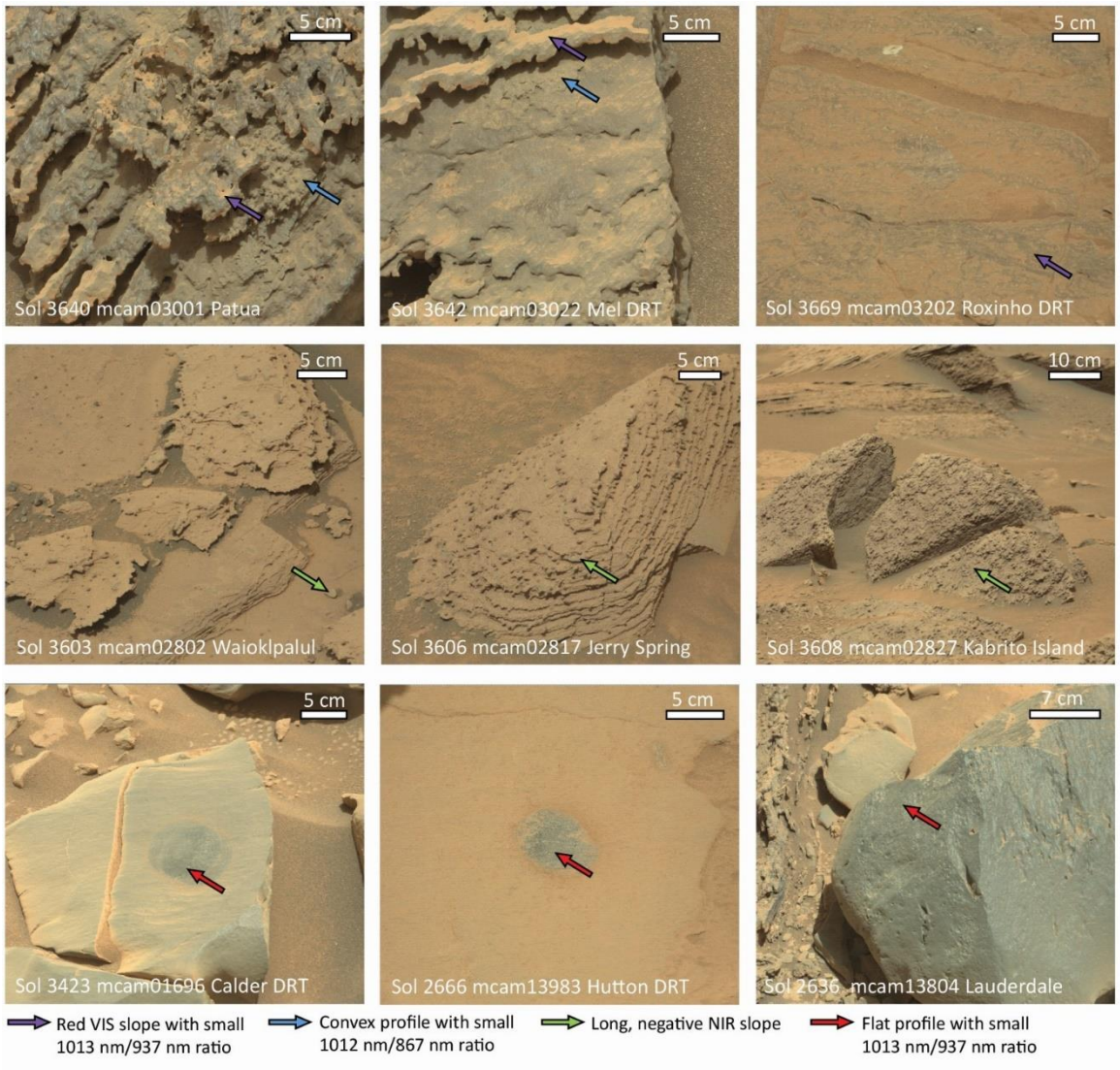

Figure 17: Examples of primary surface types in each newly defined class. “Red VIS slope with small 1013 nm/937 nm ratio” class is inherent to the rippled and rhythmically laminated units of the Amapari marker band. The “Convex profile with small 1012 nm/867 nm ratio” class is inherent to relatively lighter toned surfaces on the rippled unit of the Amapari marker band. The “Long, negative NIR slope” class is inherent to surfaces with strong diagenetic overprints. The “Flat profile with small 1013 nm/937 nm ratio” class is inherent to dark gray surfaces on the Greenheugh pediment and floats in its approaches.

5.3. Comparisons to Lab Spectra and Mineralogic Interpretations

In order to make mineralogic interpretations of the newly defined classes, we consult laboratory spectra of pure minerals and the mixtures analyzed in this study. Specifically, we take Mastcam-convolved spectra of pure minerals and plot them using the same parameters described above to understand how the pure minerals influence the spectral features that characterize the classes (Figure 18).

5.3.1 Class J

Of these candidate mineral contributors, Ca-pyroxenes and epsomite best explain the location of Class J in this parameter space (Figure 18). Class J is localized to the marker band, where detections of high-Ca pyroxenes have been made from orbit, and occurs on primarily dusty surfaces (Weitz et al., 2022; see section 5.2.3). However, laboratory experiments have shown that it is unlikely that a mixture of ferric dust and pyroxenes would result in small enough 1013 nm / 937 nm ratios to reproduce the R6 downturn that defines Class J (Cloutis et al., 2000). Evidence from other instruments for lack of sulfates in the majority of marker band targets (Gasda et al., 2023; Weitz et al., 2023; Rampe, personal communication), and the results of our laboratory mixtures, support that the R6 downturn in Class J is not due to hydrated Mg-sulfate. Furthermore, DRT targets in the MB don't have substantially different 1013 nm/937 nm ratios compared to dusty rocks (Figure 9) which implies that the ratio cannot be attributed to Mg-sulfate or an underlying material. Spectra similar to those Class of J from MER Spirit's Pancam (Rice et al., 2010; Johnson et al., 2021) and Perseverance's Mastcam-Z (Rice et al., 2023) have been noted on dust-coated rock surfaces and are attributed to hydration in dust at certain viewing geometries; we propose that this explanation is reasonable for the Class J spectra here as well.

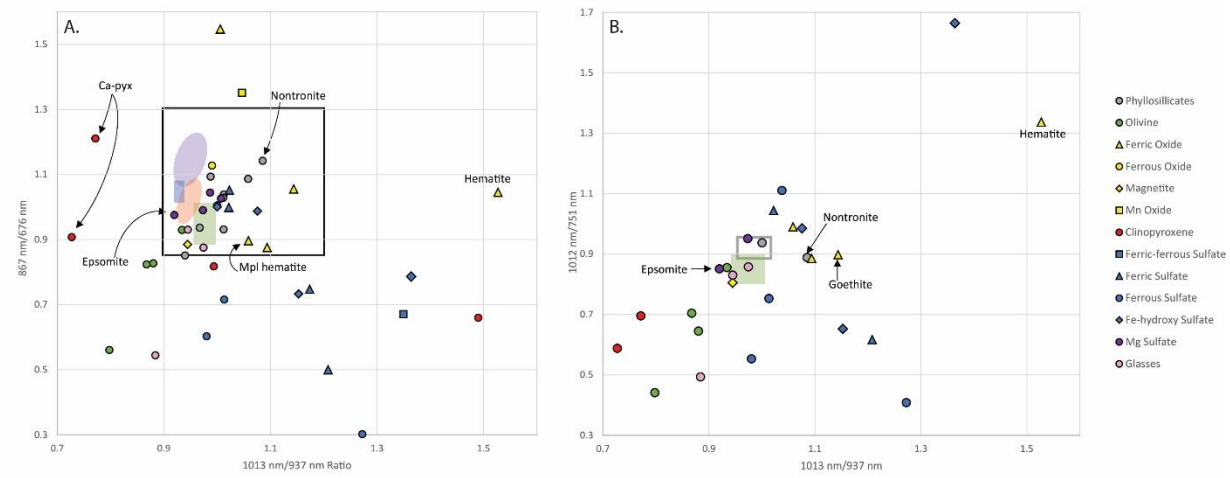

Figure 18: Parameter plot of pure mineral spectra using (A) 1013 nm/937 nm and 867 nm/676 nm ratios and (B) 1013 nm/937 nm and 1012 nm/751 nm ratios. A select few minerals are shown in (B) in order to further contextualize Class K. The box outlined in black in (A) is the parameter space that Mastcam observations from sols 2303-3672 encompass. Colored regions correspond with new classes like in Figure 14; purple is Class J, blue is Class L, red is Class M, green is Class K. Gray outline in (B) encompasses class C and is highlighted in order to distinguish mineralogic interpretations between classes K and C.

5.3.2 Class K

A primary ferrous mineral (e.g., olivine, pyroxene) and/or basaltic glasses are consistent with the shape of Class K (Haber et al., 2022) (Figures 5,18). Given that the diagenetic features inherent to Class K are Mg-sulfate-rich (Gasda et al., 2023); and the dust-removed APXS targets classified as Class K exhibit relatively low FeO abundances, it is more likely that a basaltic component influences – but is not the sole contributor to - the reflectance spectra. A minor basaltic component of Class K is further supported by our laboratory mixtures in which just 5-10 wt % basalt powder reduces the NIR slope when added to two phase mixtures of epsomite and phyllosilicate (See section 4.3). The only other stratigraphic members in which Class K has been identified are the sulfate-enriched Sutton Island (Haber et al., 2022) and the diagenetically altered Glasgow (Rudolph et al., 2022), implying that a unique secondary phase may be contributing to the spectral shape. Furthermore, Class K is primarily associated with diagenetic features in the CST where rocks have large fractions of amorphous sulfur-bearing phases that are likely mixtures of Mg-, Fe-, and possibly Ca-sulfates or sulfites (Gasda et al., 2023; Smith et al.,

2022). Thus, considering crystalline Fe-sulfate was not detected by CheMin in the CST, we investigate the influence an amorphous Fe-sulfate component may have on the spectra.

Using the Sample Analysis at Mars instrument-Evolved Gas Analysis, Clark et al. (2023), found that all 7 drill samples in the CST evolved broad SO2 releases consistent with Fe-sulfates, which either occurred in the amorphous component or were present in abundances lower than CheMin's detection limit. If contributing to Class K, a ferric sulfate present in the amorphous component would need to be in amounts small enough to preserve the negative NIR slope, considering the positive NIR slope inherent to most amorphous phases (Sklute et al., 2015). Alternatively, there could be a relatively larger amount of an amorphous ferrous or Fe-hydroxy sulfate contributing to the shape of Class K- both of which are consistent with negative NIR slopes or 1012 nm/751 nm ratios <1.0 (Sklute et al., 2015; Bishop et al., 2021) (Figures 5,18). Furthermore, VNIR spectra of an amorphous ferric sulfate precipitated onto a flood basalt produced longer negative NIR slopes in comparison to the uncoated sample (Sklute et al., 2015), which we propose is consistent with Class K.

The addition of an Fe-sulfate phase alone would not produce the 527 nm bands in many spectra defined as Class K. Thus, potential ferric iron-bearing minerals that could contribute to the 527 nm bands in Class K, while preserving the negative slope from 676 or 751 nm to 1013 nm, include nontronite, goethite (Cloutis et al., 2006), magnetite, and/or small amounts of hematite (Figures 5, 18B). With increasing grain size, nontronite and goethite Fe^{3+} spin forbidden absorptions around 900 nm shift right and/or broaden (Turenne et al., 2023; UWPSF), which in turn reduces the NIR slope in convolved Mastcam spectra and is consistent with Class K. In our nontronite-epsomite mixtures, the positive slope of the right shoulder inherent to an Fe^{3+} absorption (1012 nm/867 nm ratio) approaches 1.0 with increasing epsomite and basalt abundances, which may reflect the shape of Class C that we found to correlate with Mg-sulfate strata in our APXS investigation (see section 5.5). Considering Class K's relationship to Class C (similar surfaces and stratigraphic distribution), Class C may be characterized by a larger amount of hematite, nontronite, or amorphous ferric sulfates, which are consistent with larger 1012 nm/751 nm ratios (Figure 18B) (Sklute et al., 2015). Thus, given the disappearance of phyllosilicates in CheMin data starting at the Maria Gordon target (sol 3226), Class K may be characterized by a primary ferrous component with: (1) coarse-grained ferric oxides (e.g.,

goethite and hematite), and an amorphous Fe-sulfate component post sol 3226; and (2) nontronite, hematite, and an amorphous Fe-sulfate component pre sol 3226. Furthermore, Class K resembles the "Newberry" class inherent to spherules in the Matijevic formation encountered by the Opportunity rover and identified by Farrand et al. (2014); both interpretations of these classes are consistent with a ferric mineral component.

5.3.3 Class L and M

Several factors support a mineralogic interpretation of Ca-rich pyroxene for Class L. First, Class L is only found in the pyroxene-rich Amapari Marker Band (see section 5.2.3; Weitz et al., 2023). Second, the 1012 nm/867 nm ratios <1.0 is consistent with the shape of Ca-rich pyroxene. Lastly, the region in parameter space associated with Class L is characterized by the position of Ca-rich pyroxenes, augite and diopside. Class M spectra are consistent with olivine, magnetite and possibly microplaty hematite (Figure 18). The locations, surfaces, and compositions of Class M support a primarily basaltic component with increased alkalis (See sections 5.5) and low Chemical Index of Alteration (CIA, Dehouck et al., 2022), which is consistent with the lack of Fe^{3+} absorptions in Class M spectra (Rudolph et al., 2022). Like for Class J, the laboratory mixtures described here and by others (Jacob, 2022) - in addition to results from other Curiosity instruments (see sections 5.4-5.5 below) - support the interpretation that the 1013 nm/937 nm <1.0 in Class M is not due to hydrated Mg-sulfate. Instead, the 1013 nm/937 nm <1.0 may be attributable with the broad, weak band around 1000 nm inherent to magnetite, olivine, and/or pyroxene (Figure 5).

5.3.4 Consulting laboratory mixtures to assess Mg-sulfate influence

The results of our experimental mixtures, along with localities and chemical data, support that a small (<1.0) 1013 nm/937 nm ratio in spectra from the CST is not consistent with Mg-sulfates. However, this does not mean that there are no Mg-sulfates present, considering the ease at which the narrow hydration feature near 1000 nm is masked in Mastcam wavelengths; spectra without R6 downturns, therefore, should not be considered "Mg-sulfate-free". The ~1000 nm feature is present in the laboratory spectra of 95/05 and 90/10 epsomite-saponite, the 95/05 epsomite-saponite with 5 wt. % basalt, and the epsomite-montmorillonite mixtures. However, Mastcam would not detect some of these features (i.e., spectra convolved to Mascam bandpasses do not have an R6 downturn) due to (1) the positive NIR slopes of montmorillonite and saponite

increasing the reflectance of the right shoulder of the 1000 nm feature in epsomite and (2) the saponite and basalt reducing the band depth of the 1000 nm feature in epsomite. It is challenging to attribute the feature in the epsomite-montmorillonite mixtures to just epsomite, considering that montmorillonite also has a small hydration feature around 1000 nm as well (Figure 6). In the ASD spectra of 95/05 and 90/10 epsomite-nontronite mixtures, the 1000 nm feature inherent to epsomite slightly overprints on the broader 900 nm band inherent to nontronite and is not likely to be detectable by Mastcam. CheMin identified the crystalline Mg-sulfate, starkeyite ($MgSO_4 \cdot 4H_2O$), in the Canaima drill (see Section 5.4 below). However, hydrated Mg-sulfates with less structurally bound water molecules than epsomite are expected to require even less of these other materials to mask their 1000 nm hydration features. Thus, it is unlikely that Mastcam will be able to detect a hydrated Mg-sulfate unless the target is near pure hydrated Mg-sulfate (e.g., crystal, vein).

5.4. Classification of CheMin target drill fines

During the traverse from Glen Torridon to the first encounter with the Amapari marker band, Curiosity drilled 17 outcrop targets that were analyzed by the CheMin instrument (Table 5, Figure 19). Consistent with their masking effects, high contributions of phyllosilicates (26-34 wt. %) characterize spectra of drill fines classified as A (Figure 19), which are localized to GT. The spectral classification of the Aberlady (AL) and Kilmarie (KM) drill fines as Class B, low wt. % of hematite in Aberlady and Kilmarie, and high wt. % of phyllosilicates implies a ferric phyllosilicate (e.g., nontronite) contribution (Rudolph et al., 2022) (Figure 19). Spectra of the Edinburgh (EB) drill fines are classified as Class E which is consistent with the 14 wt. % magnetite identified by CheMin (Figure 19). Both magnetite (12.4 wt. %) and hematite (4.8 wt. %) characterize the spectra of the Hutton (HU) drill fines, which are classified as M (Figure 19). The flatness of the Hutton spectra in comparison to the Edinburgh spectra may be attributable to more MnO in Edinburgh (Thompson et al., 2022a&b) and coarse-grained microplaty hematite in Hutton. Spectra of coarse grain sizes of hematite, which are gray in color, display small to negative 867 nm band depths and 640 nm/527 nm ratios closer to 1.0 in comparison to red crystalline hematite (Horgan et al., 2020; Lane et al., 2002). Avanavero (AV) and Maria Gordon (MG) have similar mineralogic proportions but are classified as B and C, respectively (Figure

19). The different classifications of Avanavero and Maria Gordon may be attributable to the slightly higher amount of goethite in Avanavero and/or different amorphous materials (e.g., proportions of Mg- and or Fe- sulfates (Clark et al., 2023)). All CheMin targets classified as C have some goethite and hematite, which is consistent with the minerals' convolved VNIR reflectance peaks at 751 nm. No drill fines included in this study and analyzed by CheMin are classified as the new classes J, K, or L.

Table 5: Summary of CheMin Samples (Rampe et al., 2023; Thorpe et al., 2022; Cardenas et al., 2023) and the Mastcam Spectral Classes Assigned to Their Associated Drill Tailings and/or Dump Piles

Abbreviation	CheMin sample	Sol(s)	Formation	Proposed Depositional Environment	Mastcam rock spectral class
AL	Aberlady	2370	Murray	Lacustrine	B. Some hematite and/or nontronite
KM	Kilmarie	2384	Murray	Lacustrine	B. Some hematite and/or nontronite
GE1	Glen Etive	2486	Carolyn Shoemaker	Fluvial	A. Neutral/Dusty
GE2	Glen Etive 2	2527	Carolyn Shoemaker	Fluvial	A. Neutral/Dusty
HU	Hutton	2669	Carolyn Shoemaker	Lacustrine/lake margin	M. Flat profile w/ small 1013/937 nm ratio
EB	Edinburgh	2713	Stimson	Ancient aeolian	E. Dark Fe- and/or Mn-oxides
GG	Glasgow	2754	Carolyn Shoemaker	Lacustrine/lake margin	C. Peak at 751 nm w/ small 1012/751 nm ratio
MA	Mary Anning	2838	Carolyn Shoemaker	Fluvial	A. Neutral/Dusty

MA3	Mary Anning 3	2870	Carolyn Shoemaker	Fluvial	A. Neutral/Dusty
GR	Groken	2912	Carolyn Shoemaker	Fluvial	A. Neutral/Dusty
NT	Nontron	3055	Carolyn Shoemaker	Fluvio-lacustrine	B. Some hematite and/or nontronite
BD	Bardou	3094	Carolyn Shoemaker	Fluvio-lacustrine	D. Hematite-like
PT	Pontours	3170	Carolyn Shoemaker	Fluvio-lacustrine	B. Some hematite and/or nontronite
MG	Maria Gordon	3226	Mirador	Eolian	C. Peak at 751 nm w/ small 1012/751 nm ratio
ZE	Zechstein	3289	Mirador	Eolian	B. Some hematite and/or nontronite
AV	Avanavero	3509	Mirador	Eolian	B. Some hematite and/or nontronite
CA	Canaima	3612	Mirador	Eolian	C. Peak at 751 nm w/ small 1012/751 nm ratio

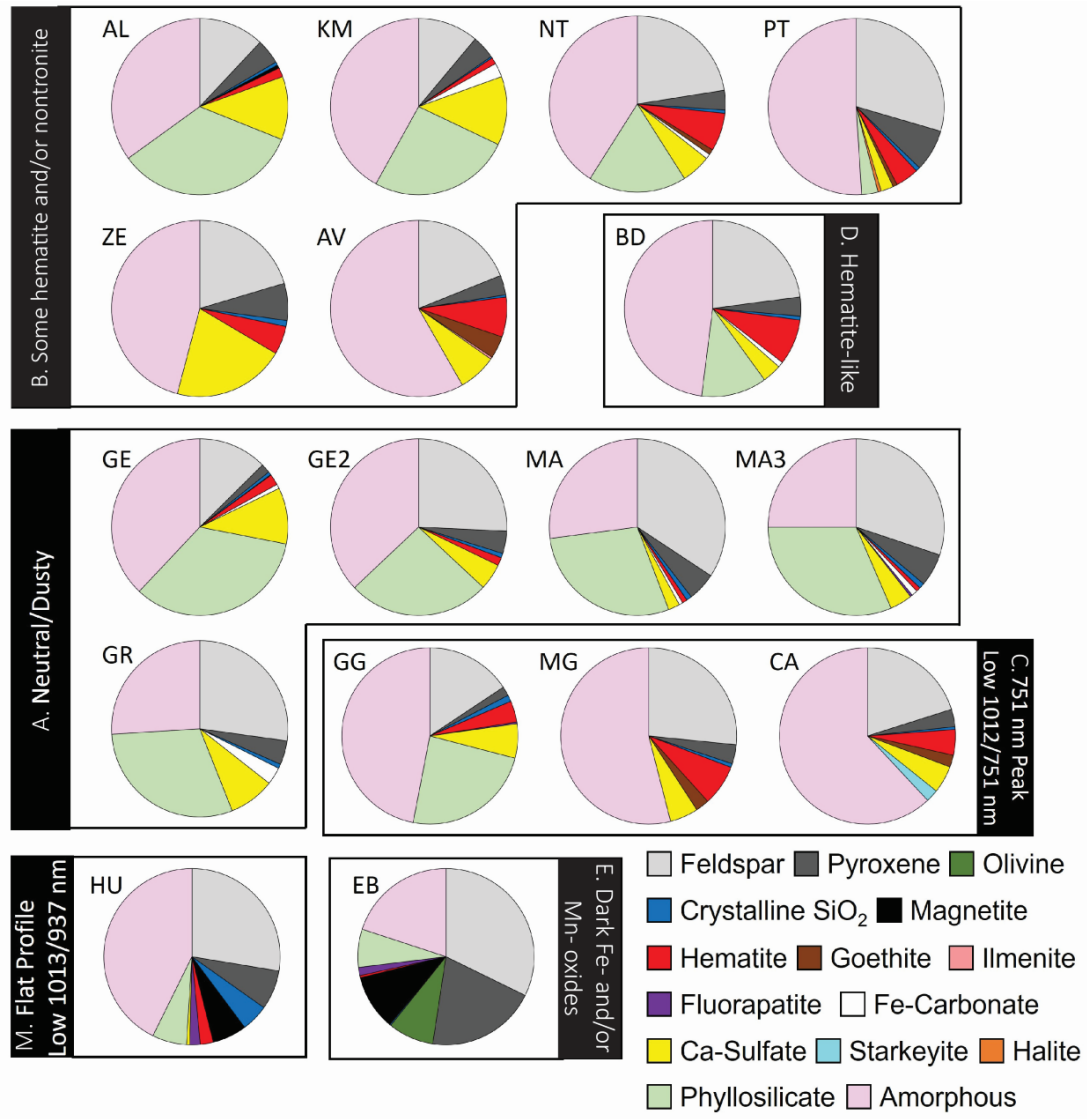

Figure 19: Mineral abundances of CheMin samples (Thorpe et al., 2022; Rampe et al., 2023) grouped by Mastcam spectral class. Sample name abbreviations are defined in Table X. Mastcam spectral classes are based on spectral features of the drill tailings and/or dump piles from each sample.

5.5. Classification of APXS DRT targets

We find that multiple classes exhibit trends with APXS elemental data. Classes J, E, and M are often distinct from other classes in their elemental abundances (Figure 20; Table 6). Classes J and E are consistent with elemental trends of the Amapari marker band. The elevated and variable metals (Zn, FeO, MnO) and lack of an MgSO4 trend in the rhythmic MB characterizes Classes J and majority of E (Thompson et al., 2023). The target classified as E that has even higher amounts of MnO, FeO, and Zn (Sol 3642 Mel) is the only APXS target on the

rippled unit of the Amapari marker bed in this dataset (Figure 20). Class M is consistent with elemental abundances of the Greenheugh pediment (e.g., elevated alkalis, MnO, and MgO; Thompson et al., 2022a&b). Class F displays similar elemental abundances to Class M but with lower total alkalis, but because only one APXS target was classified as such, we cannot draw a definitive conclusion on its elemental abundances. The slight increase in K_2O seen in spectra classified as K may be consistent with the presence of jarosite, which agrees with our interpretation of a possible Fe-sulfate contribution (see section 5.3), though could also simply be reconciled by basaltic mineralogy. Notably, the trendline for the spectra classified as C in the SO_3 vs MgO plot is close to that of $MgSO_4$ (Figure 20), which is consistent with targets in the Mirador formation in the CST. Spectra classified as C exhibit small 867-900 nm band depths with weak/flat right shoulders that appear as 1012 nm/867 nm ratios close to 1.0 which may be attributable to the flat spectrum of Mg-sulfates reducing the positive slope from 867 nm to 1012 nm characteristic of the Fe^{3+} absorption around 867-900 nm.

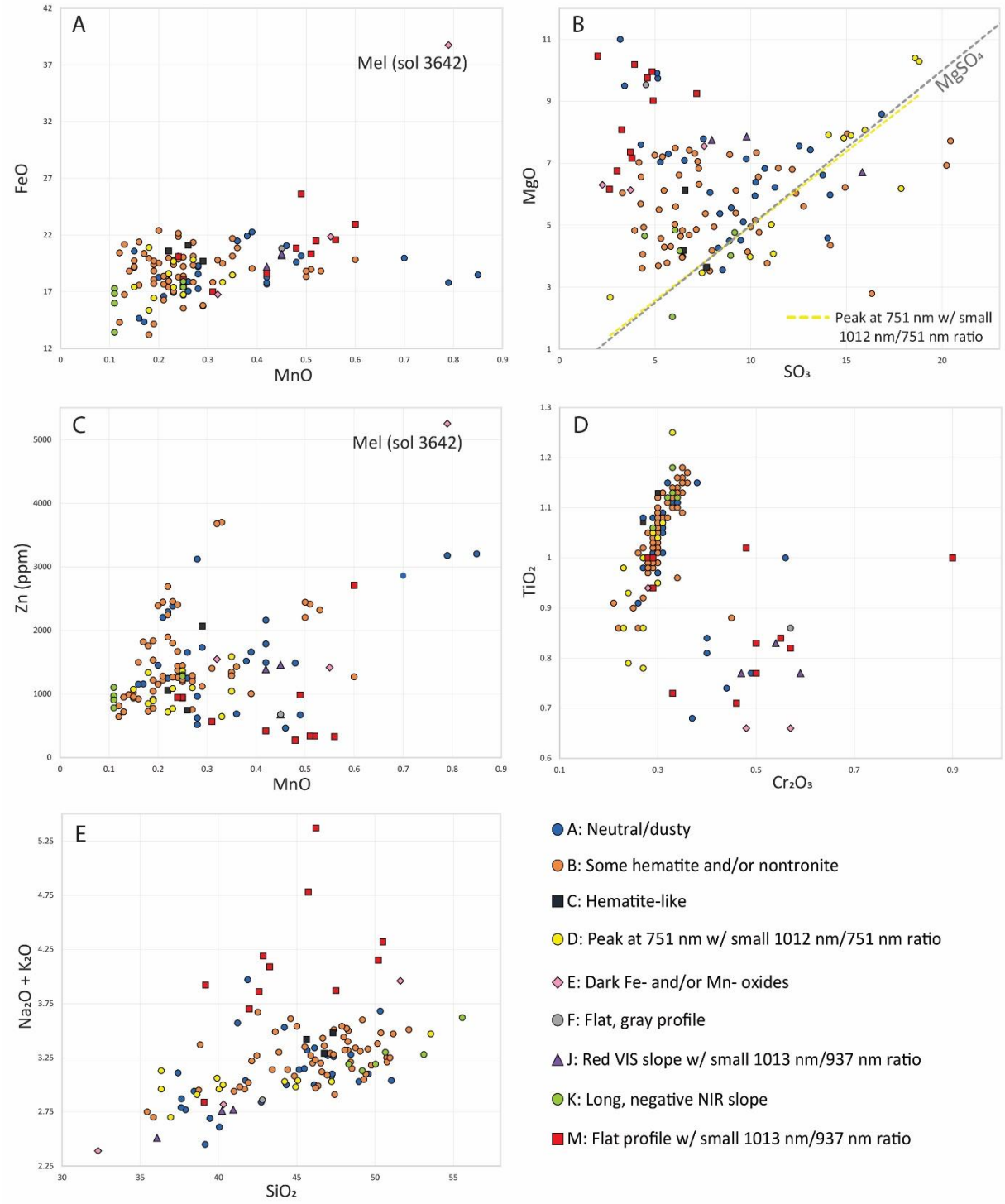

Figure 20: Comparisons of Mastcam spectral classes from DRT targets to APXS elemental compositions from Thompson et al. (2023) and Berger et al. (2023). Each APXS measurement on a DRT was color-coded by its corresponding Mastcam rock spectral class, if there was a corresponding multispectral observation acquired and the spectra of the DRT could be classified.

Table 6: APXS elemental data averaged for each class. N represents the number of spectra from APXS targets in each Mastcam rock spectral class.

	Neutral/Dusty	Some hematite and/or nontronite	Peak at 751 nm with small 1012 nm/751 nm	Hematite-like	Dark Fe- and/or Mn-oxides	Flat, gray profile	Red VIS slope with small 1013 nm/937 nm	Long, negative NIR slope	Flat profile with small 1013 nm/937 nm
N	28	56	12	3	3	1	3	6	11
Na_2O	2.38 ± 0.15	2.40 ± 0.14	2.24 ± 0.16	2.54 ± 0.16	2.44 ± 0.16	2.45 ± 0.14	2.22 ± 0.20	2.38 ± 0.14	3.00 ± 0.14
MgO	6.76 ± 0.20	5.55 ± 0.17	6.48 ± 0.20	4.65 ± 0.17	6.66 ± 0.20	9.53 ± 0.25	7.44 ± 0.22	4.08 ± 0.14	8.56 ± 0.21
Al_2O_3	8.22 ± 0.21	8.51 ± 0.20	7.74 ± 0.24	8.55 ± 0.19	7.53 ± 0.22	8.23 ± 0.19	6.60 ± 0.22	9.22 ± 0.22	8.62 ± 0.22
SiO_2	43.91 ± 0.54	46.17 ± 0.54	41.96 ± 0.53	46.57 ± 0.54	41.42 ± 0.50	42.80 ± 0.54	39.08 ± 0.50	51.15 ± 0.56	44.46 ± 0.50
P_2O_5	0.97 ± 0.07	1.01 ± 0.07	1.12 ± 0.08	1.10 ± 0.07	0.83 ± 0.06	0.73 ± 0.05	0.70 ± 0.07	1.11 ± 0.07	0.80 ± 0.06
SO_3	9.03 ± 0.18	8.25 ± 0.13	13.14 ± 0.24	6.91 ± 0.14	4.52 ± 0.12	4.53 ± 0.08	11.20 ± 0.21	6.81 ± 0.12	3.99 ± 0.08
Cl	1.44 ± 0.04	1.27 ± 0.03	1.01 ± 0.038	1.20 ± 0.04	2.15 ± 0.05	1.77 ± 0.03	2.33 ± 0.05	1.02 ± 0.03	1.23 ± 0.03
K_2O	0.73 ± 0.03	0.85 ± 0.03	0.78 ± 0.03	0.86 ± 0.03	0.61 ± 0.03	0.41 ± 0.02	0.46 ± 0.03	0.90 ± 0.04	1.10 ± 0.04
CaO	6.02 ± 0.09	5.08 ± 0.07	5.59 ± 0.09	5.18 ± 0.07	5.74 ± 0.08	6.65 ± 0.07	7.83 ± 0.09	4.98 ± 0.06	5.88 ± 0.07
TiO_2	1.00 ± 0.04	1.05 ± 0.04	0.96 ± 0.04	1.09 ± 0.04	0.75 ± 0.04	0.86 ± 0.03	0.79 ± 0.04	1.10 ± 0.05	0.88 ± 0.03
Cr_2O_3	0.34 ± 0.02	0.31 ± 0.02	0.27 ± 0.03	0.29 ± 0.02	0.44 ± 0.03	0.57 ± 0.03	0.53 ± 0.04	0.32 ± 0.02	0.47 ± 0.02
MnO	0.35 ± 0.02	0.25 ± 0.01	0.24 ± 0.02	0.26 ± 0.02	0.55 ± 0.03	0.45 ± 0.01	0.44 ± 0.03	0.16 ± 0.01	0.42 ± 0.02
FeO	18.43 ± 0.23	18.91 ± 0.23	18.09 ± 0.23	20.45 ± 0.26	25.79 ± 0.31	20.81 ± 0.26	19.91 ± 0.24	16.47 ± 0.20	20.36 ± 0.24
Ni	757.18 ± 43.21	861.45 ± 46.16	858.00 ± 48.33	830.00 ± 51.67	405.33 ± 40.00	357.00 ± 20.00	330.33 ± 35.00	936.83 ± 50.00	448.36 ± 27.27
Zn	1618.79 ± 53.39	1525.46 ± 49.38	1039.08 ± 38.33	1290.67 ± 46.67	2738.67 ± 86.67	678.00 ± 25.00	1174.00 ± 43.33	1057.00 ± 33.33	799.64 ± 27.27
Br	613.39 ± 23.39	454.23 ± 17.23	376.25 ± 17.08	571.67 ± 21.67	1196.00 ± 38.33	369.00 ± 15.00	1442.00 ± 50.00	336.33 ± 12.50	186.45 ± 9.55

5.6. ChemCam Passive Spectra

During Curiosity's traverse from Glen Torridon to first encounter with the Amapari marker band, ChemCam passive and Mastcam multispectral observations have not frequently been acquired on the same rock target. Thus, we are unable to perform comprehensive, direct comparisons of these datasets (such as the covariance analysis of Seeger (2020) from earlier in the traverse). However, we have selected a subset of measurements on like-surfaces (Figure 21) to further support the presence of new multispectral rock classes by comparing the parameters in Supplemental Table 3. Upon visual inspection, the Mastcam and ChemCam passive spectra of representative targets of new Mastcam spectral rock classes agree (Figure 21; Supplemental Table 4). For targets representative of new Mastcam multispectral rock Classes J, K, and L, the slopes from 751 nm to 805 nm are closely matched (Figure 21; Supplemental Table 5). The 751 nm to 805 nm slope for targets representative of Class M differ slightly (Figure 21; Supplemental Table 5), potentially due to a broader left shoulder corresponding to the 867 nm band depth in the ChemCam passive spectrum or viewing geometry. However, both the ChemCam passive and Mastcam multispectral observation representative of Class M do exhibit reductions in slope around 640 nm. Measurements across both instruments all show positive 527 or 535 nm band depths (Figure 21; Supplemental Table 5), though Classes J and L have more significant differences, possible due to differences in the amounts of dust between regions of interest. Overall, the agreement between the two spectral datasets give confidence that the Mastcam spectral characteristics described here are attributable to real compositional properties of the rocks (and are not significantly influenced by calibration uncertainties, viewing geometry effects, or instrumental artifacts).

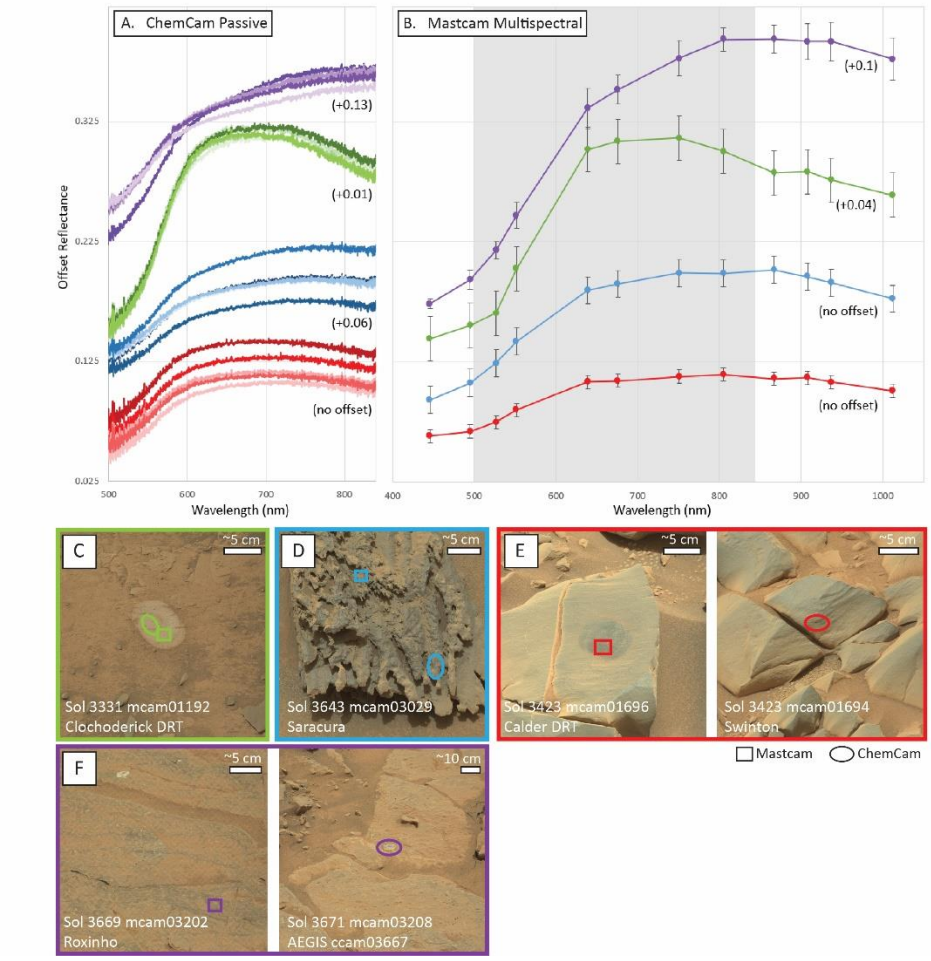

Figure 21: Comparison of (A) ChemCam passive and (B) Mastcam multispectral observations on like-surfaces. The shaded region in the Mastcam spectral plot highlights the wavelength range of the ChemCam passive spectra shown (500-850 nm). The surfaces in which ChemCam passive and Mastcam spectra were acquired are shown by colored circles and boxes, respectively. The color of the shapes corresponds with the color of the spectra. Locations of Mastcam and ChemCam spectra for (C) Class K examples; (D) Class L examples; (E) Class M examples; and (F) Class J examples.

5.7 Implications for Alteration Processes in the CST

After exploring mudstones and clay-bearing strata that reflect wetter depositional environments, Curiosity's traverse in the CST marks a transition to a drier environment with intermittently wetter periods (Rapin et al., 2023). These alternating wet-dry cycles of the CST are reflected in the large-scale, cross-bedded strata of likely aeolian origin with nodules and diagenetic features explained by the wetter periods or later interactions with groundwater (Rapin et al., 2023). Specifically, diagenetic features in the CST exhibit significant Mg-sulfate

enrichments that are likely amorphous with probable contributions of Fe-sulfates (Smith et al., 2022). We propose that these components, along with basaltic materials and small amounts of iron-oxides, can be characterized by our spectral Class K, thus enhancing our understanding of alteration processes in the CST. The following could explain our hypothesized assemblage that characterizes Class K. The oxidation of Fe- sulfides under a CO_2 atmosphere advances the alteration of silicates (e.g., dissolution of olivine) which release Ca^{2+}, Mg^{2+}, and Fe^{2+} cations that can be included in Ca-, Mg-, and Fe- sulfates (Dehouck et al., 2012; Yu et al., 2022). Additionally, the oxidation of Fe-sulfides results in fluids with low pH, which either prevented the formation of phyllosilicates or dissolved them in the CST (Bigham and Nordstrom, 2000; Bibring et al., 2006; Zolotov and Mironenko, 2007). Considering that crystalline Fe-sulfate has not been detected by CheMin and the broad SO_2 release identified in SAM-EGA data (Clark et al., 2023), an Fe-sulfate must be present in the amorphous component. Amorphous ferrous sulfates are expected to oxidize and/or crystallize rapidly under Martian conditions (Sklute et al., 2015). However, iron sulfides that had oxidized to ferrous sulfates could form Fe-hydroxy sulfates if the ferrous sulfates dehydrated rapidly before ferrous ions could undergo any oxidation that would change its valency state (Bigham and Nordstrom, 2000; Paramanick et al., 2021). Alternatively, amorphous ferric sulfates have been found to form from rapid dehydration of saturated solutions (Xu and Parise, 2012). Intermittent flowing water could have dissolved the Mg-sulfates, given their high solubility in water, and then once the sulfate-rich water table approached the surface, Mg-sulfates could have formed into nodules and cements and then become amorphous due to rapid dehydration, like the amorphous Fe-sulfates (Rapin et al., 2023; Vaniman et al., 2004). Thus, to characterize Class K, we hypothesize that a mixture of Mg- and Fe- sulfates cemented basaltic grains together as a wetter environment dried; and that the goethite and hematite components could have formed from the further aqueous alteration of Fe-sulfates (Davidson et al., 2008; Schwertmann & Murad, 1983).

5.8. Implications for Mg-sulfate detections

We recognize that CheMin has not detected Mg-sulfate and phyllosilicate in the same sample. However, orbital data suggests that both Mg-sulfate (likely in the amorphous phase) and phyllosilicates are present in Glen Torridon and up section where Curiosity is planned to explore (Sheppard et al., 2020). The abundance of phyllosilicates in GT easily masks the presence of

Mg-sulfates (this study; Sheppard et al., 2022). Although, GT is likely the most clay-rich unit Curiosity will encounter considering the rover has since traversed further up Mount Sharp into aeolian deposits and drier depositional settings. Thus, the results of our laboratory mixture experiment can be applied to Curiosity's future traverse but will likely be most applicable in assessing the purity of a potential Mg-sulfate-rich, light-toned, diagenetic feature (e.g., veins, crystals).

VI. Conclusions

It was previously hypothesized that Mastcam would be able to detect hydrated minerals, and even distinguish between mono-hydrated versus poly-hydrated Mg-sulfate phases (e.g., kieserite vs. epsomite), as Curiosity approached the sulfate-bearing strata of Mt. Sharp (Rice et al., 2022). This study provides new insight that Mastcam is sensitive to a weak hydration feature in Mg-sulfates near 1000 nm which produces a "downturn" in the R6 filter (a 1012 nm/ 937 nm slope < 1.0). Our laboratory investigation, however, shows that detecting Mg-sulfate in Mastcam multispectral data would be challenging. Specifically, 90-95 wt. % epsomite would be required to be detectable in Mastcam spectra of two-phase mixtures with phyllosilicates. Additionally, just 5 wt. % additions of basalt dampen any notable spectral features in these mixtures. Thus, any R6 downturns present in Mastcam multispectral data from the sulfate-bearing unit that Curiosity continues to explore can more easily be attributed to other minerals. In fact, we find that the Mastcam spectra from confirmed Mg-sulfate-bearing strata consistently do not exhibit a R6 downturn or other spectral features uniquely attributable to sulfates. The results of our laboratory investigation confirm our hypothesis that it would take small amounts of phyllosilicates and/or basalt to completely mask the R6 downturn in Mastcam spectra.

We continued the compilation of a comprehensive database for Mastcam spectra since the work of Rice et al. (2022) and their analysis through Vera Rubin ridge (sols 0-2302). We analyzed observations from Glen Torridon, Greenheugh Pediment, the clay-sulfate transition (CST), Marker Band valley, and Curiosity's first encounter of the Amapari marker band (sols 2303-3672). Through an investigation of spectral trends and variability with stratigraphy, we find that the CST region exhibits more multispectral rock variability than the phyllosilicate-rich region, Glen Torridon, due to a higher abundance of iron-oxides and lower abundance of phyllosilicates. We also identify four new rock spectral classes that are unique to this part of the

traverse. Two of these new classes, Classes J and L, are associated with the Amapari marker band, and their spectral characteristics are attributable to Ca-pyroxenes in the bedrock and to dust coatings on the rippled and rhythmically laminated units. Another new spectral class, Class M, is associated with the Greenheugh Pediment and is consistent with relatively unaltered basalt with magnetite. The new rock class, Class K, inherent to the CST and Marker Band Valley (MBV) indicates a strong diagenetic overprint spanning these regions. The occurrence of this class is consistent with the hypothesis of alternating wet-dry environments in the CST producing sulfate-rich nodules due to evaporation where the sulfate-rich water table approaches the surface (Rapin et al., 2023). These new spectral classes, in addition to those identified in previous traverse regions (Rice et al., 2022), will provide a baseline for Curiosity's ongoing investigation of Mount Sharp and also for Perseverance's exploration of Jezero crater, another Noachian-aged lake system.

References

Banham, S. G., Gupta, S., Rubin, D. M., Bedford, C. C., Edgar, L. A., Bryk, A. B., et al. (2022). Evidence for Fluctuating Wind in Shaping an Ancient Martian Dune Field: The Stimson Formation at the Greenheugh Pediment, Gale Crater. *Journal of Geophysical Research: Planets*, *127*(9), e2021JE007023. https://doi.org/10.1029/2021JE007023

Bell, J. F., Malin, M. C., Caplinger, M. A., Ravine, M. A., Godber, A. S., Jungers, M. C., & Rice, M. S. (2012). Mastcam Multispectral Imaging on the Mars Science Laboratory Rover: Wavelength Coverage and Imaging Strategies at the Gale Crater Field Site. *43rd Lunar and Planetary Science Conference.*

Bell, J. F. III, Godber, A., McNair, S., Caplinger, M. A., Maki, J. N., Lemmon, M. T., et al. (2017). The Mars Science Laboratory Curiosity rover Mastcam instruments: Preflight and in-flight calibration, validation, and data archiving. *Earth and Space Science*, *4*(7), 396–452. https://doi.org/10.1002/2016EA000219

Bennett, K. A., Fox, V. K., Bryk, A., Dietrich, W., Fedo, C., Edgar, L., et al. (2023). The Curiosity Rover's Exploration of Glen Torridon, Gale Crater, Mars: An Overview of the Campaign and Scientific Results. *Journal of Geophysical Research. Planets*, *128*(1), e2022JE007185. https://doi.org/10.1029/2022JE007185

Berger, J. A., Gellert, R., McCraig, M. A., O'Connell-Cooper, C. D., Spray, J. G., Thompson, L. M., et al. (2023). Isochemical characteristics of the clay-sulfate transition in Gale crater, Mars: APXS results from Mont Mercou to the Marker Band valley. *54th Lunar and Planetary Science Conference. 2806.*

Bibring, J.-P., Langevin, Y., Mustard, J. F., Poulet, F., Arvidson, R., Gendrin, A., et al. (2006). Global Mineralogical and Aqueous Mars History Derived from OMEGA/Mars Express Data. *Science*, *312*(5772), 400–404. https://doi.org/10.1126/science.1122659

Bigham, J. M., & Nordstrom, D. K. (2000). Iron and aluminum hydroxysulfates from acid sulfate waters. In *Reviews in Mineralogy and Geochemistry* (Vol. 40, p. 351403). https://doi.org/10.2138/rmg.2000.40.7

Bishop, J., Bell III, J., & Moersch, J. (Eds.). (2019). Remote Compositional Analysis: Techniques for Understanding Spectroscopy, Mineralogy, and Geochemistry of Planetary Surfaces (Cambridge Planetary Science). Cambridge: Cambridge University Press. doi:10.1017/9781316888872

Bishop, J. L., Yeşilbaş, M., Talla, D., Hiroi, T., (2021). Spectral properties of Fe hydroxy sulfates and implications for Mars. *52nd Lunar and Planetary Science Conference. 2548.*

Blake, D., Vaniman, D., Achilles, C., Anderson, R., Bish, D., Bristow, T., et al. (2012). Characterization and calibration of the CheMin mineralogical instrument on Mars Science Laboratory. *Space Sci. Rev.* 170(1-4), 341-399. https://doi.org/10.1007/s11214-012-9905-1

Bridges, J. C., Schwenzer, S. P., Leveille, R., Westall, F., Wiens, R. C., Mangold, N., et al. (2015). Diagenesis and clay mineral formation at Gale Crater, Mars. *Journal of Geophysical Research: Planets*, *120*(1), 1–19. https://doi.org/10.1002/2014JE004757

Bristow, T. F., Kennedy, M. J., Derkowski, A., Droser, M. L., Jiang, G., & Creaser, R. A. (2009). Mineralogical constraints on the paleoenvironments of the Ediacaran Doushantuo

Formation. *Proceedings of the National Academy of Sciences of the United States of America*, *106*(32), 13190–13195. https://doi.org/10.1073/pnas.0901080106

Bristow, T., & Milliken, R. (2011). A terrestrial perspective on authigenic clay production in ancient Martian lakes. *Clays and Clay Minerals*, *59*, 339–358. https://doi.org/10.1346/CCMN.2011.0590401

Bristow, T. F., Rampe, E. B., Achilles, C. N., Blake, D. F., Chipera, S. J., Craig, P., et al. (2018). Clay mineral diversity and abundance in sedimentary rocks of Gale crater, Mars. *Science Advances*, *4*(6), eaar3330. https://doi.org/10.1126/sciadv.aar3330

Broz, A. P. (2020). Organic Matter Preservation in Ancient Soils of Earth and Mars. *Life (Basel, Switzerland)*, *10*(7), 113. https://doi.org/10.3390/life10070113

Burns, R. (1993). Mineralogical Applications of Crystal Field Theory (2nd ed., Cambridge Topics in Mineral Physics and Chemistry). *Cambridge: Cambridge University Press*. doi:10.1017/CBO9780511524899

Buz, J., Ehlmann, B. L., Pan, L., & Grotzinger, J. P. (2017). Mineralogy and stratigraphy of the Gale crater rim, wall, and floor units. *Journal of Geophysical Research: Planets*, *122*(5), 1090–1118. https://doi.org/10.1002/2016JE005163

Campbell, J. L., Perrett, G. M., Gellert, R., Andrushenko, S. M., Boyd, N. I., Maxwell, J. A., et al. (2012). Calibration of the Mars Science Laboratory alpha particle X-ray spectrometer. *Space Science Reviews, 170, 319– 340*. doi.org/10.1007/s11214-012-9873-5

Campbell, J. L., King, P. L., Burkemper, L., Berger, J. A., Gellert, R., Boyd, N. I., et al. (2014). The Mars Science Laboratory APXS calibration target: Comparison of Martian measurements with the terrestrial calibration. *Nuclear Instruments and Methods in Physics Research Section B: Beam Interactions with Materials and Atoms,* 323, 49– 58. doi.org/10.1016/j.nimb.2014.01.011

Cardenas, B. T., Grotzinger, J. P., Lamb, M. P., Lewis, K. W., Fedo, C. M., Bryk, A. B., et al. (2023). Barform deposits of the Carolyn Shoemaker formation, Gale crater, Mars. *Journal of Sedimentary Research*, *92*(12), 1071–1092. https://doi.org/10.2110/jsr.2022.032

Carter, J., Loizeau, D., Mangold, N., Poulet, F., & Bibring, J.-P. (2015). Widespread surface weathering on early Mars: A case for a warmer and wetter climate. *Icarus*, *248*, 373–382. https://doi.org/10.1016/j.icarus.2014.11.011

Chipera, S.J., Bish, D.L., 2002. FULLPAT: a full-pattern quantitative analysis program for X-ray powder diffraction using measured and calculated patterns. *J. Appl. Crystallogr. 35*(6), 744-749.

Clark, J. V., Sutter, B., Lewis, J., McAdam, A. C., Archer, P. D., Franz, H., et al. (2023). Mineralogical and chemical changes in the clay-sulfate transition region as detected by the Sample Analysis at Mars-Evolved Gas Analyzer (SAM-EGA) in Gale crater, Mars. *54th Lunar and Planetary Science Conference, 2806.*

Clouits, E. A., Bell, J. F., Mueller, T., (2000). Pyroxene + Palagonite Mixture Spectra: Effects of Palagonite on Deriving Pyroxene Compositional Information. *31st Lunar and Planetary Science Conference, 1114.*

Cloutis, E. A., Craig, M. A., Mustard, J. F., Kruzelecky, R. V., Jamroz, W. R., Scott, A., et al. (2007). Stability of hydrated minerals on Mars. *Geophysical Research Letters*, *34*(20). https://doi.org/10.1029/2007GL031267

Cloutis, E., Hawthorne, F., Mertzman, S., Krenn, K., Craig, M., Marcino, D., et al. (2006). Detection and discrimination of sulfate minerals using reflectance spectroscopy. *Icarus*, *184*(1), 121–157. https://doi.org/10.1016/j.icarus.2006.04.003

Curtis, S. (2022) Spectral Variability in Naturally Weathered Rock Surfaces and Implications for Mars (Unpublished master's dissertation). *WWU Graduate School Collection*. 1118. https://cedar.wwu.edu/wwuet/1118

Das, D., S. M. R. Turner, S. M. R., Gasda, P. J., Schwenzer, S. P., Palandri, J., Reed, M. H., et al. (2023). Simulating evaporative wet and dry cycles in Gale crater, Mars using modeling techniques. *54th Lunar and Planetary Science Conference. 2806.*

Davidson, L. E., Shaw, S., & Benning, L. G. (2008). The kinetics and mechanisms of schwertmannite transformation to goethite and hematite under alkaline conditions. *American Mineralogist*, *93*(8–9), 1326–1337. https://doi.org/10.2138/am.2008.2761

Day, M., Anderson, W., Kocurek, G., & Mohrig, D. (2016). Carving intracrater layered deposits with wind on Mars. *Geophysical Research Letters*, *43*(6), 2473–2479. Et https://doi.org/10.1002/2016GL068011

Dehouck, E., Cousin, A., Mangold, N., Frydenvang, J., Gasnault, O., Forni, O., et al. (2022). Bedrock Geochemistry and Alteration History of the Clay-Bearing Glen Torridon Region of Gale Crater, Mars. *Journal of Geophysical Research: Planets*, *127*(12), e2021JE007103. https://doi.org/10.1029/2021JE007103

Dixon, D. (2018). Visible-to-Near-Infrared Spectral Variability of Hydrated Sulfates and Candidate Mars Landing Sites: Implications for the Mastcam-Z Investigation on NASA's Mars-2020 Rover Mission" (Unpublished master's dissertation). *WWU Graduate School Collection*. 638. https://cedar.wwu.edu/wwuet/638

Douglas, S. (2004). Microbial biosignatures in evaporite deposits: Evidence from Death Valley, California, *Planetary and Space Science*, *52*(1,Äì3), 223-227. doi: 10.1016/j.pss.2003.08.005

Milliken, R. E., Grotzinger, J. P., & Thomson, B. J. (2010). Paleoclimate of Mars as captured by the stratigraphic record in Gale Crater. *Geophysical Research Letters*, *37*(4). https://doi.org/10.1029/2009GL041870

Farrand, W. H., Bell III, J. F., Johnson, J. R., Jolliff, B. L., Knoll, A. H., McLennan, S. M., et al. (2007). Visible and near-infrared multispectral analysis of rocks at Meridiani Planum, Mars, by the Mars Exploration Rover Opportunity. *Journal of Geophysical Research: Planets*, *112*(E6). https://doi.org/10.1029/2006JE002773

Farrand, W. H., Bell, J. F., III, Johnson, J. R., Arvidson, R. E., Crumpler, L. S., Hurowitz, J. A., & Schröder, C. (2008). Rock spectral classes observed by the Spirit rover's Pancam on the Gusev crater plains and in the Columbia Hills. *Journal of Geophysical Research: Planets*, 113(E12), E12S38. https://doi.org/10.1029/2008JE003237

Farrand, W. H., Bell III, J. F., Johnson, J. R., Rice, M. S., Jolliff, B. L., & Arvidson, R. E. (2014). Observations of rock spectral classes by the Opportunity rover's Pancam on northern Cape York and on Matijevic Hill, Endeavour Crater, Mars. *Journal of*

Geophysical Research: Planets, *119*(11), 2349–2369. https://doi.org/10.1002/2014JE004641

Fraeman, A. A., Ehlmann, B. L., Arvidson, R. E., Edwards, C. S., Grotzinger, J. P., Milliken, R. E., Quinn, D. P., & Rice, M. S. (2016). The stratigraphy and evolution of lower Mount Sharp from spectral, morphological, and thermophysical orbital data sets. *Journal of Geophysical Research: Planets*, *121*(9), 1713–1736. https://doi.org/10.1002/2016JE005095

Fraeman, A. A., Johnson, J. R., Arvidson, R. E., Rice, M. S., Wellington, D. F., Morris, R. V., et al. (2020). Synergistic Ground and Orbital Observations of Iron Oxides on Mount Sharp and Vera Rubin Ridge. *Journal of Geophysical Research: Planets*, *125*(9), [e2019JE006294]. https://doi.org/10.1029/2019JE006294

Gasda, P. J., Comellas, J., Essunfeld, A., Das, D., Bryk, A. B., Dehouck, E., et al. (2022). Overview of the Morphology and Chemistry of Diagenetic Features in the Clay-Rich Glen Torridon Unit of Gale Crater, Mars. *Journal of Geophysical Research: Planets*, *127*(12), e2021JE007097. https://doi.org/10.1029/2021JE007097

P. J. Gasda, N. Lanza, W. Rapin, J. Frydenvang, W. Goetz, et al. (2023). ChemCam bservations of the Marker Band, Gale crater, Mars. *54th Lunar and Planetary Science Conference, 2389.*

Gellert, R., Rieder, R., Brückner, J., Clark, B.C., Dreibus, G., Klingelhöfer, G., et al. (2006). Alpha Particle X-Ray Spectrometer (APXS): Results from Gusev crater and calibration report. Journal of Geophysical. *Research, Planets, 111*, E02S05. doi.org/10.1029/2005JE002555

Gellert, R., Clark, B.C. III, & Mars Science Laboratory (MSL) Science Team (2015). In situ compositional measurements of rocks and soils with the Alpha Particle X-ray Spectrometer on NASA's Mars rovers. *Elements 11*, 39–44. https://doi.org/10.2113/gselements.11.1.39

Golombek, M., Grant, J., Kipp, D., Vasavada, A., Kirk, R., Fergason, R., et al. (2012). Selection of the Mars Science Laboratory Landing Site. *Space Science Reviews*, *170*, 641–737. https://doi.org/10.1007/s11214-012-9916-y

Grotzinger, J. P. et al., (2015). Deposition, exhumation, and paleoclimate of an ancient lake deposit, Gale crater, Mars. *Science* 350, aac7575. doi:10.1126/science.aac7575

Lane, M. D., Morris, R. V., Mertzman, S. A., & Christensen, P. R. (2002). Evidence for platy hematite grains in Sinus Meridiani, Mars. *Journal of Geophysical Research: Planets*, *107*(E12), 9-1-9–15. https://doi.org/10.1029/2001JE001832

Hapke, B., (1993). Theory of Reflectance and Emittance Spectroscopy. *Cambridge University Press, NY, NY.*

Gupta, S., Dietrich, W. E., Lewis, K. W., Kite, E., Mondro, C. A., Schieber, J., et al. (2023). "High" but not so dry on Aeolis Mons*:* Transient Lake Systems in Hesperian Deserts in Gale crater. *54th Lunar and Planetary Science Conference. 2806.*

Haber, J. T., Horgan, B., Fraeman, A. A., Johnson, J. R., Bell III, J. F., Rice, M. S., et al. (2022). Mineralogy of a Possible Ancient Lakeshore in the Sutton Island Member of Mt. Sharp, Gale Crater, Mars, From Mastcam Multispectral Images. *Journal of Geophysical Research: Planets*, *127*(10), e2022JE007357. https://doi.org/10.1029/2022JE007357

Harris, J. K., & M. Grindrod, P. (2018). Hapke mixture modeling applied to VNIR spectra of mafic mineral mixtures and shergottites: Implications for quantitative analysis of satellite data. *Meteoritics & Planetary Science*, *53*(6), 1179–1206. https://doi.org/10.1111/maps.13065

Hoza, K. (2019). Photometric investigations of weathering rinds and coatings with implications for Mars. (Unpublished master's dissertation). *WWU Graduate School Collection*. 921. https://cedar.wwu.edu/wwuet/921

Horgan, B. H. N., Johnson, J. R., Fraeman, A. A., Rice, M. S., Seeger, C., Bell, J. F., et al. (2020). Diagenesis of Vera Rubin Ridge, Gale Crater, Mars, From Mastcam Multispectral Images. *Journal of Geophysical Research. Planets*, *125*(11), e2019JE006322. https://doi.org/10.1029/2019JE006322

Jacob, S. R. (2022). Deciphering the Geologic History and Mineralogy of Planets from Mars to Exoplanets Using Rover In Situ Analysis, Laboratory Spectroscopy, and Modeling [Doctoral dissertation, Arizona State University].

Johnson, J.R., J.F. Bell III, S. Bender, D. Blaney, E. Cloutis, L. DeFlores, et al. (2015). MSL Science Team, ChemCam Passive Reflectance Spectroscopy of Surface Materials at the Curiosity Landing Site, Mars. *Icarus, 249*, 74–92.

Johnson, J. R., Grundy, W. M., Lemmon, M. T., Liang, W., Bell, J. F., Hayes, A. G., & Deen, R. G. (2021). Spectrophotometric properties of materials observed by Pancam on the Mars Exploration Rovers: 4. Final mission observations. *Icarus*, *357*, 114261. https://doi.org/10.1016/j.icarus.2020.114261

Kling, A. M., Haberle, R. M., McKay, C. P., Bristow, T. F., & Rivera-Hernández, F. (2020). Subsistence of ice-covered lakes during the Hesperian at Gale crater, Mars. *Icarus*, *338*, 113495. https://doi.org/10.1016/j.icarus.2019.113495

Kotler, J. M. (2009). Biosignature storage in sulfate minerals- synthetic and natural investigations of the jarosite group minerals. Graduate Student Theses, Dissertations, & Professional Papers. 1275. https://scholarworks.umt.edu/etd/1275

Kraft, M. D., Christensen, P. R., (2013). Tectonic formation of Mount Sharp, Gale crater, Mars. *44th Lunar and Planetary Science, 3106.*

Lapo, K. (2021) "Martian Spectroscopy: Laboratory calibration of the Perseverance rover's Mastcam-Z and photometric investigation of Mars-analog ferric-coated sand" (Unpublished master's dissertation). *WWU Graduate School Collection*. 1011. https://cedar.wwu.edu/wwuet/1011

Lewis, K. W., Kite, E. S., Weitz, C. M., Cowart, A., Dietrich, W. E., Gupta, S., et al. (2023). Rhythmic stratigraphy at the orbital marker bed at Mount Sharp, Gale crater, Mars. *54th Lunar and Planetary Science Conference 2806.*

Lynch, K. L., Horgan, B. H., Munakata-Marr, J., Hanley, J., Schneider, R. J., et al. (2015). Near-infrared spectroscopy of lacustrine sediments in the Great Salt Lake Desert: An analog study for Martian paleolake basins. *Journal of Geophysical Research: Planets*, *120*(3), 599–623. https://doi.org/10.1002/2014JE004707

Malin, M. C., Ravine, M. A., Caplinger, M. A., Tony Ghaemi, F., Schaffner, J. A., Maki, J. N., et al. (2017). The Mars Science Laboratory (MSL) Mast cameras and Descent imager:

Investigation and instrument descriptions. *Earth and Space Science*, *4*(8), 506–539. https://doi.org/10.1002/2016EA000252

Maurice, S., Wiens, R., Saccoccio, M., Barraclough, B., Gasnault, O., Forni, O., et al. (2012). The ChemCam Instrument Suite on the Mars Science Laboratory (MSL) Rover: Science Objectives and Mast Unit Description. *Space Science Reviews*, *170*. https://doi.org/10.1007/s11214-012-9912-2

Michalski, J. R., Kraft, M. D., Sharp, T., & Christensen, P. (2006). Effects of chemical weathering on infrared spectra of Columbia River Basalt and spectral interpretations of martian alteration. *Earth and Planetary Science Letters*, *248*(3–4), 822–829. https://doi.org/10.1016/j.epsl.2006.06.034

Minitti et al., (2021). Rock Textures and Grain Sizes in the Glen Torridon Region (Gale Crater, Mars) Observed by the Mars Hand Lens Imager (MAHLI) and ChemCam, *52nd Lunar and Planetary Science Conference*, no. 2435.

Moreras-Marti, A., Fox-Powell, M., Cousins, C. R., Macey, M. C., & Zerkle, A. L. (2022). Sulfur isotopes as biosignatures for Mars and Europa exploration. *Journal of the Geological Society*, *179*(6), jgs2021-134. https://doi.org/10.1144/jgs2021-134

Murchie, S. L., Mustard, J. F., Ehlmann, B. L., Milliken, R. E., Bishop, J. L., McKeown, N. K., et al. (2009). A synthesis of Martian aqueous mineralogy after 1 Mars year of observations from the Mars Reconnaissance Orbiter. *Journal of Geophysical Research: Planets*, *114*(E2). https://doi.org/10.1029/2009JE003342

Niles, P. B., & Michalski, J. (2012). Origin and Evolution of Sediments in Gale Crater Through Ice-Hosted Processes. *Lunar and Planetary Science Conference* 2012 no. 2575.

Currey, D. R. (1990), Quaternary palaeolakes in the evolution of semidesert basins, with special emphasis on Lake Bonneville and the Great Basin, U.S.A. *Paleogeography, Palaeoclimatology, Paleoecology*, *76*(3-4), 189-214. doi: 10.1016/0031-0182(90)90113-l

Paramanick, S., Rajesh, V. J., Praveen, M. N., Sajinkumar, K. S., & Bhattacharya, S. (2021). Spectral and Chemical Characterization of Copiapite and Rozenite from Padinjarathara in Wayanad, Southern India: Implications for Mars Exploration. *Chemical Geology*, *575*, 120043. https://doi.org/10.1016/j.chemgeo.2020.120043

Pedgregosa, F., Varoquax, G., Gramfort, A., Michel, V., & Thirion, B. (2011). Scikit-learn: Machine learning in Python. *Journal of Machine Learning Research*, 12, 2825– 2830.

Rampe, E. B., Bristow, T. F., Blake, D. F., Chipera, S. J., Vaniman, D. T., Achilles, C. N., et al. (2023). Mineralogical evidence for environmental change in the clay-sulfate transition at Gale crater, Mars. *54th Lunar and Planetary Science Conference*, 1554.

Rapin, W., Ehlmann, B. L., Dromart, G., Schieber, J., Thomas, N. H., Fischer, W. W., et al. (2019). An interval of high salinity in ancient Gale crater lake on Mars. *Nature Geoscience*, *12*(11), Article 11. https://doi.org/10.1038/s41561-019-0458-8

Rapin, W., Dromart, G., Rubin, D., Deit, L. L., Mangold, N., Edgar, L. A., et al. (2021). Alternating wet and dry depositional environments recorded in the stratigraphy of Mount Sharp at Gale crater, Mars. *Geology*, *49*(7), 842–846. https://doi.org/10.1130/G48519.1

Rapin, W., Dromart, G., Schieber, J., Clark, B. C., Kah, L., Rubin, D., et al. (2023). Not always wet: An aridification sequence in the orbital clay-sulfate transition of Aeolis Mons. *54th Lunar and Planetary Science Conference*, 2806.

Rice, M. S., Bell, J. F., Cloutis, E. A., Wang, A., Ruff, S. W., Craig, M. A., et al. (2010). Silica-rich deposits and hydrated minerals at Gusev Crater, Mars: Vis-NIR spectral characterization and regional mapping. *Icarus*, *205*(2), 375–395. https://doi.org/10.1016/j.icarus.2009.03.035

Rice, M. S. et al., (2013). Reflectance spectra diversity of silica-rich materials: Sensitivity to environment and implications for detections on Mars. *Icarus*, *223*(1), 499–533.

Rice, M. S., Seeger, C., Bell, J., Calef, F., St. Clair, M., Eng, A., et al. (2022). Spectral Diversity of Rocks and Soils in Mastcam Observations Along the Curiosity Rover's Traverse in Gale Crater, Mars. *Journal of Geophysical Research: Planets*, *127*(8), e2021JE007134. https://doi.org/10.1029/2021JE007134

Rice, M. S. (2022). Mastcam multispectral database from the Curiosity rover's traverse in Gale crater, Mars (sols 0-2302*)* (Vol. 104). WWU Geology Faculty Publications. https://doi.org/10.25710/rqr0-8x75

Rice, M. S., Johnson, J. R., Million, C. C., St. Clair, M., Horgan, B. N., Vaughan, et al. (2023). Spectral variability of rocks and soils on the Jezero crater floor: A summary of multispectral observations from Perseverance's Mastcam-Z instrument. *Journal of Geophysical Research: Planets*, *n/a*(n/a), e2022JE007548. https://doi.org/10.1029/2022JE007548

Rieder, R., Gellert, R., Brückner, J., Klingelhöfer, G., Dreibus, G., Yen, A. & Squyres, S. W. (2003) The new Athena alpha particle X-ray spectrometer for the Mars Exploration Rovers. *Journal of Geophysical Research, Planets*, *108*, E12, 8066. https://doi.org/10.1002/2015GL066675

Rietveld, H., (1969). A profile refinement method for nuclear and magnetic structures. *J. Appl. Crystallogr.* *2*(2), 65-71.

Rivera-Hernández, F., Sumner, D. Y., Mangold, N., Banham, S. G., Edgett, K. S., Fedo, C. M., et al. (2020). Grain Size Variations in the Murray Formation: Stratigraphic Evidence for Changing Depositional Environments in Gale Crater, Mars. *Journal of Geophysical Research: Planets*, *125*(2), e2019JE006230. https://doi.org/10.1029/2019JE006230

Roberts, A. L., Gupta, S., Dietrich, W. E., Edgar, L. A., Rapin, W., Banham, S. G., et al. (2023). What depositional processes and paleoenvironments formed the layered sulfate unit in Gale crater, Mars?: Insights from Marker Band valley. *54th Lunar and Planetary Science Conference*, 2806.

Roush, T. L., Bishop, J. L., Brown, A. J., Blake, D. F., & Bristow, T. F. (2015). Laboratory reflectance spectra of clay minerals mixed with Mars analog materials: Toward enabling quantitative clay abundances from Mars spectra. *Icarus*, *258*, 454–466. https://doi.org/10.1016/j.icarus.2015.06.035

Rudolph, A., Horgan, B., Johnson, J., Bennett, K., Haber, J., Bell, J. F., et al. (2022). The Distribution of Clay Minerals and Their Impact on Diagenesis in Glen Torridon, Gale Crater, Mars. *Journal of Geophysical Research: Planets*, *127*(10). https://doi.org/10.1029/2021JE007098

Schwertmann, U., & Murad, E. (1983). Effect of pH on the Formation of Goethite and Hematite from Ferrihydrite. *Clays and Clay Minerals*, *31*(4), 277–284. https://doi.org/10.1346/CCMN.1983.0310405

Seeger, C. (2020). Using Multispectral Imagery to Interrogate Deposition, Alteration, and Weathering Across Curiosity Rover's Traverse in Gale Crater, Mars (Unpublished master's dissertation). *WWU Graduate School Collection*. 974. https://cedar.wwu.edu/wwuet/974

Seeger, C. H., Grotzinger, J. P., & Cowart, A. C. (2023). Diagenetic overprints associated with the clay-sulfate transition in Gale crater, Mars. *54th Lunar and Planetary Science Conference*, 2806.

Sheppard, R. Y., Milliken, R. E., Parente, M., & Itoh, Y. (2021). Updated Perspectives and Hypotheses on the Mineralogy of Lower Mt. Sharp, Mars, as Seen from Orbit. *Journal of Geophysical Research: Planets*, *126*(2), e2020JE006372. https://doi.org/10.1029/2020JE006372

Sheppard, R. Y., Thorpe, M. T., Fraeman, A. A., Fox, V. K., & Milliken, R. E. (2021). Merging Perspectives on Secondary Minerals on Mars: A Review of Ancient Water-Rock Interactions in Gale Crater Inferred from Orbital and In-Situ Observations. *Minerals*, *11*(9), Article 9. https://doi.org/10.3390/min11090986

Sheppard, R. Y., Milliken, R. E., & Robertson, K. M. (2022). Presence of clay minerals can obscure spectral evidence of Mg sulfates: Implications for orbital observations of Mars. *Icarus*, *383*, 115083. https://doi.org/10.1016/j.icarus.2022.115083

Shkuratov, Y., L. Starukhina, H. Hoffmann, G. Arnold (1999). A Model of Spectral Albedo of Particulate Surfaces: Implications for Optical Properties of the Moon. *Icarus, 137*(2), 235–246. http://doi.org/10.1006/icar.1998.6035

Simpson, S. L., Achilles, C. N., Rampe, E. B., Bristow, T. F., Blake, D. F., Chipera, S. J., et al. (2023) The composition of X-ray amorphous materials in Gale crater, Mars. *54th Lunar and Planetary Science Conference*, 2781.

Sklute, E. C., Jensen, H. B., Rogers, A. D., and Reeder, R. J. (2015), Morphological, structural, and spectral characteristics of amorphous iron sulfates. *J. Geophys. Res. Planets*, 120, 809– 830, doi: 10.1002/2014JE004784.

Smith, R. J., McLennan, S. M., Achilles, C. N., Dehouck, E., Horgan, B. H. N., Mangold, N., et al. (2021). X-ray amorphous components in sedimentary rocks of Gale crater, Mars: Evidence for ancient formation and long-lived aqueous activity. *Journal of Geophysical Research: Planets*, 126(3), e2020JE006782. https://doi.org/10.1029/2020JE006782

Smith, R. J., McLennan, S. M., Sutter, B., Rampe, E. B., Dehouck, E., Siebach, K. L., et al. (2022). X-Ray Amorphous Sulfur-Bearing Phases in Sedimentary Rocks of Gale Crater, Mars. *Journal of Geophysical Research: Planets*, *127*(5), e2021JE007128. https://doi.org/10.1029/2021JE007128

Stack, K. M., & Milliken, R. E. (2015). Modeling near-infrared reflectance spectra of clay and sulfate mixtures and implications for Mars. *Icarus*, *250*, 332–356. https://doi.org/10.1016/j.icarus.2014.12.009

Thompson, L. M., Spray, J. G., O'Connell-Cooper, C., Berger, J. A., Yen, A., Gellert, R., et al. (2022a). Alteration at the Base of the Siccar Point Unconformity and Further Evidence for an Alkaline Provenance at Gale Crater: Exploration of the Mount Sharp Group, Greenheugh Pediment Cap Rock Contact With APXS. *Journal of Geophysical Research: Planets*, *127*(11), e2021JE007178. https://doi.org/10.1029/2021JE007178

Thompson, L., Spray, J., Gellert, R., Williams, R., Berger, J., O'Connell-Cooper, C., et al. (2022b). APXS-determined compositional diversity of eolian Siccar Point group sandstones, Gale crater Mars: Implications for provenance and timing of events. *EPSC2022*-1184. https://doi.org/10.5194/epsc2022-1184

Thompson, L. M., Kite, E. S., Grotzinger, J. P., Yen, A. S., Berger, J. A., Lewis, K. W., et al. (2023). Investigation of the Gale crater Marker Band (and beyond) with the Mars Science Laboratory, Alpha Particle X-ray Spectrometer. *54th Lunar and Planetary Science Conference*, 2806.

Thomson, B. J., Buczkowski, D. L., Crumpler, L. S., Seelos, K. D., & Fassett, C. I. (2019). How Much of the Sediment in Gale Crater's Central Mound Was Fluvially Transported? *Geophysical Research Letters*, *46*(10), 5092–5099. https://doi.org/10.1029/2018GL081727

Thorpe, M. T., Bristow, T. F., Rampe, E. B., Tosca, N. J., Grotzinger, J. P., Bennett, K. A., et al. (2022). Mars Science Laboratory CheMin data from the Glen Torridon region and the significance of lake-groundwater interactions in interpreting mineralogy and sedimentary history. *Journal of Geophysical Research: Planets*, 127, e2021JE007099. https://doi.org/10.1029/2021JE007099

Turenne, N., Sidhu, S., Applin, D. M., Cloutis, E. A., Wolf, Z. U., Mertzman, S. A., et al. (2023). Spectral reflectance properties of nontronite exposed to Mars-like surface conditions and low-temperature heating (<300 °C). *Icarus*, *395*, 115448. https://doi.org/10.1016/j.icarus.2023.115448

Vaniman, D. T., Bish, D. L., Chipera, S. J., Fialips, C. I., William Carey, J., & Feldman, W. C. (2004). Magnesium sulphate salts and the history of water on Mars. *Nature*, *431*(7009), 663–665. https://doi.org/10.1038/nature02973

Vasavada, A. R. (2022). Mission Overview and Scientific Contributions from the Mars Science Laboratory Curiosity Rover After Eight Years of Surface Operations. *Space Science Reviews*, *218*(3), 14. https://doi.org/10.1007/s11214-022-00882-7

Wang, A., Freeman, J. J., & Jolliff, B. L. (2009). Phase transition pathways of the hydrates of magnesium sulfate in the temperature range 50°C to 5°C: Implication for sulfates on Mars. *Journal of Geophysical Research*, *114*(E4), E04010. https://doi.org/10.1029/2008JE003266

Wang, A., Jolliff, B. L., Liu, Y., & Connor, K. (2016). Setting constraints on the nature and origin of the two major hydrous sulfates on Mars: Monohydrated and polyhydrated sulfates. *Journal of Geophysical Research: Planets*, *121*(4), 678–694. https://doi.org/10.1002/2015JE004889

Watkins, J. A., Grotzinger, J. P., Stein, N. T., Banham, S. G., Gupta, S., Rubin, D. M., et al. (2022). Burial and exhumation of sedimentary rocks revealed by the base Stimson erosional unconformity, Gale crater, Mars. *Journal of Geophysical Research: Planets*, *127*(7), e2022JE007293. https://doi.org/10.1029/2022je007293

Weitz, C. M., Lewis, K. W., Bishop, J. L., Thomson, B. J., Arvidson, R. E., et al. (2022). Orbital Observations of a Marker Horizon at Gale Crater. *Journal of Geophysical Research: Planets*, *127*(4), e2022JE007211. https://doi.org/10.1029/2022JE007211

Weitz, C. M., Lewis, K. W., Kite, E. S., Dietrich, W. E., Thompson, L. M., O'Connell, C. D., et al. (2023). The Marker Band in Gale crater: A synthesis of orbital and ground. *54th Lunar and Planetary Science Conference*, 2806.

Wellington, D. F., Johnson, J. R., Meslin, P. Y., & Bell, J. F., III. (2018). Iron meteorite candidates within Gale crater, Mars, from MSL/Mastcam multispectral observations. *49th Lunar and Planetary Science Conference.*

Wiens, R. C., Maurice, S., Barraclough, B., Saccoccio, M., Barkley, W. C., Bell, J. F., et al. (2012). The ChemCam Instrument Suite on the Mars Science Laboratory (MSL) Rover: Body Unit and Combined System Tests. *Space Science Reviews*, *170*(1), 167–227. https://doi.org/10.1007/s11214-012-9902-4

Wray, J. (2013). Gale Crater: The Mars Science Laboratory/Curiosity Rover Landing Site. *International Journal of Astrobiology*, *12*, 25–38. https://doi.org/10.1017/S1473550412000328

Xu, W., & Parise, J. B. (2012). Temperature and humidity effects on ferric sulfate stability and phase transformation. *American Mineralogist*, *97*(2–3), 378–383. https://doi.org/10.2138/am.2012.3927

Yu, X., Zhao, Y., Wu, Y., Qi, C., Li, D., Honglei, L., Yang, S., Liu, J., & Li, X. (2022). Cryogenic Sulfuric Weathering and Challenges for Preserving Iron-Rich Olivine on Cold and Icy Mars. *Journal of Geophysical Research: Planets*, *128*. https://doi.org/10.1029/2022JE007593

Zolotov, M. Y., & Mironenko, M. V. (2007). Timing of acid weathering on Mars: A kinetic-thermodynamic assessment. *Journal of Geophysical Research: Planets*, *112*(E7). https://doi.org/10.1029/2006JE002882

Table S1: Mastcam multispectral observations used in this study collected post sol 2302

Group	Formation	Member	Sol	SeqID	Name
Mt. Sharp	Murray	Jura	2304	mcam12306	St_Fergus
Mt. Sharp	Murray	Jura	2313	mcam12349	Alba Dun Ara
Mt. Sharp	Murray	Jura	2316	mcam12363	Dauntless_to_Emerald
Mt. Sharp	Murray	Jura	2319	mcam12388	Clyde_Gannet
Mt. Sharp	Murray	Jura	2319	mcam12390	Curlew
Mt. Sharp	Murray	Jura	2320	mcam12405	Curlew (redo)
Mt. Sharp	Murray	Jura	2338	mcam12420	Cuttyhill
Mt. Sharp	Murray	Jura	2338	mcam12421	Leslie
Mt. Sharp	Murray	Jura	2347	mcam12448	Arbuthnott Fife
Mt. Sharp	Murray	Jura	2349	mcam12464	Caledonia
Mt. Sharp	Murray	Jura	2351	mcam12472	Muir of Ord
Mt. Sharp	Murray	Jura	2361	mcam12513	Eorsa
Mt. Sharp	Murray	Jura	2368	mcam12563	Aberlady DRT
Mt. Sharp	Murray	Jura	2371	mcam12572	Aberlady Stereo
Mt. Sharp	Murray	Jura	2371	mcam12574	Light Toned VRR Stereo
Mt. Sharp	Murray	Jura	2374	mcam12585	Lumphanan
Mt. Sharp	Murray	Jura	2380	mcam12649	Aberlady Dump Pile
Mt. Sharp	Murray	Jura	2385	mcam12661	Kilmarie
Mt. Sharp	Murray	Jura	2385	mcam12662	Aberlady Drill Tailings
Mt. Sharp	Murray	Jura	2407	mcam12758	Kilmaire Dump Pile Redo
Mt. Sharp	Murray	Jura	2409	mcam12773	Rigg Scuff 2x1
Mt. Sharp	Murray	Jura	2414	mcam12797	Annbank_Brimmond 2x1
Mt. Sharp	Murray	Jura	2414	mcam12798	West_Linga
Mt. Sharp	Murray	Jura	2416	mcam12812	Broad_Cairn Stereo
Mt. Sharp	Murray	Jura	2425	mcam12843	West_Side Stereo
Mt. Sharp	Murray	Jura	2425	mcam12845	Morningside Stereo
Mt. Sharp	Murray	Jura	2429	mcam12855	Morningside Stereo (redo)

Mt. Sharp	Murray	Jura	2429	mcam12856	West_Side Stereo (redo)
Mt. Sharp	Murray	Jura	2435	mcam12909	little_minch_strathspey
Mt. Sharp	Murray	Jura	2437	mcam12920	Tweed
Mt. Sharp	Murray	Knockfarril Hill	2447	mcam12970	Beauly
Mt. Sharp	Murray	Knockfarril Hill	2453	mcam13017	Buckie
Mt. Sharp	Murray	Knockfarril Hill	2454	mcam13024	Perth
Mt. Sharp	Murray	Knockfarril Hill	2459	mcam13052	Oykel DRT
Mt. Sharp	Murray	Knockfarril Hill	2464	mcam13075	Visionarium stereo_Lall_2x1_Rall
Mt. Sharp	Murray	Knockfarril Hill	2472	mcam13113	Joppa Shore
Mt. Sharp	Murray	Knockfarril Hill	2472	mcam13114	Sandside Harbour
Mt. Sharp	Murray	Knockfarril Hill	2484	mcam13201	Glen Etive stereo 2x1
Mt. Sharp	Murray	Knockfarril Hill	2487	mcam13211	Glen Etive 1 Drill Tailings
Mt. Sharp	Murray	Knockfarril Hill	2494	mcam13249	Monach Isles
Mt. Sharp	Murray	Knockfarril Hill	2504	mcam13290	Windy Swire Stereo
Mt. Sharp	Murray	Knockfarril Hill	2504	mcam13291	Stone Row
Mt. Sharp	Murray	Knockfarril Hill	2526	mcam13323	Glen Etive 1 Dump Pile
Mt. Sharp	Murray	Knockfarril Hill	2528	mcam13330	Glen Etive 2 Drill Tailings
Mt. Sharp	Murray	Knockfarril Hill	2532	mcam13348	Brawl Stereo
Mt. Sharp	Murray	Knockfarril Hill	2554	mcam13419	Glen Etive 2 Dump Pile
Mt. Sharp	Murray	Knockfarril Hill	2570	mcam13490	Solan Bank

Mt. Sharp	Murray	Knockfarril Hill	2582	mcam13566	Conachair DRT stereo
Mt. Sharp	Murray	Knockfarril Hill	2584	mcam13578	Central Butte Top
Mt. Sharp	Murray	Knockfarril Hill	2592	mcam13626	Muckle Flugga
Mt. Sharp	Murray	Greenheugh Pediment	2611	mcam13722	Glen Trool Stereo
Mt. Sharp	Murray	Glasgow	2613	mcam13733	Glen Nevis
Mt. Sharp	Murray	Glasgow	2620	mcam13763	Blackwaterfoot Stereo
Mt. Sharp	Murray	Glasgow	2632	mcam13786	Ben Arnaboll DRT Stereo
Mt. Sharp	Murray	Glasgow	2636	mcam13804	Lauderdale Stereo
Mt. Sharp	Murray	Glasgow	2639	mcam13815	Ben Eighe
Mt. Sharp	Murray	Glasgow	2641	mcam13828	Buchan_Haven Stereo
	Murray/Unknown	Unknown	2641	mcam13830	Crianlarich Hills
Mt. Sharp	Murray	Glasgow	2643	mcam13838	Hascosay Stereo
Mt. Sharp	Murray	Glasgow	2654	mcam13874	Trossachs DRT
Mt. Sharp	Murray	Glasgow	2657	mcam13904	Sauchiehall DRT Stereo
Mt. Sharp	Murray	Glasgow	2661	mcam13938	Hastigrow Tillicoultry 2x1
Mt. Sharp	Murray	Glasgow	2661	mcam13940	Cullivoe Stereo
Mt. Sharp	Murray	Glasgow	2663	mcam13956	Berwickshire Stereo
Mt. Sharp	Murray	Glasgow	2666	mcam13983	Hutton DRT
Siccar Point	Stimson	Greenheugh Pediment	2695	mcam14094	Huttons Section
Siccar Point	Stimson	Greenheugh Pediment	2698	mcam14119	Galloway Hills Stereo
Siccar Point	Stimson	Greenheugh Pediment	2702	mcam14152	Assynt Window Stereo
Siccar Point	Stimson	Greenheugh Pediment	2705	mcam14177	Edinburgh Stereo
Siccar Point	Stimson	Greenheugh Pediment	2710	mcam14191	Eshaness Stereo

Siccar Point	Stimson	Greenheugh Pediment	2712	mcam14203	Edinburgh Stereo
Siccar Point	Stimson	Greenheugh Pediment	2726	mcam14264	Edinburgh Dump Pile
Mt. Sharp	Carolyn Shoemaker	Glasgow	2737	mcam14344	Creig DRT Stereo
Mt. Sharp	Carolyn Shoemaker	Glasgow	2745	mcam14393	Beefstand_Hill Stereo
Mt. Sharp	Carolyn Shoemaker	Glasgow	2750	mcam14418	Glasgow 1 DRT
Mt. Sharp	Carolyn Shoemaker	Glasgow	2753	mcam14429	Glasgow 1 DRT
Mt. Sharp	Carolyn Shoemaker	Glasgow	2755	mcam14442	Glasgow 1 DRT (Tailings)
Mt. Sharp	Carolyn Shoemaker	Glasgow	2777	mcam14542	glasgow_dump_pile
Mt. Sharp	Carolyn Shoemaker	Glasgow	2786	mcam14591	Heather Island Stereo
Mt. Sharp	Carolyn Shoemaker	Glasgow	2793	mcam14634	Hedgeley Moor Stereo
Mt. Sharp	Carolyn Shoemaker	Glasgow	2799	mcam14665	BlackHillock Stereo
Mt. Sharp	Carolyn Shoemaker	Glasgow	2802	mcam 14693	Chambers Street Stereo
Mt. Sharp	Carolyn Shoemaker	Knockfarrill Hill	2829	mcam14808	Breamish Stereo
Mt. Sharp	Carolyn Shoemaker	Knockfarrill Hill	2836	mcam14832	Mary Anning Stereo
Mt. Sharp	Carolyn Shoemaker	Knockfarrill Hill	2837	mcam14837	Mary Anning Stereo
Mt. Sharp	Carolyn Shoemaker	Knockfarrill Hill	2840	mcam14857	Mary Anning Stereo
Mt. Sharp	Carolyn Shoemaker	Knockfarrill Hill	2852	mcam14904	Mary Anning Dump Stereo
Mt. Sharp	Carolyn Shoemaker	Knockfarrill Hill	2862	mcam14944	Mary Anning 2 Stereo
Mt. Sharp	Carolyn Shoemaker	Knockfarrill Hill	2869	mcam14968	Mary Anning 3 Stereo
Mt. Sharp	Carolyn Shoemaker	Knockfarrill Hill	2871	mcam14977	Mary Anning 3 Stereo

Mt. Sharp	Carolyn Shoemaker	Knockfarrill Hill	2882	mcam15033	Le Ceasnachadh Stereo
Mt. Sharp	Carolyn Shoemaker	Knockfarrill Hill	2891	mcam15083	Mary Anning 3 dump
Mt. Sharp	Carolyn Shoemaker	Knockfarrill Hill	2898	mcam15118	Duachy Duntulm Stereo
Mt. Sharp	Carolyn Shoemaker	Knockfarrill Hill	2907	mcam15164	Groken DRT stereo
Mt. Sharp	Carolyn Shoemaker	Knockfarrill Hill	2909	mcam15182	Trow Stereo
Mt. Sharp	Carolyn Shoemaker	Knockfarrill Hill	2911	mcam15193	Groken Tailings
Mt. Sharp	Carolyn Shoemaker	Glasgow	2929	mcam15279	VRR Light Toned Stereo
Mt. Sharp	Carolyn Shoemaker	Glasgow	2936	mcam15318	Hunt Hill Stereo
Mt. Sharp	Carolyn Shoemaker	Glasgow	2940	mcam15338	Stow Stereo
Mt. Sharp	Carolyn Shoemaker	Glasgow	2943	mcam15349	Geesa Water Stereo
Mt. Sharp	Carolyn Shoemaker	Glasgow	2946	mcam15372	Lasswade Stereo
Mt. Sharp	Carolyn Shoemaker	Glasgow	2950	mcam15397	DRT Giova Stereo
Mt. Sharp	Carolyn Shoemaker	Glasgow	2956	mcam15430	Rest and be Thankful
Mt. Sharp	Carolyn Shoemaker	Glasgow	2961	mcam15459	Island Davaar Stereo
Mt. Sharp	Carolyn Shoemaker	Glasgow	2963	mcam15469	Ben Hee Stereo
Mt. Sharp	Carolyn Shoemaker	Glasgow	2965	mcam15478	Saasaig Stereo
Mt. Sharp	Carolyn Shoemaker	Glasgow	2965	mcam15480	Island Davaar Stereo
Mt. Sharp	Carolyn Shoemaker	Glasgow	2967	mcam15488	Island Davaar Stereo
Mt. Sharp	Carolyn Shoemaker	Glasgow	2967	mcam15490	Obar Dheathain Stereo
Mt. Sharp	Carolyn Shoemaker	Glasgow	2975	mcam15538	Cod Baa Stereo

Mt. Sharp	Carolyn Shoemaker	Glasgow	2975	mcam15541	Rubbly unit 5x2
Mt. Sharp	Carolyn Shoemaker	Glasgow	2992	mcam15599	Columbas Bay
Mt. Sharp	Carolyn Shoemaker	Glasgow	2997	mcam15628	St. Andrew Square
Mt. Sharp	Carolyn Shoemaker	Glasgow	2999	mcam15640	St. Andrew Square
Mt. Sharp	Carolyn Shoemaker	Glasgow	3007	mcam15673	Easthouses Stereo
Mt. Sharp	Carolyn Shoemaker	Glasgow	3011	mcam15700	La Roque Gageac
Mt. Sharp	Carolyn Shoemaker	Glasgow	3013	mcam15711	Marnac
Mt. Sharp	Carolyn Shoemaker	Glasgow	3015	mcam15720	Beaupouyet Stereo
Mt. Sharp	Carolyn Shoemaker	Glasgow	3017	mcam15725	Vezere Stereo
Mt. Sharp	Carolyn Shoemaker	Glasgow	3018	mcam15738	Neuvic Stereo
Mt. Sharp	Carolyn Shoemaker	Glasgow	3022	mcam15755	Tamnies Stereo
Mt. Sharp	Carolyn Shoemaker	Glasgow	3025	mcam15773	Coutures
Mt. Sharp	Carolyn Shoemaker	Glasgow	3025	mcam15775	Basal Sulfate Unit 2x1
Mt. Sharp	Carolyn Shoemaker	Glasgow	3026	mcam15785	Azerat
Mt. Sharp	Carolyn Shoemaker	Glasgow	3027	mcam15792	Brantome
Mt. Sharp	Carolyn Shoemaker	Glasgow	3027	mcam15794	Bourdeilles
Mt. Sharp	Carolyn Shoemaker	Glasgow	3028	mcam15805	Firbeix
Mt. Sharp	Carolyn Shoemaker	Glasgow	3032	mcam15822	Dordogne
Mt. Sharp	Carolyn Shoemaker	Glasgow	3034	mcam15833	Fleurac
Mt. Sharp	Carolyn Shoemaker	Glasgow	3035	mcam15844	Limeyrat

Mt. Sharp	Carolyn Shoemaker	Glasgow	3038	mcam15866	Chalus
Mt. Sharp	Carolyn Shoemaker	Glasgow	3045	mcam15897	Saussignac
Mt. Sharp	Carolyn Shoemaker	Glasgow	3045	mcam15899	Sadillac Pazayac
Mt. Sharp	Carolyn Shoemaker	Glasgow	3047	mcam15907	Cornille
Mt. Sharp	Carolyn Shoemaker	Glasgow	3049	mcam15921	Marval
Mt. Sharp	Carolyn Shoemaker	Mercou	3052	mcam15941	Montrem
Mt. Sharp	Carolyn Shoemaker	Mercou	3055	mcam15959	La Coquille
Mt. Sharp	Carolyn Shoemaker	Mercou	3055	mcam15961	Nontron Drill Hole
Mt. Sharp	Carolyn Shoemaker	Mercou	3057	mcam15968	Rocamadour
Mt. Sharp	Carolyn Shoemaker	Mercou	3057	mcam15970	Nontron Tailings
Mt. Sharp	Carolyn Shoemaker	Mercou	3059	mcam15977	Mont Mercou
Mt. Sharp	Carolyn Shoemaker	Mercou	3072	mcam16042	Nontron Dump Pile
Mt. Sharp	Carolyn Shoemaker	Mercou	3076	mcam16064	Maurens Stereo
Mt. Sharp	Carolyn Shoemaker	Mercou	3086	mcam16123	Peyrignac Stereo
Mt. Sharp	Carolyn Shoemaker	Mercou	3086	mcam16125	Cubjac Stereo
Mt. Sharp	Carolyn Shoemaker	Mercou	3091	mcam16149	Bardou Stereo
Mt. Sharp	Carolyn Shoemaker	Mercou	3095	mcam16163	Bardou Tailings Stereo
Mt. Sharp	Carolyn Shoemaker	Mercou	3101	mcam16187	Tour Blanche Stereo
Mt. Sharp	Carolyn Shoemaker	Mercou	3106	mcam16243	Bardou dump
Mt. Sharp	Carolyn Shoemaker	Mercou	3110	mcam00027	Pech Du Loup Stereo

Mt. Sharp	Carolyn Shoemaker	Mercou	3113	mcam00040	Gourdon Stereo
Mt. Sharp	Carolyn Shoemaker	Mercou	3113	mcam00042	Mayac Stereo
Mt. Sharp	Carolyn Shoemaker	Mercou	3115	mcam00049	Coly Stereo
Mt. Sharp	Carolyn Shoemaker	Mercou	3120	mcam00074	Monsec stereo
Mt. Sharp	Carolyn Shoemaker		3140	mcam00185	Petit Bersac
Mt. Sharp	Carolyn Shoemaker		3143	mcam00195	Vayres Stereo
Mt. Sharp	Carolyn Shoemaker		3143	mcam00197	Videix Stereo
Mt. Sharp	Carolyn Shoemaker		3145	mcam00216	Plaisance Stereo
Mt. Sharp	Carolyn Shoemaker	Pontours	3158	mcam00311	Bosset
Mt. Sharp	Carolyn Shoemaker	Pontours	3161	mcam00326	Simeyrols
Mt. Sharp	Carolyn Shoemaker	Pontours	3163	mcam00341	Gardonne
Mt. Sharp	Carolyn Shoemaker	Pontours	3165	mcam00362	Colombier Stereo
Mt. Sharp	Carolyn Shoemaker	Pontours	3169	mcam00379	Pontours Stereo
Mt. Sharp	Carolyn Shoemaker	Pontours	3171	mcam00392	Pontours Tailings
Mt. Sharp	Carolyn Shoemaker	Pontours	3178	mcam00422	Bussac Stereo
Mt. Sharp	Carolyn Shoemaker	Pontours	3180	mcam00443	Pontours Dump
Mt. Sharp	Carolyn Shoemaker	Pontours	3180	mcam00445	Bouzic Stereo
Mt. Sharp	Carolyn Shoemaker	Pontours	3185	mcam00475	Prats de Carlux Stereo
Mt. Sharp	Carolyn Shoemaker	Pontours	3185	mcam00477	Rampieux Stereo
Mt. Sharp	Carolyn Shoemaker	Pontours	3188	mcam00495	Chauffour Stereo

Mt. Sharp	Mirador	Dunnideer	3194	mcam00521	Blue Stones Stereo
Mt. Sharp	Mirador	Dunnideer	3197	mcam00539	Vendoire Beleymas
Mt. Sharp	Mirador	Dunnideer	3197	mcam00540	Baneuil
Mt. Sharp	Mirador	Dunnideer	3202	mcam00568	Nadaillac rp drt Stereo
Mt. Sharp	Mirador	Dunnideer	3203	mcam00586	Blis Et Born Stereo
Mt. Sharp	Mirador	Dunnideer	3209	mcam00619	Kilmaluag Stereo
Mt. Sharp	Mirador	Dunnideer	3210	mcam00638	Solway Lowlands Stereo
Mt. Sharp	Mirador	Dunnideer	3215	mcam00671	Newcraighall Stereo
Mt. Sharp	Mirador	Dunnideer	3222	mcam00703	Saltopus Stereo
Mt. Sharp	Mirador	Dunnideer	3222	mcam00705	Temptation Hill Stereo
Mt. Sharp	Mirador	Dunnideer	3228	mcam00733	Maria Gordon DRT Stereo
Mt. Sharp	Mirador	Dunnideer	3230	mcam00745	Maria Gordon Tailings Stereo
Mt. Sharp	Mirador	Dunnideer	3247	mcam00822	Maria Gordon Dump pile
Mt. Sharp	Mirador	Dunnideer	3248	mcam00828	Helmsdale Boulder
Mt. Sharp	Mirador	Dunnideer	3274	mcam00860	Acadian Stereo
Mt. Sharp	Mirador	Port Logan	3279	mcam00897	Denburn Stereo
Mt. Sharp	Mirador	Port Logan	3284	mcam00932	Isle of Mists
Mt. Sharp	Mirador	Port Logan	3288	mcam00962	Zechstein DRT
Mt. Sharp	Mirador	Port Logan	3290	mcam00975	Zechstein Tailings
Mt. Sharp	Mirador	Port Logan	3302	mcam01034	Zechstein Dump pile
Mt. Sharp	Mirador	Port Logan	3303	mcam01036	Maria Gordon Notch 6x1
Mt. Sharp	Mirador	Port Logan	3316	mcam01097	Arainn Stereo
Mt. Sharp	Mirador	Port Logan	3316	mcam01099	Yarrow Stone
Mt. Sharp	Mirador	Port Logan	3322	mcam01136	Cladh Hallan Stereo

Mt. Sharp	Mirador	Port Logan	3329	mcam01166	Maria Gordon West
Mt. Sharp	Mirador	Port Logan	3331	mcam01192	DRT clochoderick
Mt. Sharp	Mirador	Port Logan	3345	mcam01226	Maes Howe ccam
Mt. Sharp	Mirador	Port Logan	3351	mcam01256	Indio Stereo
Mt. Sharp	Mirador	Port Logan	3359	mcam01324	Chimata Stereo
Mt. Sharp	Mirador	Port Logan	3369	mcam01367	Kambaouk stereo
Mt. Sharp	Mirador	Port Logan	3372	mcam01395	Suapi DRT
Mt. Sharp	Mirador	Port Logan	3379	mcam01421	Cucurital stereo
Mt. Sharp	Mirador	Port Logan	3386	mcam01462	Kintradwell DRT Stereo
Mt. Sharp	Mirador	Port Logan	3390	mcam01500	Loch Coruisk stereo
Mt. Sharp/Siccar Point Transition	Mt. Sharp/Siccar Point Transition	Mt. Sharp/Siccar Point Transition	3391	mcam01509	Tomnaverie Stereo
Mt. Sharp/Siccar Point Transition	Mt. Sharp/Siccar Point Transition	Mt. Sharp/Siccar Point Transition	3396	mcam01535	Galdenoch DRT
Mt. Sharp/Siccar Point Transition	Mt. Sharp/Siccar Point Transition	Mt. Sharp/Siccar Point Transition	3397	mcam01546	Scousburgh DRT
Siccar Point	Stimson	Greenheugh Pediment	3406	mcam01599	East Suisnish stereo
Siccar Point	Stimson	Greenheugh Pediment	3413	mcam01631	Skaw Ridge DRT
Siccar Point	Stimson	Greenheugh Pediment	3423	mcam01696	Calder DRT
Siccar Point	Stimson	Greenheugh Pediment	3435	mcam01783	Donkey Train Venlaw 2x1
Siccar Point	Stimson	Greenheugh Pediment	3440	mcam01825	Denny
Siccar Point	Stimson	Greenheugh Pediment	3443	mcam01845	Brackenberry DRT
Mt. Sharp	Mirador	Port Logan	3452	mcam01889	Shandon DRT
Mt. Sharp	Mirador	Port Logan	3454	mcam01904	Delting DRT stereo

Mt. Sharp	Mirador	Port Logan	3454	mcam01906	Rumblings
Mt. Sharp	Mirador		3458	mcam01924	Maringma Butte
Mt. Sharp	Mirador	Contigo	3472	mcam01999	Pastora DRT
Mt. Sharp	Mirador	Contigo	3474	mcam02018	San Pedro DRT
Mt. Sharp	Mirador	Contigo	3480	mcam02065	Sunset Sky stereo
Mt. Sharp	Mirador	Contigo	3481	mcam02069	Bamboo Creek DRT
Mt. Sharp	Mirador	Contigo	3485	mcam02102	Cabo Sobral
Mt. Sharp	Mirador	Contigo	3489	mcam02122	Pitinga DRT
Mt. Sharp	Mirador	Contigo	3492	mcam02144	Parepona
Mt. Sharp	Mirador	Contigo	3495	mcam02166	Issano
Mt. Sharp	Mirador	Contigo	3504	mcam02196	Omai Stereo
Mt. Sharp	Mirador	Contigo	3506	mcam02207	Mahdia 2 stereo
Mt. Sharp	Mirador	Contigo	3508	mcam02218	Kukui Stereo
Mt. Sharp	Mirador	Contigo	3512	mcam02243	Avanavero Stereo
Mt. Sharp	Mirador	Contigo	3512	mcam02245	Marbura Hill Stereo
Mt. Sharp	Mirador	Contigo	3513	mcam02254	Avanavero Tailings
Mt. Sharp	Mirador	Contigo	3514	mcam02266	Kamana Stereo
Mt. Sharp	Mirador	Contigo	3527	mcam02311	Bolivar Stereo
Mt. Sharp	Mirador	Contigo	3527	mcam02316	Isla Caou Stereo
Mt. Sharp	Mirador	Contigo	3533	mcam02371	Seringa Stereo
Mt. Sharp	Mirador	Contigo	3536	mcam02384	Ilha Novo Destino
Mt. Sharp	Mirador	Contigo	3542	mcam02420	Merume Stereo
Mt. Sharp	Mirador	Contigo	3543	mcam02425	Motocuruna DRT Stereo
Mt. Sharp	Mirador	Contigo	3544	mcam02433	Lagoa do Paraiso
Mt. Sharp	Mirador	Contigo	3546	mcam02452	Deepdale Stereo
Mt. Sharp	Mirador	Contigo	3546	mcam02458	Lilas Stereo
Mt. Sharp	Mirador	Contigo	3549	mcam02475	Salto Sakaika Stereo
Mt. Sharp	Mirador	Contigo	3553	mcam02494	Arorouta Stereo
Mt. Sharp	Mirador	Contigo	3555	mcam02509	Linden Stereo
Mt. Sharp	Mirador	Contigo	3558	mcam02528	El Caura Stereo
Mt. Sharp	Mirador	Contigo	3560	mcam02543	Annai Stereo
Mt. Sharp	Mirador	Contigo	3565	mcam02574	Karia Island

Mt. Sharp	Mirador	Contigo	3569	mcam02609	Massara Stereo
Mt. Sharp	Mirador	Contigo	3569	mcam02611	Stampa Island Stereo
Mt. Sharp	Mirador	Contigo	3574	mcam02648	Liberdade Stereo
Mt. Sharp	Mirador	Contigo	3579	mcam02679	Micobie Sterio
Mt. Sharp	Mirador	Contigo	3580	mcam02686	Las Lajitas Stereo
Mt. Sharp	Mirador	Contigo	3589	mcam02725	La Soledad
Mt. Sharp	Mirador	Contigo	3592	mcam02736	Vendaval Stereo
Mt. Sharp	Mirador	Contigo	3597	mcam02767	Marshall Falls Stereo
Mt. Sharp	Mirador	Contigo	3597	mcam02769	Corona Falls Stereo
Mt. Sharp	Mirador	Contigo	3601	mcam02791	Cauarane Stereo
Mt. Sharp	Mirador	Contigo	3603	mcam02802	Waioklepalul Stereo
Mt. Sharp	Mirador	Contigo	3606	mcam02817	Jerry Springer Stereo
Mt. Sharp	Mirador	Contigo	3610	mcam02839	Canaima Drt Stereo
Mt. Sharp	Mirador	Contigo	3613	mcam02849	Canaima Tailings Stereo
Mt. Sharp	Mirador	Contigo	3608	mcam02827	Kabrito Island
Mt. Sharp	Mirador	Contigo	3623	mcam02913	Dress Island Stereo
Mt. Sharp	Mirador	Catrimani	3631	mcam02949	Calcara Stereo
Mt. Sharp	Mirador	Catrimani	3635	mcam02966	Maraca Stereo
Mt. Sharp	Mirador	Catrimani	3638	mcam02985	Catrimani Drt Stereo
Mt. Sharp	Mirador	Amapari Marker Band	3640	mcam03001	Patua Stereo
Mt. Sharp	Mirador	Amapari Marker Band	3640	mcam03003	Tucano Stereo
Mt. Sharp	Mirador	Amapari Marker Band	3642	mcam03022	Mel Stereo
Mt. Sharp	Mirador	Amapari Marker Band	3642	mcam03024	Mamupi Stereo

Mt. Sharp	Mirador	Amapari Marker Band	3643	mcam03029	Saracura Stereo
Mt. Sharp	Mirador	Amapari Marker Band	3648	mcam03055	Cana Stereo
Mt. Sharp	Mirador	Amapari Marker Band	3651	mcam03081	Raposa Stereo (DRT)
Mt. Sharp	Mirador	Amapari Marker Band	3655	mcam03106	Saddle Mountain Stereo
Mt. Sharp	Mirador	Amapari Marker Band	3658	mcam03129	Xua Stereo
Mt. Sharp	Mirador	Amapari Marker Band	3658	mcam03130	Lua Stereo
Mt. Sharp	Mirador	Amapari Marker Band	3658	mcam03132	Rio Jufari Stereo
Mt. Sharp	Mirador	Amapari Marker Band	3665	mcam03167	Poraque Stereo
Mt. Sharp	Mirador	Amapari Marker Band	3665	mcam03169	Los Tranques Stereo
Mt. Sharp	Mirador	Amapari Marker Band	3667	mcam03185	Flecha Stereo
Mt. Sharp	Mirador	Amapari Marker Band	3669	mcam03199	Niquia Stereo
Mt. Sharp	Mirador	Amapari Marker Band	3669	mcam03200	Jufari Stereo
Mt. Sharp	Mirador	Amapari Marker Band	3669	mcam03202	Roxinho Stereo
Mt. Sharp	Mirador	Amapari Marker Band	3672	mcam03216	Shabono Stereo

Table S2: Components of laboratory mixtures with calculated parameters that can be associated with hydration.

Wt. % epsomite	Phyllosilicate	Wt. % phyllosilicate	Wt. % basalt	1013 nm/ 937 nm ratio	937 nm/ 805 nm ratio
90	Montmorillonite	10	0	0.988821	1.002376
85.5	Montmorillonite	9.5	5	1.004563	1.009218
81	Montmorillonite	9	10	0.996658	0.991387
85	Montmorillonite	15	0	0.999612	1.01405
80.75	Montmorillonite	14.25	5	1.000515	1.001587
76.5	Montmorillonite	13.5	10	0.997708	0.99293
80	Montmorillonite	20	0	1.003000	1.018093
76	Montmorillonite	19	5	1.005248	1.010118
72	Montmorillonite	18	10	0.993904	0.985029
95	Saponite	5	0	0.992769	1.007369
90.25	Saponite	4.75	5	0.998788	0.996536
85.5	Saponite	4.5	10	1.001868	1.003074
90	Saponite	10	0	1.001481	1.01623
85.5	Saponite	9.5	5	1.003119	1.007325
81	Saponite	9	10	1.002816	1.000654
80	Saponite	20	0	1.006186	1.016817
76	Saponite	19	5	1.002623	1.00337
72	Saponite	18	10	0.998693	0.991243
95	Nontronite	5	0	1.004994	0.997725
90.25	Nontronite	4.75	5	1.006684	1.00333
85.5	Nontronite	4.5	10	0.999772	0.985562
90	Nontronite	10	0	1.01086	0.987369
85.5	Nontronite	9.5	5	1.007922	0.987672
81	Nontronite	9	10	1.005081	0.98545
80	Nontronite	20	0	1.020631	0.97976
76	Nontronite	19	5	1.014521	0.98068
72	Nontronite	18	10	1.008291	0.972034

Table S3: Equations for ChemCam and Mastcam parameters

Instrument	Parameter	Equation
ChemCam	535 nm band	$1\text{-}R^*_{535}/(0.65\ R^*_{500} + 0.35\ R^*_{600})$
Mastcam	527 nm band	$1—R^*_{527}/(0.645R^*_{445} + 0.355R^*_{676})$
ChemCam	751-805 nm slope	$(R^*_{751} - R^*_{805})/(751\text{-}805)$
Mastcam	751-805 nm slope	$(R^*_{751} - R^*_{805})/(751\text{-}805)$

Table S4: ChemCam and Mastcam sequences used to calculate parameters in Table S3

Class	Mastcam	ChemCam
J	Sol 3669 mcam03202	Sol 3668 ccam03667
K	Sol 3331 mcam01192	Sol 3331 ccam03330
L	Sol 3643 mcam03029	Sol 3640 ccam01640
M	Sol 3423 mcam01696	Sol 3423 mcam01423

Table S5: ChemCam and Mastcam values for parameters in Table S3 using sequences in Table S4

Instrument	Parameter	Result
Red VIS slope with small 1013 nm/937 nm ratio		
ChemCam	535 nm band	0.040
Mastcam	527 nm band	0.150
ChemCam	751-805 nm slope	4.67E-05
Mastcam	751-805 nm slope	2.87E-04
Long, negative NIR slope		
ChemCam	535 nm band	0.115
Mastcam	527 nm band	0.226
ChemCam	751-805 nm slope	-3.00E-04
Mastcam	751-805 nm slope	-2.10E-04
Convex Profile w/ small 1012/867 nm		
ChemCam	535 nm band	0.096
Mastcam	527 nm band	0.025
ChemCam	751-805 nm slope	-2.28E-05
Mastcam	751-805 nm slope	-7.55E-06
Flat profile w/ small 1013/937 nm ratio		
ChemCam	535 nm band	0.071

Mastcam	527 nm band	0.058
ChemCam	751-805 nm slope	-7.30E-05
Mastcam	751-805 nm slope	3.19E-05